Upconversion Dynamics and Energy Transfer:

Er3+: YAlO3, YAG and Tm3+: YLF, YBF

by

Jianan Wang

A Thesis Submitted to the Faculty of
Graduate Studies and Research
in Partial Fulfilment of the Requirements for the
Degree of Doctor of Philosophy

McGill University

Department of Physics

Montreal, Quebec, Canada

© February 1996



Acquisitions and Bibliographic Services Branch

మక Wellington Street Ottawa, Onlario K1A 0N4 Bibliothèque nationale du Canada

Direction des acquisitions et des services bibliographiques

395, rue Wellington Ottawa (Cntario) K1A 0N4

Your life. Votre référence

Our lile Notre référence

The author has granted an irrevocable non-exclusive licence allowing the National Library of Canada to reproduce, loan, distribute or sell copies of his/her thesis by any means and in any form or format, making this thesis available to interested persons.

L'auteur a accordé une licence irrévocable et non exclusive permettant à la Bibliothèque nationale ďи Canada reproduire, prêter, distribuer ou vendre des copies de sa thèse de quelque manière et sous quelque forme que ce soit pour mettre des exemplaires de cette thèse disposition la des personnes intéressées.

The author retains ownership of the copyright in his/her thesis. Neither the thesis nor substantial extracts from it may be printed or otherwise reproduced without his/her permission. L'auteur conserve la propriété du droit d'auteur qui protège sa thèse. Ni la thèse ni des extraits substantiels de celle-ci ne doivent être imprimés ou autrement reproduits sans son autorisation.

ISBN 0-612-19784-0



Dedicated to my parents

ABSTRACT

This thesis describes detailed studies of the upconversion dynamics of $Er^{3+}:YAlO_3$ (YAP), $Er^{3+}:YAG$, $Tm^{3+}:Y_2BaF_8$ (YAB) and the avalanche upconversion dynamics of $Tm^{3+}:YLiF_4$ (YLF).

Upconversion dynamics of Er³⁺:YAP, and Er³⁺:YAG are analyzed by a rate equation model which includes four energy transfer processes. It was found that good fits to the experimental data can be achieved only when the fourth power activator concentration dependent energy transfer terms (when the energy transfer is fourth order kinetically) are included in the rate equation.

To study avalanche upconversion dynamics of Tm3:YLF measurements of the time dependent upconversion luminescence intensity were made under different pumping wavelengths and different pumping powers at both low temperature and room The pumping power dependent upconversion luminescence was also measured. To describe the avalanche upconversion dynamics a rate equation model which includes both the cross-relaxation and energy transfer processes was developed. Satisfactory fits simulations of the or experimental data were obtained in every case. Through this work it was found that the energy transfer term is proportional to the second power of the activator concentration (second order kinetically) at low activator concentration and proportional to the fourth power of the activator concentration (fourth order kinetically) at high activator concentration.

To obtain the fourth power activator concentration dependent energy transfer term, the existing three-body interaction model obtained from the second order perturbation theory was extended to the case of four-body interaction, and a two-body interaction dipole-dipole energy transfer model based on regular distribution of the donors and acceptors and two dimensional transfer was built.

Upconversion dynamics of Tm³⁺:YBF is analyzed by a rate equation model which includes two energy transfer processes. Satisfactory fits of the experimental data were obtained by this model. Pump-probe measurements of the temperature and power dependence of the upconversion gain for the blue emission at 482 nm from Tm³⁺:YBF are presented.

RÉSUMÉ

Cette thèse porte sur l'étude en détail de la dynamique de conversion du $Er^{3+}:YAlO_3$ (YAP), $Er^{3+}:YAG$, $Tm^{3+}:Y_2BaF_8$ (YAB) et de conversion avalanche du $Tm^{3+}:YLiF_4$ (YLF).

La dynamique de conversion du Er3-:YAP et du Er3-:YAG, est analysée par un modèle de loi de vitesse comprenant quatres processus de transfert énergétiques. Il a été démontré qu'une bonne concordance avec les donnés expérimentales ne peut être obtenue que lorsque la puissance quatre du terme de concentration de l'activateur de la loi de vitesse de transfert énergétique (transfert énergétique d'ordre quatre cinétiquement parlant) se trouve inclus dans la loi de vitesse.

Pour étudier la dynamique de la conversion avalanche du Tm3: YLF, des mesures de la dépendance en temps de l'intensité de la luminescence ont été éffectués avec plusieurs longueurs d'onde d'excitation, ainsi plusieurs puissances que d'exitation. La dépendance de la luminescence sur la puissance d'excitation a aussi été évaluée. Pour représenter la dynamique de la conversion avalanche, un modèle de loi de vitesse tenant compte de la relaxation non-radiative extrachromophorique ainsi que des processus de transfert énergétiques a été mis au point. concordance Une satisfaisante ou une modélisation des donnés expérimentales a été obtenue dans chaque cas. Par le bias de cette étude, il

a été démontré que la vitesse du transfert énergétique est proportionnelle à la puissance deux de la concentration de l'activateur (ordre deux cinetiquement parlant) pour les faibles concentrations de l'activateur tandis que cette même proprotionnalité est d'ordre quatre pour des concentrations d'activateur élevées.

Pour obtenir la loi de vitesse de transfert énergétique d'ordre quatre par rapport à la concentration de l'activateur, un modèle de transfert énergétique à quatre corps interactifs basé sur une distribution aléatoire des donneurs et des accepteurs, ainsi que d'un modèle de transfert énergétique à deux corps interactifs basé sur une distribution uniforme des donneurs et des accepteurs ont été crées.

La dynamique de conversion du Tm³⁺:YBF a été étudiée avec un modèle de loi de vitesse comprenant deux processus de transferet énergétique. Une concordance satisfaisante a été obtenue avec ce modèle. Des mesures par sonde d'exitation de la dépendance à la température et à la puissance du gain de conversion de l'émission bleue à 482 nm provenant du Tm³⁺:YBF sont aussi présentées.

ACKNOWLEDGEMENTS

I would like to express my sincere gratitude to my supervisor, Professor David Simkin, for his guidance during the course of this work as well as for his encouragement during the challenging stages of this study.

I wish to thank Professor Martin Zuckermann for coming to my assistance on many occasions.

I would also like to thank Andrei Skirtach for providing me with good companionship.

I also thank Dr. Monique Marie Laberge for her help in getting my feet wet with the lab work when I joined the group.

As well, I would like to thank the Departments of Physics and Chemistry for providing a pleasant research climate.

TABL	E OF CONTENTS	Page
	ABSTRACT	i
	RÉSUMÉ	iii
	ACKNOWLEDGEMENT	v
	LIST OF FIGURES	хi
	LIST OF TABLES	xv
	CHAPTER 1	
	INTRODUCTION	1
1.1	Properties of the rare earth and laser	
	crystals	2
	1.1.1 Properties of the rare earth	2
	1.1.2 Properties of the laser crystals	2
1.2	Spectra and energy levels of rare earth ions	
	in Crystals	2
	1.2.1 Energy levels of Er3: YAG and	
	Er3+:YAlO3	5
	1.2.2 Energy levels of Tm3.:YLiF4 and	
	Tm ³⁺ :Y _z BaF ₈	5
1.3	Transition intensities and radiative decay	
	rates in rare-earth doped crystals	5
	1.3.1 Brief introduction	5
	1.3.2 Calculations of the radiative decay	
	rates in Er3+:YAG and Er3+:YAlO3	13
	1.3.3 Calculations of the radiative decay	
	rates in Tm ^{3*} :YLiF ₄ and Tm ^{3*} :Y ₂ BaF ₈	16

1.4	Energy transfer	16
	1.4.1 Brief introduction	16
	1.4.2 The Föster-Dexter transfer (two-body	
	interaction electric multipole transfer)	
	rate	20
	1.4.3 The Judd-ofelt parameter expression	
	of the two-body interaction electric	
	multipole transfer rate	29
1.5	Upconversion	30
	1.5.1 Brief introduction	30
	1.5.2 Basic rate equation model to describe	
	upconversion dynamics	31
	1.5.3 Avalanche upconversion	35
1.6	High (higher than two) order concentration	
	dependent energy transfer and concentration	
	dependent transfer parameter	40
	1.6.1 Observations	40
	1.6.2 The diffusion transfer model	42
	1.6.3 The many-body process	44
1.7	Statement of the problem	49
1.8	Objectives of the research	50
	CHAPTER 2	
	EXPERIMENTAL METHODS AND DATA TREATMENT	51
2.1	Time dependent upconversion intensity	
	measurements	52

	2.1.1 Upconversion emission in Er3: YAG and	
	YA103	52
	2.1.2 Upconversion emission in Tm3::YLiF, and	
	Y ₂ BaF ₈	53
2.2	Power dependence of the upconversion intensity	
	measurement	55
2.3	Pump-probe gain measurement	56
2.4	Data treatment	58
	2.4.1 Numerical methods for the solution of	
	the coupled rate equations	58
	2.4.2 Choice of parameters to vary and choice	
	of parameter values	60
	2.4.3 Fitting to more than one level when	
	possible	60
	2.4.4 Treatment of the gain data	60
	CHAPTER 3	
	RESULTS AND DISCUSSIONS	62
3.1	Upconversion dynamics of Er3-: YAG and	
	Er3+: YA103	63
3.2	Avalanche upconversion dynamics of	
	Tm ³⁺ :YLiF ₄	72
3.3	Upconversion dynamics and pump-probe	
	measurements of the upconversion gain in	
	Tm3+:Y2BaF8	98
3.4	Theoretical considerations	11

	3.4.1	Four-body interaction transfer model	114
	3.4.2	Energy transfer in a regular	
		distribution of donors and acceptors	
		(Regular model)	121
	3.4.3	Four-body model approach to the	
		upconversion dynamics of Er3+: YAG and	
		Er ³⁺ :YAlO ₃	129
	3.4.4	Regular model approach to the	
		upconversion dynamics of Er3+: YAG and	
		Er ³⁺ :YAlO ₃	131
	3.4.5	Four-body model approach to the	
		avalanche upconversion dynamics of	
		Tm ³⁺ :YLiF ₄	137
	3.4.6	Regular model approach to the avalanche	
		upconversion dynamics of Tm3-:YLiF4	141
3.5	Discus	ssions	145
	3.5.1	About the many-body interaction energy	
		transfer	145
	3.5.2	About the regular distribution of the	
		donors and acceptors	146
	3.5.3	About the two-dimensional transfer	150
	3.5.4	The influence of the energy transfer	
		parameters by structure of the compounds	151
	3.5.5	Analysis of the parameters	152
	CHAPT	ER 4	
	CONCL	USIONS AND SUMMARY OF THE CONTRIBUTIONS	

TO THE KNOWLEDGE	154
4.1 Conclusions	155
4.2 Summary of the contributions to the knowledge.	156
4.3 Suggestions for future work	157
APPENDIX	158
1. Error analysis	158
2. Assumptions in the energy transfer models	158
REFERENCES	160

LIST	OF FIGURES	Page
1.1	Energy levels of Er3::YAG and Er3::YAlO3	7
1.2	Absorption spectrum of Tm3+:Y2BaF8	9
1.3	Emission spectrum of Tm ³ *:Y ₂ BaF ₈	10
1.4	Energy levels of Tm3+:YLiF4 and Tm3+:Y2BaF8	11
1.5	Two-atom system	20
1.6	Two-atom system in solid	23
1.7	Three-level scheme for an avalanche process	37
2.1	Optical arrangement for the time dependent	
	upconversion emission measurement	54
2.2	Optical arrangement for the pump-probe gain	
	measurement	57
3.1	Energy level scheme of Er3+ showing the energy	
	transfer and decay processes considered in the	
	rate equations for the upconversion dynamics	
	of Er ³⁺ :YAG and Er ³⁺ :YAlO ₃	64
3.2	Time dependence of the upconversion emission	
	at 550 nm ($^4S_{3/2}$) and 650 nm ($^4F_{9/2}$) from	
	Er3+:YAlO3 at room temperature, subsequent	
	to a 15 ns pulse at ca. 1550 nm	67
3.3	Time dependence of the upconversion emission	
	at 550 nm ($^4S_{3/2}$) and 650 nm ($^4F_{9/2}$) from	
	Er3+: YAG at room temperature, subsequent to	
	a 15 ns pulse at ca. 1550 nm	68
3.4	Dependence of the upconversion emission	
	intensity of Er3+:YAlO3 on cw 1550 nm laser	

	power	71
3.5	Rise time behaviour of the upconversion	
	emission of Tm ³⁺ :YLiF ₄ under 370 mW/	
	$3.42\times10^{-5}\text{cm}^2$ and σ polarization pump at	
	different pump wavelengths	73
3.6	Rise time behaviour of the upconversion	
	emission of Tm ³⁺ :YLiF ₄ under 370 mW/	
	$3.42\times10^{-5}\mathrm{cm^2}$ and π polarization pump at	
	different pump wavelengths	74
3.7	Energy level scheme of Tm3+ showing the	
	energy transfer, the pump and the decay	
	processes considered in the rate equations	
	for the avalanche upconversion dynamics of	
	Tm ³⁺ :YLiF ₄	75
3.8	Dependence of the 487 nm upconversion	
	emission intensity of Tm3+:YLiF4 on	
	627 nm σ polarization laser power at 12K	78
3.9	Dependence of the 487 nm upconversion	
	intensity rise time of Tm3+:YLiF4 on	
	627 nm σ polarization laser power at 12K	79
3.10	Time dependence of the upconversion	
	emission of Tm^{3+} :YLiF ₄ at 487 nm ($^3H_6 \leftarrow {}^1G_4$)	
	and 12 K under 30 mw/3.42×10 ⁻⁵ cm ² 627 nm and σ	
	polarization pump	83
3.11	Simulations of the dependence of the 487 nm	
	upconversion intensity rise time of Tm3+:YLiF4	

	on 627 nm σ polarization laser pump at 12 K	88
3.12	Time dependence of the upconversion emission	
	of Tm^{3+} :YLiF ₄ at 487 nm ($^3H_6 \leftarrow {}^1G_a$) and 452 nm	
	$(^{3}F_{4} \leftarrow ^{1}D_{2})$ at 12 K under 370 mw/3.42×10 ⁻⁵ cm ²	
	σ polarization 627 nm pump	91
3.13	Time dependence of the upconversion emission	
	of Tm^{3+} : YLiF ₄ at 487 nm ($^3H_6 \leftarrow {}^1G_4$) and 452 nm	
	$({}^{3}F_{4} \leftarrow {}^{1}D_{2})$ at 12 K under 370 mw/3.42×10 ⁻⁵ cm ²	
	σ polarization 646 nm pump	92
3.14	Time dependence of the upconversion emission	
	of Tm^{3+} : YLiF ₄ at 487 nm ($^3H_6 \leftarrow {}^1G_4$) and 452 nm	
	$(^{3}F_{4} \leftarrow ^{1}D_{2})$ at 12 K under 370 mw/3.42×10 ⁻⁵ cm ²	
	π polarization 629 nm pump	93
3.15	Time dependence of the upconversion emission	
	of Tm^{3+} :YLiF ₄ at 487 nm ($^3H_6 \leftarrow {}^1G_4$) and 452 nm	
	$(^{3}F_{4} \leftarrow ^{1}D_{2})$ at 12 K under 370 mw/3.42×10 ⁻⁵ cm ²	
	π polarization 641 nm pump	94
3.16	Time dependence of the upconversion emission	
	of Tm^{3+} :YLiF ₄ at 487 nm ($^3H_6 \leftarrow {}^1G_4$) and 452 nm	
	$(^{3}F_{4} \leftarrow ^{1}D_{2})$ at 300 K under 370 mw/3.42×10 ⁻⁵ cm ² σ	
	polarization 650 nm pump	95
3.17	Time dependence of the upconversion emission	
	of Tm^{3+} : YLiF ₄ at 487 nm ($^3H_6 \leftarrow {}^1G_4$) and	
	452 nm (${}^3F_4 \leftarrow {}^1D_2$) at 300 K under 370 mw/	
	3.42×10^{-5} cm ² π polarization 654 nm pump	96
3.18	Energy level scheme of Tm3+ showing the	

	energy transfer the pump and the decay	
	processes considered in the rate equations	
	for the upconversion dynamics of $Tm^{3+}:Y_2BaF_8$	101
3.19	Time dependence of the upconversion emission	
	of $Tm^{3+}Y_2BaF_8$ at 491 nm ($^3H_6 \leftarrow {}^1G_4$) and 464 nm	
	$(^{3}F_{4} \leftarrow ^{1}D_{2})$ at 12 K under 260 mw/3.42×10 ⁻⁵ cm ²	
	628.5 nm pump	104
3.20	Time dependence of the upconversion emission	
	of $\text{Tm}^{3+}\text{Y}_2\text{BaF}_8$ at 488 nm ($^3\text{H}_6\leftarrow ^1\text{G}_4$) and 462 nm	
	$(^3F_4 \leftarrow ^1D_2)$ at 300 K under 350 mw/3.42×10 ⁻⁵ cm ²	
	628.5 nm pump	105
3.21	Upconversion emissions spectra of Tm3+Y2DaF8	
	at various temperatures	109
3.22	Pump power dependence of the 482.10 nm	
	$(^{3}H_{6}^{1}G_{4})$ emission upconversion gain in	
	Tm ³⁺ Y ₂ BaF ₈	110
3.23	Broad upconversion gain spectrum of Tm3+Y2BaF8	
	at 120 K for a pump wavelength of 628 nm and	
	a probe wavelength centred at 482.10 nm	111
3.24	Diagrams showing the regular and non-regular	
	distribution of the donors and acceptors	147
3.25	Diagram showing the two-dimensional transfer .	150

LIST	OF TABLES	Page
1.1	Basic properties of rare earth elements	3
1.2	Properties of laser crystals YAG, YAlO3,	
	YLiF ₄ , and Y ₂ BaF ₈	4
1.3	Energy levels of Er3+:YAG and Er3+:YAlO3	6
1.4	Energy levels of Tm3+:YLiF4 and Tm3+:Y2BaF8	8
1.5	Intensity parameters Ω_{λ} (λ =2, 4, 6) for	
	Er ³⁺ :YAG and Er ³⁺ :YAlO ₃	13
1.6	Reduced matrix elements $U^{2}(\lambda) = \langle J U^{(\lambda)} J' \rangle^{2}$ for	
	Er ³⁺	14
1.7	Calculated dipole transition radiative decay	
	rates in Er3+:YAG and Er3+:YAlO3	15
1.8	Intensity parameters $\Omega_{\lambda}(\lambda=2,4,6)$ for $\text{Tm}^{3+}:\text{YLiF}_4$	
	and Tm ³⁺ :Y ₂ BaF ₈	16
1.9	Reduced matrix elements $U^2(\lambda) = \langle J \ U^{(\lambda)} \ J' \rangle^2$	
	for Tm ³⁺	17
1.10	Calculated dipole transition radiative decay	
	rates in Tm^{3+} :YLiF ₄ and Tm^{3+} :Y ₂ BaF ₈	18
3.1	Fixed radiative decay rates in the fitting	
	of the time dependent upconversion emission	
	intensity experimental data of Er3+: YAG and	
	Er ³⁺ :YAlO ₃	66
3.2	Fitted values of the nonradiative decay rates	
	and energy transfer parameters in the fitting	
	of the time dependent upconversion emission	
	intensity experimental data of Er3+:YAG and	

	Er3-: YA103	70
3.3	Dependence of upconverted emission and	
	intensity (I) on 1550 nm pump power (P),	
	according to I=Pm	72
3.4	Resonances for the three different pump	
	wavelengths at each of the two different	
	polarizations	76
3.5	Fixed radiative decay rates in fitting the	
	time dependent upconversion 487 nm emission	
	experimental data of Tm3+:YLiF4 under	
	30 mW/3.42×10 ⁻⁵ cm ² pump	82
3.6	Parameters obtained from the fitting of the	
	time dependent upconversion 487 nm emission	
	experimental data of Tm3+:YLiF4 under 30 mW/	
	$3.42 \times 10^{-5} \text{cm}^2$ pump compared with the calculated	
	values	84
3.7	Fixed radiative decay rates in the fitting of	
	the time dependent upconversion emissions of	
	Tm^{3+} :YLiF ₄ under 370 mW/3.42×10 ⁻⁵ cm ² pump	97
3.8	Values of the parameters found in the	
	fitting of the time dependent upconversion	
	emissions of Tm^{3+} :YLiF4 under σ polarization	
	370 mW/3.42×10 ⁻⁵ cm ² pump	99
3.9	Values of the parameters found in the	
	fitting of the time dependent upconversion	
	emissions of Tm3+.VLiE, under # nolarization	

	370 mW/3.42×10 ⁻⁵ cm ² pump	100
3.10	Fixed radiative decay rates in the fittings	
	of the time dependent upconversion emission	
	experimental data of Tm3+:Y2BaF8	106
3.11	Values of parameters obtained from the	
	fittings of the time dependent upconversion	
	emission experimental data of Tm3+:Y2BaF8	
	compared with the calculated values	107
3.12	Measured gain for three emission lines in	
	the ${}^{1}G_{4} \rightarrow {}^{3}H_{6}$ (475.0 nm: 21183 cm $^{-1} \rightarrow$ 119 cm $^{-1}$,	
	482nm: 20883 cm ⁻¹ \rightarrow 141 cm ⁻¹ , 486.0 nm: 20883	
	$cm^{-1} \rightarrow 186 cm^{-1}$) manifold of $Tm^{3+}: Y_2BaF_8 \dots$	113
3.13	Values of the fourth-order energy transfer	
	parameters obtained from the fittings of	
	the time dependent upconversion emission	
	experimental data of Er3+:YAG and Er3+:YAlO3	
	compared with that calculated from the	
	Judd-Ofelt parameters for the four-body	
	transfer	130
3.14	Values of the fourth-order energy transfer	
	parameters obtained from the fittings of	
	the time dependent upconversion emission	
	experimental data of Er3+:YAG and Er3+:YAlO3	
	compared with that calculated from the	
	Judd-Ofelt parameters (for the regular	
	distribution two-body interaction	

	dipole-dipole transfer)	132
3.15	Energy transfer parameters obtained from the	
	σ polarization fittings compared with those	
	calculated from the Judd-Ofelt parameters (for	
	the four-body transfer)	138
3.16	Energy transfer parameters obtained from the	
	Tm^{3+} :YLiF ₄ π polarization fittings compared	
	with those calculated from the Judd-Ofelt	
	parameters (for the four-body energy transfer)	139
3.17	Energy transfer parameters obtained from the	
	Tm³:Y2BaF8 fittings compared with those	140
	calculated from the Judd-Ofelt parameters (for	
	the four-body energy transfer)	
3.18	Energy transfer parameters obtained from the	
	σ polarization fitting compared with those	
	calculated from the Judd-Ofeld parameters	
	(for the regular distribution two-body	
	interaction dipole-dipole transfer)	142
3.19	Energy transfer parameters obtained from	
	the Tm^{3+} :YLiF ₄ π polarization fitting comparing	
	with those calculated from the Judd-Ofeld	
	parameters (for the regular distribution	
	two-body interaction dipole-dipole transfer) .	143
3.20	Energy transfer parameters obtained from	
	the Tm3+:Y2BaF8 fitting comparing with those	
	calculated from the Judd-Ofeld parameters	

- xix ~

144
152
153

e e

CHAPTER 1

INTRODUCTION

1.1 Properties of the rare earth and laser crystals

1.1.1 Properties of the rare earth

The rare earths form a group of chemically similar elements which have in common an open 4f shell. They are chiefly trivalent and it is principally the properties of the trivalent ions which are important rather than those of the neutral atoms. Table 1.1 gives a summary of the basic properties of the trivalent rare earths (in order of the atomic number Z), which includes the electron configuration, the ground term, the Landé factor g_J , the max ESR $[2M_J(max) \cdot g_J]$ g factor, and the ionic radius R.

1.1.2 Properties of laser crystals

Table 1.2 gives the main physical properties of the laser crystals YAG, YAlO3, YLiF4, and Y2BaF8 including the refractive index n, the density of the crystals ρ , the density of Yttrium in the crystals ρ_Y , the concentration of Yttrium n_Y , the nearest neighbour distance between two Yttrium ions a_Y , the space group, the cation-site symmetry, and the lattice constants (a, b, and c).

1.2 Spectra and energy levels of rare earth ions in Crystals

The crystal spectra (absorption spectra and fluorescence spectra) reflect the modifications in the free ion energy level structure by the electric crystal field to which the rare earth ions are subjected. The detailed information of the

Table 1.1 Basic properties of rare earth elements[1], [2].

Z	E	Electron	Ground	g _J	g	R (Å)
		configuration	term			
57	La	4f ⁰ 5s ² 5p ⁶	¹ S ₀	0	0	1.15
58	Ce	4f ¹ 5s ² 5p ⁶	² F _{5/2}	6/7	4.29	1.02
59	Pr	4f ² 5s ² 5p ⁶	³ H ₄	4/5	6.40	1.00
60	Nd	4f³5s²5p6	4I _{9/2}	8/11	6.55	0.99
61	Pm	4f45s25p6	⁵ I ₄	3/5	4.80	0.98
62	Sm	4f ⁵ 5s ² 5p ⁶	6H _{5/2}	2/7	1.43	0.97
63	Eu	4f ⁶ 5s ² 5p ⁶	⁷ F₀	0	0	0.97
64	Gd	4f ⁷ 5s ² 5p ⁶	⁸ S _{7/2}	2	14	0.97
65	Tb	4f85s25p6	⁷ F ₆	3/2	18	1.00
66	Dy	4f ⁹ 5s ² 5p ⁶	⁶ H _{15/2}	4/3	20	0.99
67	Но	4f ¹⁰ 5s ² 5p ⁶	⁵ I ₈	5/4	20	0.97
68	Er	4f ¹¹ 5s ² 5p ⁶	⁴ I _{15/2}	6/5	18	0.96
69	Tm	4f ¹² 5s ² 5p ⁶	³ H ₆	7/6	14	0.95
70	Yb	4f ¹³ 5s ² 5p ⁶	² F _{7/2}	8/7	8	0.94
71	Lu	4f ¹⁴ 5s ² 5p ⁶	¹ S ₀	0	0	0.93

Table 1.2 properties of the laser crystals YAG, YAlO3, YLiF4 and $Y_2BaF_8[2],[3],[4],[5]$.

	YAG	YA10 ₃	YLiF ₄	Y ₂ BaF _e
n	1.929	1.815	1.46	
ρ (g.cm ₋₃)	4.55	5.35	3.968	5.047
ρ _γ (g.cm ₋₃)	2.04	2.90	2.052	1.921
n _y (cm ⁻³)	1.381×10 ²²	1.964×10 ²²	1.389×10 ²²	1.300×10 ²²
a _y (Å)	5.17	4.60	5.16	5.28
Space group	O _h 10-la3d	D _{2h} 16-Pbnm	C _{4h} 6-I4 ₁ /a	C _{2h} ³ -C2/m
cation-site	D ₂ (Y ³⁺)	C _s (Y ³⁺)	S ₄ (Y ³⁺)	• • •
symmetry				
a (Å)	12	5.176	5.175	4.260
ъ (Å)	12	5.307	5.175	6.302
c (Å)	12	7.355	6.498	6.302

energy level structure is important to the study of the kinetics of energy transfer and the dynamics of upconversion.

1.2.1 Energy levels of Er3+:YAG and Er3+:YAlO3

The energy levels of Er³⁺:YAG and Er³⁺:YAlO₃ were obtained from the absorption and emission spectra[6],[7]. Those results are listed in Table 1.3 and shown in Figure 1.1.

1.2.2 Energy levels of Tm3+:YLiF4 and Tm3+:Y2BaF8

The energy levels of Tm³⁺:YLiF₄ and Tm³⁺:Y₂BaF₈ are listed in Table 1.4 and shown in Figure 1.4. The information of the Tm³⁺:YLiF₄ energy levels were obtained from reference[8]. The excited state levels and their Stark splitting of Tm³⁺ in Y₂BaF₈ were obtained from the absorption spectrum acquired by D. J. Simkin (shown in Figure 1.2). The ground state level and its Stark splitting of Tm³⁺ in Y₂BaF₈ were obtained from the emission spectrum shown in Figure 1.3.

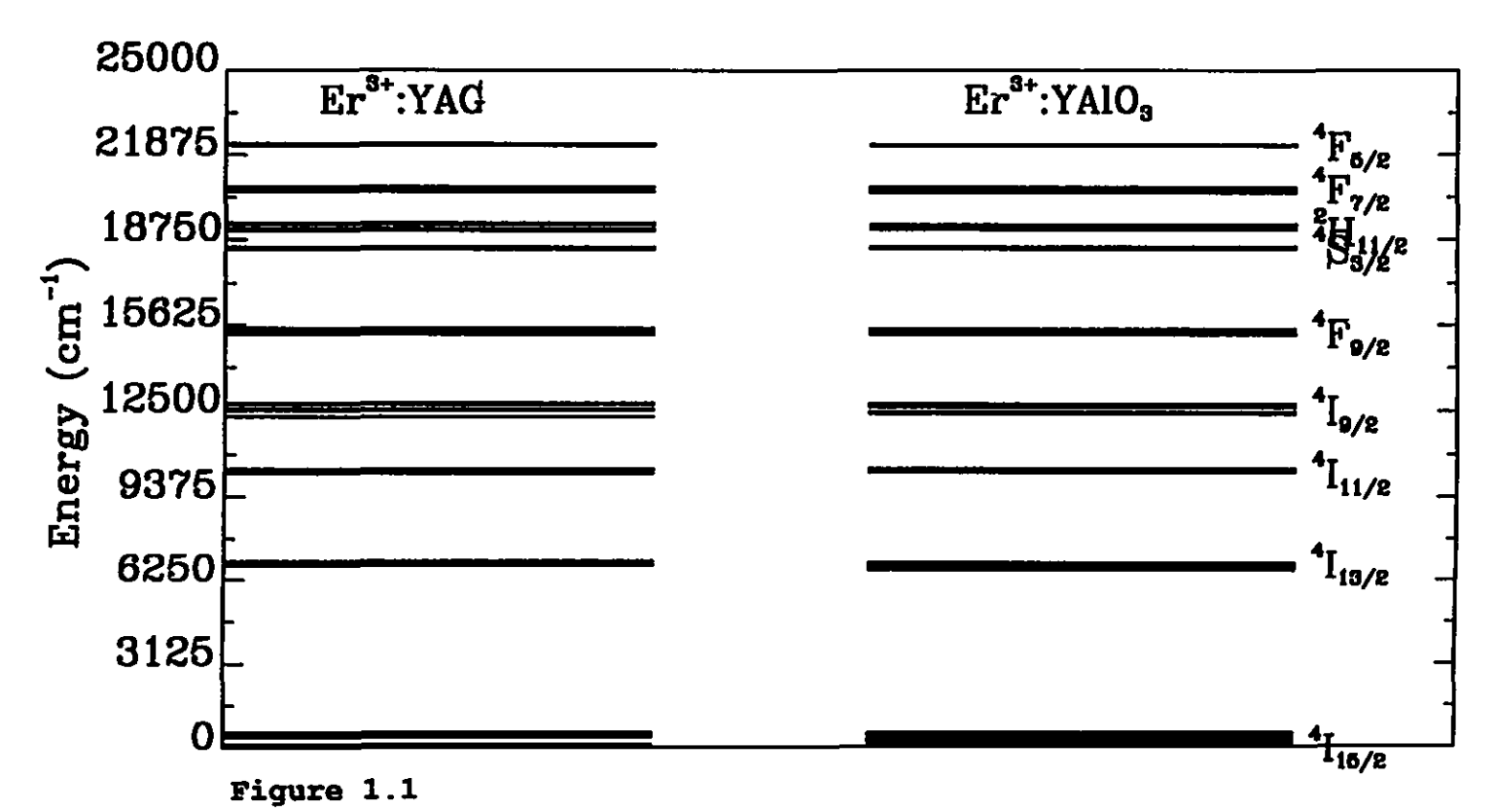
1.3 Transition intensities and radiative decay rates in rareearth doped crystals

1.3.1 Brief introduction

Electric dipole transitions between the states of 4f^N electron configuration of an isolated rare-earth ion are prohibited by the parity selection rule[9]. This prohibition, as was shown by Van Vleck[10] can be avoided due to non-central symmetric interaction of the rare earth

Table 1.3 Energy levels of Er3+:YAG[6] and Er3-:YAlO3[7].

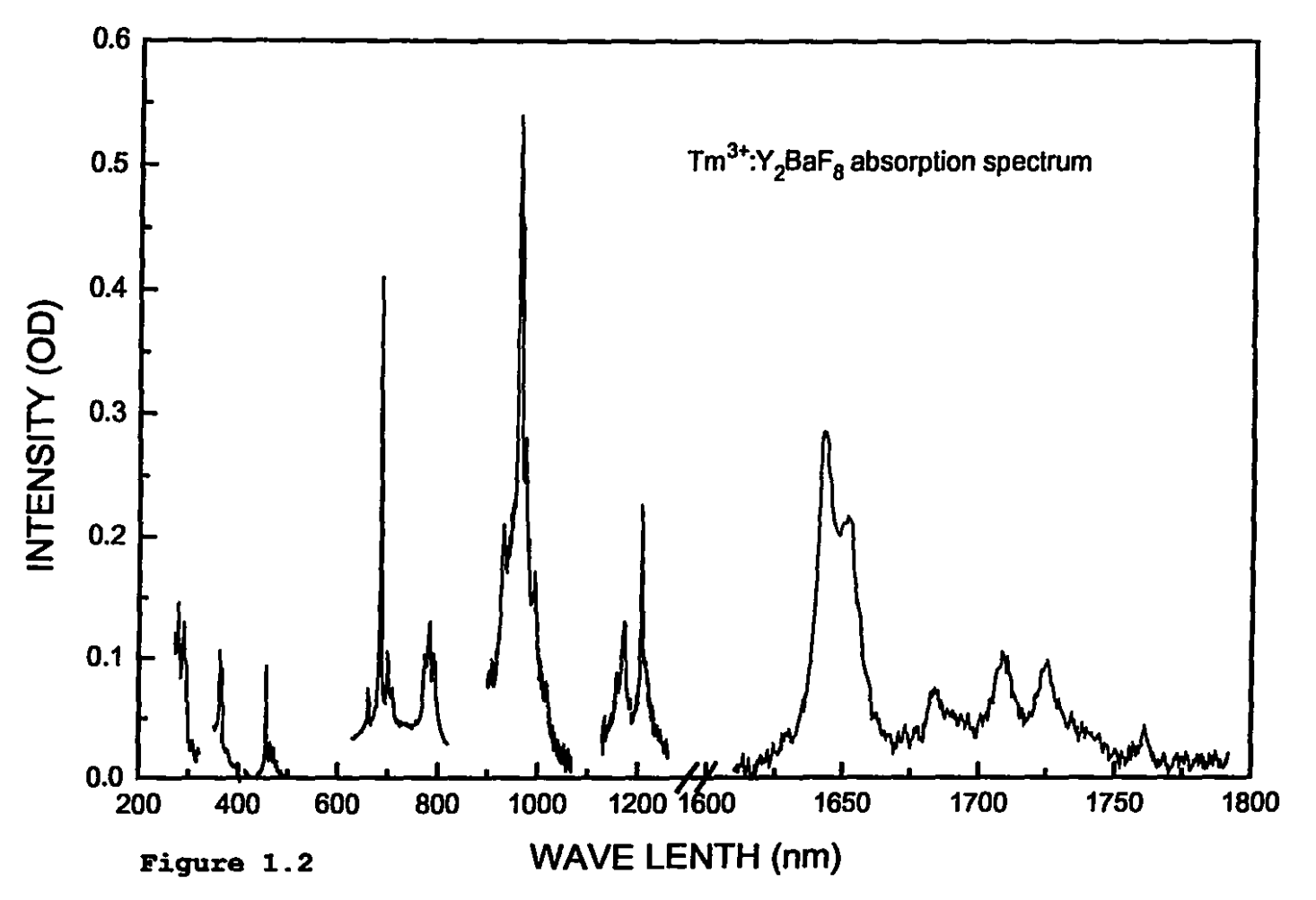
	els of Er : IAG[6] an	
Er ³⁺ :YAG (cm ⁻¹)	Er ³⁺ :YAlO ₃ (cm ⁻¹)	SLJ
24 116 412 426 468 564	51 218 266 388 443 516	⁴ I _{15/2}
6766 6858 6949	6602 6641 6669 6773 6814 6868	⁴ I _{13/2}
10252 10281 10360 10370 10411	10282 10293 10322 10347 10402	⁴ I _{11/2}
12298 12573 12719 12765	12393 12624 12648 12732	⁴ I _{9/2}
15290 15319 15364 15485 15530	15263 15344 15374 15396 15481	⁴ F _{9/2}
18406 18470	18406 18487	⁴ S _{3/2}
19100 . 19161 19328 19350 19367	19119 19190 19240 19275 19303	² H _{11/2}
20520 20574 20625 20659 20709	20482 20554 20617 20685	⁴ F _{7/2}
22230 22250 22299	22196 22227 22259	⁴ F _{5/2}



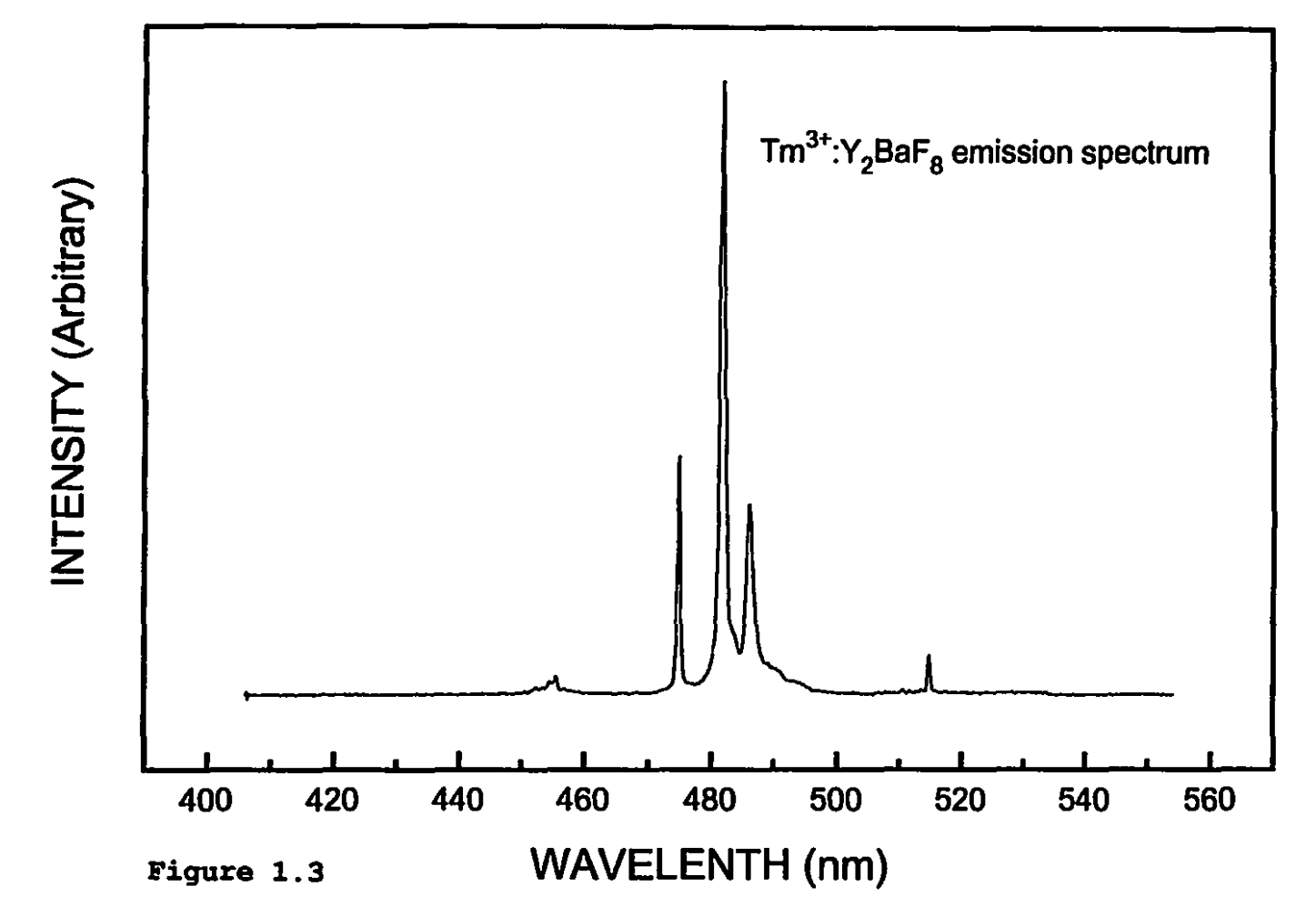
Energy levels of Er3+:YAG and Er3+:YAlO3.

Table 1.4 Energy levels of Tm3+:YLiF4[8] and Tm3+:Y2BaF8

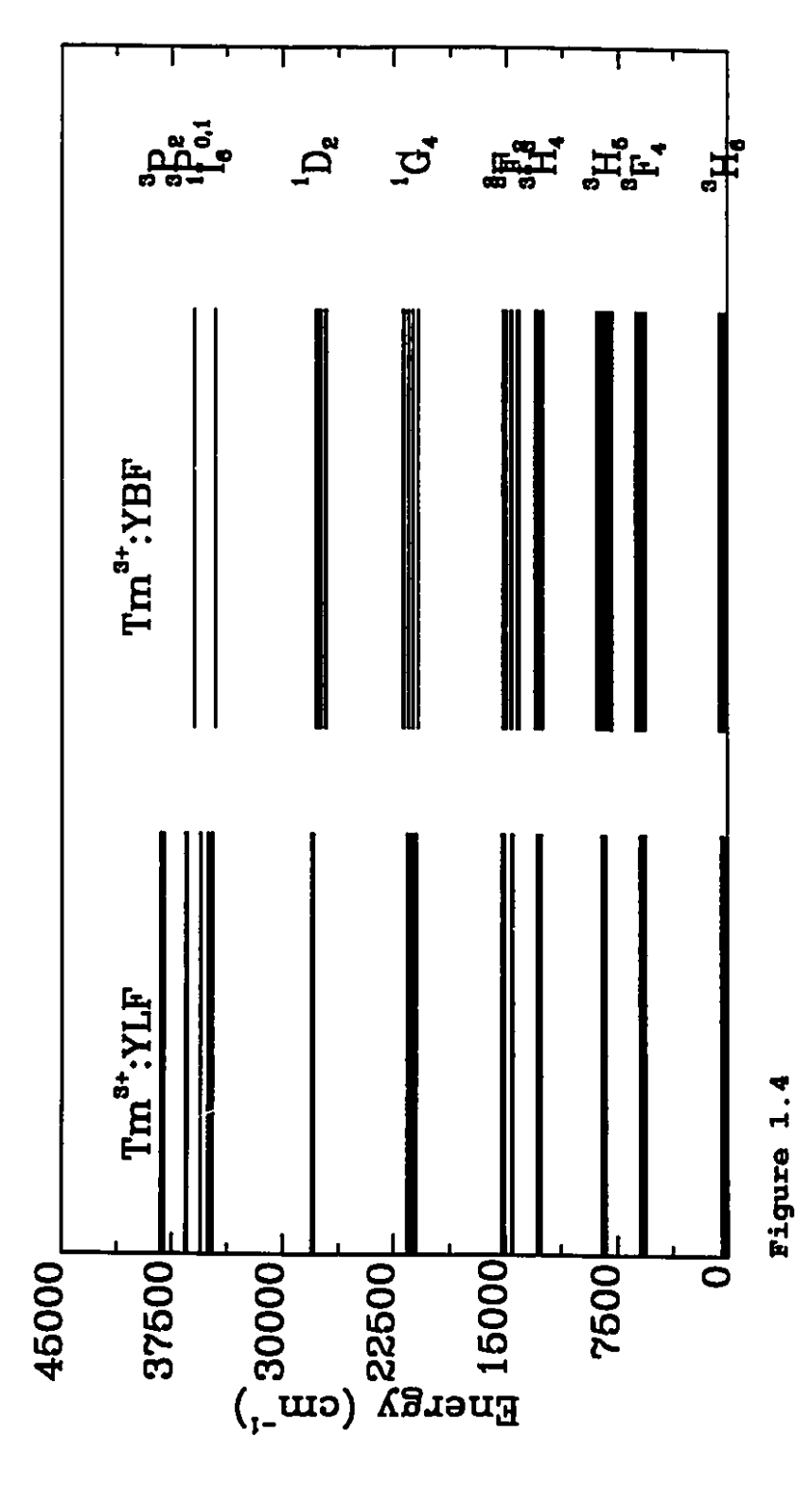
Table	r Energy	levers or im	. 1111	Alol and Im	• 12Bar 8
SLJ	Tm ³⁺ :YLiF ₄ (cm ⁻¹)	Tm ³⁺ :Y ₂ BaF ₈ (cm ⁻¹)	SLJ	Tm ³⁺ :YLiF ₄ (cm ⁻¹)	Tm ³⁺ :Y ₂ BaF ₈ (cm ⁻¹)
³ H ₆	0 30 56 270 305 319 334 372 407 419	0 59 110 169 200 246 307 350 417 478	³ F ₄	5599 5756 5757 5820 5942 5968 5972	5681 5797 5848 5939 6051 6087
³ H ₅	8284 8300 8319 8501 8519 8535	8286 8529 8630 8676 8826	³ H ₄	12599 12624 12643 12745 12804 12835 12891	12616 12786 12934
³ F ₃	14520 14549 1459400 14597	14115 14309 14602 14634	³ F ₂	15094 15203 15275	15130 15166
¹ G ₄	20973 21186 21272 21300 21554 21562	20583 20992 21134 21244 21555 21946	¹D ₂	27961 27911 28053 28075	27271 27411 27498 27618 27693 27833
¹ I ₆	34729 34778 34769 34999 34998	34627	³ P ₀	35538	35420 35597 35774 35993
³ P ₁	36470 36566				



Absorption spectrum of $Tm^{3+}:Y_2BaF_8$.



Emission spectrum of Tm^{3+} : Y_2BaF_8 .



Energy levels of Tm3+:YLiF4 and Tm3+:Y2BaF8.

ions with the surroundings, which mixes states of opposite parity. Judd[11] and Ofelt[12], working independently and simultaneously, obtained the line strength for electric dipole transitions

$$S_{\text{ed}}(J;J') = \frac{1}{e^2} \sum_{J_z J_z'} |\langle A | P_q^{(1)} | A \rangle|^2$$

$$= \sum_{\lambda=2,4,6} \Omega_{\lambda} |\langle J | U^{(\lambda)} | J \rangle|^2$$
(1.1)

where $\langle J | | U^{(\lambda)} | J' \rangle$ is a reduced matrix element of the irreducible tensor operator of rank λ and Ω_{λ} are the intensity parameters. The line strength $S_{\rm ed}(J;J')$ determined by (1.1) is associated with the spontaneous decay rate by:

$$A_{ed}(J;J') = \frac{64\pi^4 e^2 v^3}{3hc^3(2J+1)} \frac{n(n^2+2)^2}{9n} s_{ed}(J;J')$$
 (1.2)

where n is the refractive index, c is the velocity of light in vacuum and ν is wave number of the transition. Including the magnetic dipole transition the total decay rate is

$$A = \frac{64\pi^4 e^2 v^3}{3hc^3 (2J+1)} \left[\frac{(n^2+2)^2}{9n} S_{ed} + n^3 S_{ed} \right]$$
 (1.3)

in the above equation S_{md} are determined in the following way [13]:

If J'=J

$$S_{md} = (\frac{eh}{2mc})^{2} \cdot \frac{2J+1}{4J(J+1)} \cdot \delta(S, S') \cdot \delta(L, L')$$

$$: [S(S+1) - L(L+1) + 3J(J+1)]^{2}$$
(1.4)

If J'=J-1

$$S_{md} = (\frac{eh}{4\pi mc})^{2} \cdot \delta(S, S') \cdot \delta(L, L')$$

$$\cdot [(S+L+1)^{2} - J^{2}] [J^{2} - (L-S)^{2}] / 4J$$
(1.5)

If J'=J+1

$$S_{md} = \left(\frac{eh}{4\pi mc}\right)^{2} \cdot \delta(S, S') \delta(L, L')$$

$$\cdot \left[(S+L+1)^{2} - (J+1)^{2} \right] \left[(J+1)^{2} - (L-S)^{2} \right] / \left[4(J+1) \right]$$
(1.6)

1.3.2 Calculations of the radiative decay rates in Er3+:YAlO3 and Er3+:YAG

The intensity parameters $\Omega_{\lambda}(\lambda=2,4,6)$ for Er³*:YAG and Er³*:YAlO3 were obtained from reference [13] and are listed in Table 1.5.

Table 1.5 Intensity parameters $\Omega_{\lambda}(\lambda=2,4,6)$ for Er³⁺:YAG and Er³⁺:YAlO₃[13]

Ω_2 (10 ⁻²⁰ cm ²)	$\Omega_{\rm q}$ (10 ⁻²⁰ cm ²)	$\Omega_{\rm 6}$ (10 ⁻²⁰ cm ²)
0.19	1.68	0.62
1.06	2.63	0.78
	0.19	0.19 1.68

The reduced matrix elements $U^2(\lambda) = \langle J | U^{(\lambda)} | J' \rangle^2$ for Er^{3^+} listed in Table 1.6 are obtained from reference[14] and [15]. The dipole transition decay rates can be calculated using equation (1.3). Table 1.7 gives the results of the calculated dipole transition decay rates for Er^{3^+} :YAG and Er^{3^+} :YAlO₃.

Table 1.6 Reduced matrix elements $U^2(\lambda) = \langle J | U^{(\lambda)} | J' \rangle^2$ for $Er^{3+}[14], [15]$.

SLJ	S'L'J'	U² (2)	U ² (4)	U² (6)
⁴ I _{13/2}	⁴ I _{15/2}	0.0188	0.1176	1.4617
⁴ I _{11/2}	⁴ I _{15/2}	0.0259	0.0001	0.3994
	4I _{13/2}	0.021	0.11	1.04
⁴ I _{9/2}	⁴ I _{15/2}	0.0	0.1452	0.0064
	⁴ I _{13/2}	0.0003	0.0081	0.64
4F _{9/2}	⁴ I _{15/2}	0.0	0.5655	0.4651
	⁴ I _{13/2}	0.0096	0.1576	0.0870
	⁴ I _{11/2}	0.0671	0.0088	1.2611
	4I _{9/2}	0.096	0.0061	0.012
⁴ S _{3/2}	⁴ I _{15/2}	0.0	0.0	0.2285
	⁴ I _{13/2}	0.0	0.0	0.3481
	⁴ I _{11/2}	0.0	0.0037	0.0789
	⁴ I _{9/2}	0.0	0.0729	0.2560

Table 1.7 Calculated dipole transition radiative decay rates in Er³⁺:YAG and Er³⁺:YAlO₃

SLJ	S'L'J'	A (s ⁻¹)	A(s ⁻¹)
	,	Er³+:YAG	Er3+:YA103
⁴ I _{13/2}	⁴ I _{15/2}	73.34	92.1
⁴ I _{11/2}	⁴ I _{15/2}	74.43	102.3
	⁴ I _{13/2}	9.7	14.5
⁴ I _{9/2}	⁴ I _{15/2}	155.7	253.9
	⁴ I _{13/2}	24.4	34.2
⁴ F _{9/2}	⁴ I _{15/2}	1537	2306
	⁴ I _{13/2}	72.3	113.0
	⁴ I _{11/2}	36.5	48.1
	4I _{9/2}	.22	.8
⁴ S _{3/2}	⁴ I _{15/2}	782.0	991.6
	⁴ I _{13/2}	315.0	405.0
d I	4I _{11/2}	27.4	35.5
	⁴ I _{9/2}	49.0	69.5

1.3.3 Calculations of the radiative decay rates in Tm³⁺:YLiF₄ and Tm³⁺:Y₂BaF₈

The intensity parameters $\Omega_{\lambda}(\lambda=2,4,6)$ for $\text{Tm}^{3+}:Y\text{LiF}_{4}$ were obtained by M. Dulick et al[8], for $\text{Tm}^{3+}:Y_{2}\text{BaF}_{8}$ were obtained by B. M. Antipenko[16]. The results are listed in Table 1.8.

Table 1.8 Intensity parameters $\Omega_{\lambda}(\lambda=2,4,6)$ for Tm³⁺:YLiF₄[8] and Tm³⁺:Y₂BaF₈[16]

Crystal	Ω_2 (10 ⁻²⁰ cm ²)	$\Omega_{\rm c}$ (10 ⁻²⁰ cm ²)	$\Omega_{\rm c}$ (10 ⁻²⁰ cm ²)
Tm3+:YLiF4	2.43	1.08	0.67
Tm³+:Y₂BaF _e	1.20	0.94	1.20

The reduced matrix elements $U^2(\lambda) = \langle J | U^{(\lambda)} | J' \rangle^2$ for Tm^{3+} were calculated by R. Reisfeld and L. Boehm[17] and are listed in Table 1.9. Using their results and the above intensity parameters we calculated the radiative decay rates in $Tm^{3+}:YLiF_4$ and $Tm^{3+}:Y_2BaF_8$ which are listed in Table 1.10.

1.4 Energy transfer

1.4.1 Brief introduction

When a material is exposed to a source of radiation, some of the energy may be absorbed through the creation of electronic excited states. This energy is later dissipated through the emission of light (radiative process) or heat

Table 1.9 Reduced matrix elements $U^2(\lambda) = \langle J | U^{(\lambda)} | J' \rangle^2$ for $Tm^{3+}[17]$

SLJ	S'L'J'	U ² (2)	U ² (4)	ប² (6)
¹ I ₆	³ H ₆	0.0108	0.0397	0.0137
¹ I ₆	³ F ₄	0.0549	0.4543	0.3658
¹ I ₆	³ H ₅	0.0010	0.0021	0.0057
¹ I ₆	³ F ₂ ³ F ₃ ³ H ₄	0.0 0.0 0.0676	0.0394 0.0028 0.3175	0.3373 0.0075 0.1035
¹ I ₆	¹ G ₄	0.2194	1.2894	0.6520
¹ I ₆	¹ D ₂	0.0	0.0515	0.8433
¹ D ₂	³ H ₆	0.0	0.3144	0.0916
¹ D ₂	3F.4	0.5792	0.0968	0.0194
¹ D ₂	3H5	0.0	0.0017	0.0164
¹ D ₂	³ F ₂ ³ F ₃ ³ H ₄	0.0639 0.1637 0.1147	0.3093 0.0714 0.0138	0.0 0.0 0.2307
¹D ₂	¹ G ₄	0.1926	0.1666	0.0006
¹ G ₄	³ H ₆	0.0452	0.0694	0.0122
¹G₄	³ F ₄	0.0042	0.0186	0.0642
¹G₄	³ H ₅	0.0704	0.0055	0.5176
¹G₄	³ F ₂ ³ F ₃ ³ H ₄	0.0050 0.0100 0.1511	0.0695 0.0698 0.0046	0.0413 0.2915 0.3750
³ F ₂ ³ F ₃ ³ H ₄	³ H ₆	0.0 0.0 0.2187	0.0 0.3163 0.0944	0.2591 0.8409 0.5758
³ F ₂ ³ F ₃ ³ H ₄	³ F ₄	0.2849 0.0031 0.1215	0.0548 0.0011 0.1329	0.0448 0.1654 0.2258
³ H ₄	³ H ₅	0.0152	0.4669	0.0153
³ F ₄	³ H ₆	0.5589	0.7462	0.2574

Table 1.10 Calculated dipole transition radiative decay rates in Tm^{3+} : YLiF₄ and Tm^{3+} : Y₂BaF₈

SLJ	S'L'J'	Tm ³⁺ :YLiF ₄ A(s ⁻²)	Tm ³⁺ : Y ₂ BaF ₈ A(s ⁻¹)
¹ I ₆	³ H ₆	492	420
¹ I ₆	³ F ₄	3241	3475
¹ I ₆	³ H ₅	24	28
¹ I ₆	³ F ₂ ³ F ₃ ³ H ₄	310 10 947	510 15 828
¹ I ₆	¹ G ₄	876	838
¹ I ₆	¹ D ₂	30	51
¹ D ₂	³ H ₆	3388	3427
¹ D ₂	³ F ₄	6576	3490
¹ D ₂	³ H ₅	38	63
¹ D ₂	³ F ₂ ³ F ₃ ³ H ₄	408 456 631	306 253 602
¹ D ₂	¹ G ₄	75	45
¹ G ₄	³ H ₆	399	277
¹ G ₄	³ F ₄	60	82
¹ G ₄	³ H ₅	167	297
¹ G ₄	³ F ₂ ³ F ₃ ³ H ₄	6 20 88	6 30 90
³ F ₂ ³ F ₃ ³ H ₄	³ H ₆	228 749 434	409 1081 444
³ F ₂ ³ F ₃ ³ H ₄	³ F ₄	253 22 43	145 38 39
³ H ₄	³ H ₅	6	11
³ F ₄	³ H ₆	89	64

(mutiphonon process). In between the creation of electronic excited states and the subsequent energy dissipation, the energy may move around from one atom or molecule to another within the material. This process is called "energy transfer". This phenomenon occurs in many different types of materials under a wide variety of physical conditions. Thus energy transfer is an important topic for study by physicists, chemists, and biologists with many different specialized research interests.

Energy transfer can occur by three different mechanisms. In the first mechanism, photoconductivity, the incident radiation creates free electron-hole pairs. These free electrons and/or holes can then migrate through the solid carrying with them both energy and charge. This mechanism is generally associated with studies of electrical conductivity. In the second mechanism, radiative reabsorption, the donor simply emits a real photon which is eventually absorbed by either another donor or an acceptor. This work deals with a third mechanism, radiationless energy transfer. In this process the transfer of energy between individual atoms or molecules can be viewed as a quantum mechanical resonance process involving the exchange of a virtual photon. This exchange occurs via either an electromagnetic multipolemultipole interaction or an exchange interaction.

The foundations of energy transfer theory were established by Föster[18],[19]. Föster electric

dipole-dipole interaction theory is still used today. This theory was extended by Dexter[20] to include higher order multipole interactions and exchange interaction. Work in this area has increased in the past thirty years because of the importance of energy transfer processes in the application of optical materials to technological systems.

- 1.4.2 The Föster-Dexter transfer (two-body interaction electric multipole transfer) rate[21]
 - a). The two-body interaction energy transfer Hamiltonian As shown in Figure 1.5.

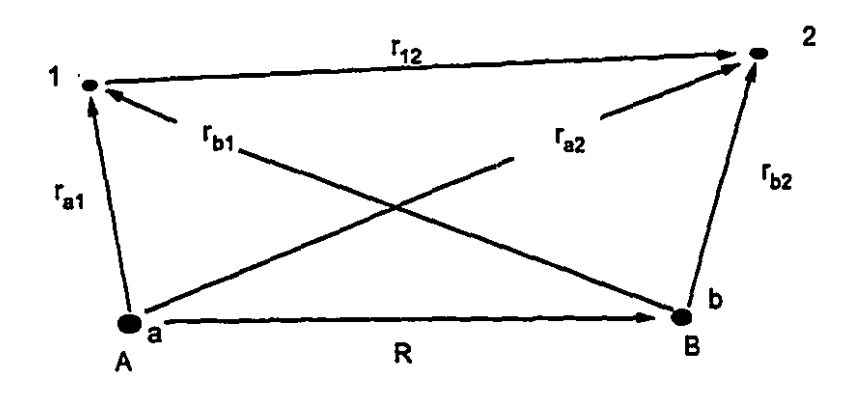


Figure 1.5 Two-atom system

 H_{A} and H_{B} are the Hamiltonian of atom A and B, respectively. The Hamiltonian of the two-atom system is given by:

$$H = H_A + H_B + H_{AB} \tag{1.7}$$

in the above equation

$$H_{AB} = \frac{Z_a Z_b e^2}{R} + \frac{e^2}{r_{12}} - \frac{Z_a e^2}{r_{a2}} - \frac{Z_b e^2}{r_{b1}}$$

$$= \frac{Z_a Z_b e^2}{R} + \frac{e^2}{r_{12}} - \frac{Z_a e^2}{|\vec{R} + \vec{r}_{b2}|} - \frac{Z_b e^2}{|-\vec{R} + \vec{r}_{a1}|}$$
(1.8)

Let $|a\rangle$ and $|a'\rangle$ to be the ground state and excited state wavefunctions of atom A, $|b\rangle$ and $|b'\rangle$ to be the ground state and excited wavefunctions of atom B, respectively. Consider a transition from an initial state $|1\rangle = |a'b\rangle$ to a final state $|2\rangle = |ab'\rangle$. The matrix element of this transition is given by:

$$\langle a'(1)b(2) | H_{AB} | a(1)b'(2) \rangle$$

$$= Z_{a} Z_{b} \frac{e^{2}}{R} \langle a'(1) | a(1) \rangle \langle b(2) | b'(2) \rangle$$

$$+ \langle a'(1)b(2) | \frac{e^{2}}{r_{12}} | a(1)b'(2) \rangle$$

$$- Z_{a} e^{2} \langle a'(1) | a(1) \rangle \langle b(2) | \frac{1}{|\vec{R} + \vec{r}_{b2}|} | b'(2) \rangle$$

$$- Z_{b} e^{2} \langle a'(1) | \frac{1}{|\vec{R} + \vec{r}_{a1}|} | a(1) \rangle \langle b(2) | b'(2) \rangle$$

$$= \langle a'(1)b(2) | \frac{e^{2}}{r_{12}} | a(1)b'(2) \rangle$$

$$= \langle a'(1)b(2) | \frac{e^{2}}{r_{12}} | a(1)b'(2) \rangle$$

Taking into account the overlap of the wavefunction the relevant product wavefunctions are replaced as follows:

$$|a'(1)b(2)\rangle \rightarrow \frac{1}{\sqrt{2}}|a'(1)b(2)-b(1)a'(2)\rangle$$

$$|a(1)b'(2)\rangle \rightarrow \frac{1}{\sqrt{2}}|a(1)b'(2)-b'(1)a(2)\rangle$$
(1.10)

Then

$$\langle a'(1)b(2) | H_{AB} | a(1)b'(2) \rangle$$

$$-\frac{1}{2} \langle a'(1)b(2) | H_{AB} | a(1)b'(2) \rangle$$

$$+\frac{1}{2} \langle b(1)a'(2) | H_{AB} | b'(1)a(2) \rangle$$

$$-\frac{1}{2} \langle b(1)a'(2) | H_{AB} | a(1)b'(2) \rangle$$

$$-\frac{1}{2} \langle a'(1)b(2) | H_{AB} | b'(1)a(2) \rangle$$

$$= \langle a'(1)b(2) | H_{AB} | a(1)b'(2) \rangle$$

$$-\langle a'(1)b(2) | H_{AB} | b'(1)a(2) \rangle$$

and

$$\langle a'(1)b(2) | H_{AB} | b'(1) a(2) \rangle$$

$$= Z_{a} Z_{b} \frac{e^{2}}{R} \langle a'(1) | b'(1) \rangle \langle b(2) | a(2) \rangle$$

$$+ \langle a'(1)b(2) | \frac{e^{2}}{r_{12}} | b'(1) a(2) \rangle$$

$$- Z_{a} e^{2} \langle a'(1) | b'(1) \rangle \langle b(2) | \frac{1}{|\vec{R} + \vec{r}_{b2}|} | a(2) \rangle$$

$$- Z_{b} e^{2} \langle b(2) | a(2) \rangle \langle a'(1) | \frac{1}{|-\vec{R} + \vec{r}_{a1}|} | b'(1) \rangle$$

$$= \langle a'(1)b(2) | \frac{e^{2}}{r_{12}} | b'(1) a(2) \rangle$$
(1.12)

Thus, the matrix element is given by:

$$\langle |H_{AB}| \rangle = \langle a'(1)b(2)| \frac{e^2}{I_{12}} |a(1)b'(2) \rangle$$

- $\langle a'(1)b(2)| \frac{e^2}{I_{12}} |b'(1)a(2) \rangle$ (1.13)

b). Interaction between two atoms in solidsConsider two atoms A and B in fixed positions in a solid as shown in Figure 1.6, and set

$$\vec{R} = (R, \theta, \phi)$$

$$R > r_{AS}, r_{Bt}$$

$$\vec{r}_{st} = \vec{R} + \vec{r}_{Bt} - \vec{r}_{AS}$$

$$(1.14)$$

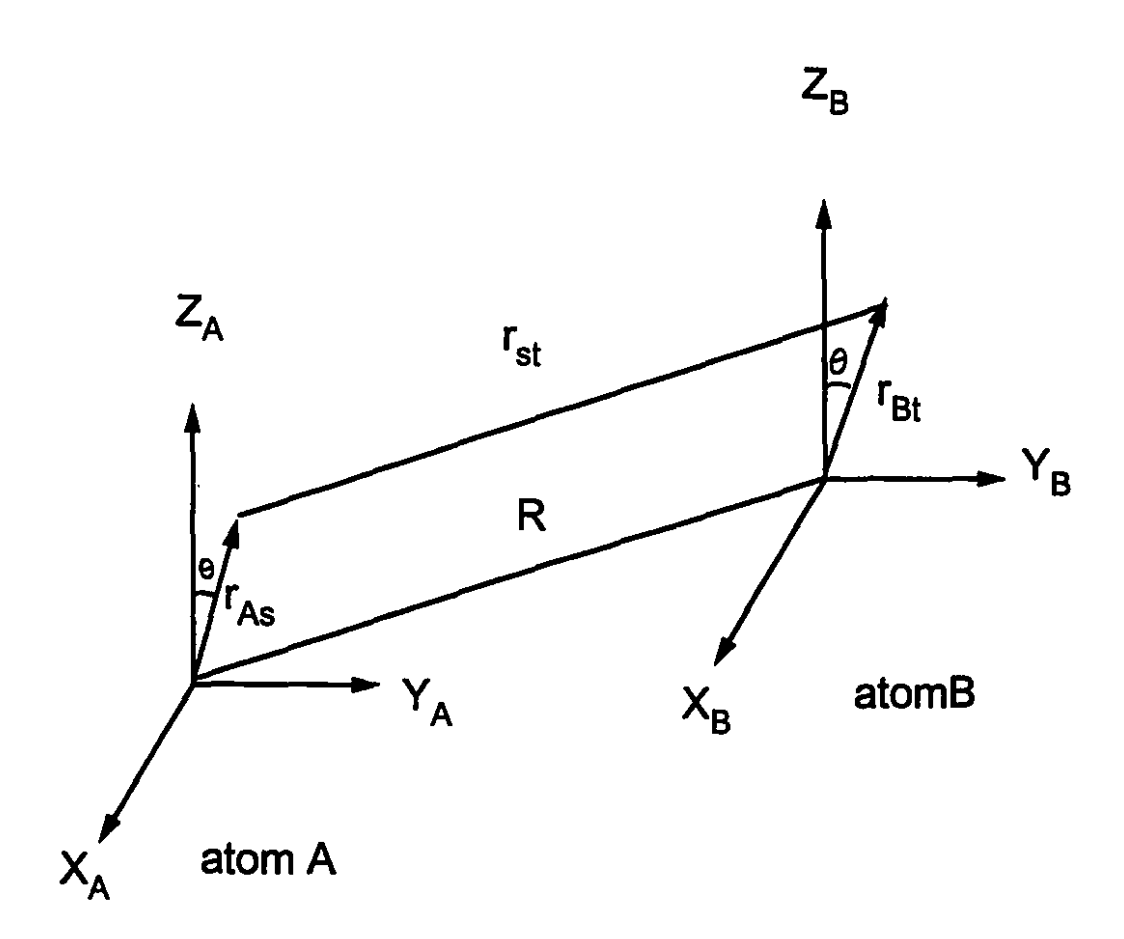


Figure 1.6 Two-atom system in solids

The relevant energy transfer Hamiltonian is given by:

$$H_{AB} = \sum_{s,t} \frac{e^2}{r_{st}} = \sum_{s,t} \frac{e^2}{|\vec{R} + \vec{r}_{Bt} - \vec{r}_{As}|}$$
(1.15)

where the sum is over the electrons of the two atoms. Taking into account the fact that $R>>r_{As}$, r_{Bt} , the expansion of H_{AB} in spherical harmonics is given by [22]:

$$H_{AB} = e^{2} \sum_{l_{1}=0}^{\infty} \sum_{l_{2}=0}^{\infty} \sum_{m_{1}=-l}^{l} \sum_{m_{2}=-l}^{l} \frac{1}{R^{l_{1}+l_{2}+1}}$$

$$\cdot G_{12} C_{m_{1}+m_{2}}^{l_{1}+l_{2}} (\theta, \phi) * D_{m_{1}}^{l_{1}} (A) D_{m_{2}}^{l_{2}} (B)$$

$$(1.16)$$

where

$$G_{12} = (-1)^{l_1} \sqrt{\frac{(2l_1 + 2l_2 + 1)!}{(2l_1)!(2l_2)!}} \begin{pmatrix} l_1 & l_2 & l_1 + l_2 \\ m_1 & m_2 & -m_1 - m_2 \end{pmatrix}$$
(1.17)

$$D_{m}^{1}(A) = \sum_{s} r_{s}^{1} C_{m}^{1}(\theta_{s}, \dot{\phi}_{s})$$
 (1.18)

$$C_m^1(\Omega) = \sqrt{\frac{4\pi}{2l+1}} Y_{lm}(\Omega)$$
 (1.19)

$$\begin{pmatrix}
j_1 & j_2 & j_3 \\
m_1 & m_2 & m_3
\end{pmatrix} = (-1)^{j_1 - j_2 - m_3} \sqrt{2j_3 + 1} \\
\langle j_1 m_1 j_2 m_2 | j_1 j_2 j_3 - m_3 \rangle$$
(1.20)

For example l=1, m=0, ± 1 :

严认

$$Y_{10} = \sqrt{\frac{3}{4\pi}} \cos\theta = \sqrt{\frac{3}{4\pi}} \frac{z}{r}$$

$$Y_{1,\pm 1} = \mp \sqrt{\frac{3}{8\pi}} e^{\pm i\phi} \sin\theta = \mp \sqrt{\frac{3}{8\pi}} \frac{x \pm iy}{r}$$
(1.21)

Then

$$C_{o}^{1} = \sqrt{\frac{4\pi}{3}} Y_{10} = \frac{z}{r}$$

$$C_{\pm 1}^{1} = \sqrt{\frac{4\pi}{3}} Y_{\pm 1} = \mp \frac{1}{\sqrt{2}} \frac{x \pm y}{r}$$
(1.22)

and

$$D_0^1 = rC_0^1 = z$$

$$D_1^1 = rC_1^1 = -\frac{1}{\sqrt{2}} (x + iy)$$

$$D_{-1}^1 = rC_{-1}^1 = \frac{1}{\sqrt{2}} (x - iy)$$
(1.23)

Then the direct term of $<|H_{AB}|>$ is

$$\langle a'b|H_{AB}|ab'\rangle = \sum_{l_1 l_2 m_1 m_2} \frac{e^2}{R^{l_1 + l_2 + 1}} G_{12} C_{m_1 + m_2}^{l_1 + l_2^2}$$

$$\langle a'|D_{m_1}^{l_1}|a\rangle\langle b|D_{m_2}^{l_2}|b'\rangle$$
(1.24)

The quantity related to the transition rate is

$$\begin{aligned} |\langle a'b|H_{AB}|ab'\rangle|^{2} &= \sum_{l_{1}l_{2}m_{1}m_{2}} \sum_{l_{3}l_{4}m_{3}m_{4}} \frac{e^{4}}{R^{l_{1}+l_{2}+l_{3}+l_{4}+2}} G_{12}G_{34} \\ & \cdot C_{m_{1}+m_{2}}^{l_{1}+l_{2}^{*}} C_{m_{3}+m_{4}}^{l_{3}+l_{4}} \\ & \cdot \langle a'|D_{m_{1}}^{l_{1}}|a\rangle\langle a'|D_{m_{3}}^{l_{3}}|a\rangle^{*} \\ & \cdot \langle b|D_{m_{2}}^{l_{2}}|b'\rangle\langle b|D_{m_{4}}^{l_{4}}|b'\rangle^{*} \end{aligned}$$

$$(1.25)$$

Averaging over θ and Φ the following result is obtained:

$$\frac{\frac{1}{4\pi} \iint \sin\theta d\theta d\phi C_{m_1+m_2}^{l_1+l_2} C_{m_3+m_4}^{l_3+l_4}}{\frac{1}{\sqrt{(2l_1+2l_2+1)(2l_3+2l_4+1)}}}$$

$$\frac{1}{\delta_{l_1+l_2, l_3+l_4} \delta_{m_1+m_2, m_3+m_4}}$$
(1.26)

Neglecting cross terms: $l_1 \neq l_3$, $l_2 \neq l_4$, $m_1 \neq m_3$, $m_2 \neq m_4$, $|<|H_{AB}|>|^2$ can be expressed as:

$$|\langle |H_{AB}| \rangle|^{2} \propto \sum_{l_{1}l_{2}m_{1}m_{2}} \left[\frac{e^{2}}{R^{l_{1}+l_{2}+1}} \right]^{2} G_{12}^{2} \frac{1}{2l_{1}+2l_{2}+1}$$

$$\cdot |\langle a'|D_{m_{1}}^{l_{1}}|a \rangle|^{2} |\langle b|D_{m_{2}}^{l_{2}}|b' \rangle|^{2}$$
(1.27)

where

$$G_{12}^{2} = \frac{(2I_{1}+2I_{2}+1)!}{(2I_{1})!(2I_{2})!} \begin{pmatrix} I_{1} & I_{2} & I_{1}+I_{2} \\ m_{1} & m_{2} & -m_{1}-m_{2} \end{pmatrix}^{2}$$
(1.28)

Taking the average of G_{12}^2 :

$$\langle G_{12}^{2} \rangle = \frac{1}{(2l_{1}+1)(2l_{2}+1)} \sum_{m_{1},m_{2}} G_{12}^{2}$$

$$= \frac{1}{(2l_{1}+1)(2l_{2}+1)} \sum_{m_{1},m_{2}} \frac{(2l_{1}+2l_{2}+1)!}{(2l_{1})!(2l_{2})!}$$

$$\begin{cases} l_{1} l_{2} l_{1}+l_{2} \\ m_{1} m_{2} -m_{1}-m_{2} \end{cases}^{2}$$

$$= \frac{(2l_{1}+2l_{2}+1)!}{(2l_{1}+1)!(2l_{2}+1)!} \sum_{m_{1},m_{2}} \begin{pmatrix} l_{1} l_{2} l_{1}+l_{2} \\ m_{1} m_{2} -m_{1}-m_{2} \end{pmatrix}^{2}$$

$$= \frac{(2l_{1}+2l_{2}+1)!}{(2l_{1}+1)!(2l_{2}+1)!}$$

$$= \frac{(2l_{1}+2l_{2}+1)!}{(2l_{1}+1)!(2l_{2}+1)!}$$

$$(1.29)$$

 $|<|H_{AB}|>|^2$ can be expressed as:

$$\begin{aligned} |\langle |H_{AB}| \rangle|^{2} &= \sum_{\substack{l_{1}l_{2}m_{1}m_{2} \\ (2l_{1}+2l_{2}+1)! \\ (2l_{1}+1)!(2l_{2}+1)!}} \frac{1}{2l_{1}+2l_{2}+1} \\ &\cdot \frac{(2l_{1}+2l_{2}+1)!}{(2l_{1}+1)!(2l_{2}+1)!} \frac{1}{2l_{1}+2l_{2}+1} \\ &\cdot |\langle a'|D_{m_{1}}^{l_{1}}|a\rangle|^{2}|\langle b|D_{m_{2}}^{l_{2}}|b\rangle|^{2} \\ &= \sum_{\substack{l_{1}l_{2} \\ R^{l_{1}+l_{2}+1}}} (\frac{e^{2}}{R^{l_{1}+l_{2}+1}})^{2} \frac{(2l_{1}+2l_{2})!}{(2l_{1}+1)!(2l_{2}+1)!} \\ &\cdot [\sum_{m_{1}} |\langle a'|D_{m_{1}}^{l_{1}}|a\rangle|^{2}] [\sum_{m_{2}} |\langle b|D_{m_{2}}^{l_{2}}|b\rangle|^{2}] \end{aligned}$$

$$(1.30)$$

c). The energy transfer rate

The transfer rate is defined as [21]

$$\gamma_{AB} = \frac{4\pi^2}{h} \left| \langle |H_{AB}| \rangle |^2 S$$
 (1.31)

where

$$S = \int g_{A}(E) g_{B}(E) dE = \frac{2\pi}{h} \int g_{A}(\omega) g_{B}(\omega) d\omega \qquad (1.32)$$

is the overlap integral. In (1.32) $g_A(\omega)$ and $g_B(\omega)$ are the line shape functions for ions A and B respectively. Considering the case of two Lorentzian lines of width $\Delta\omega_A$ and $\Delta\omega_B$, centred at ω_A and ω_B , respectively, the overlap integral is given by[21]:

$$\int g_{A}(\omega) g_{B}(\omega) d\omega = \frac{1}{\pi} \frac{\Delta \omega}{(\Delta \omega)^{2} + (\omega_{A} - \omega_{B})^{2}}$$

$$= \frac{1}{2\pi^{2} c} \frac{\Delta v}{\Delta v^{2} + (v_{A} - v_{B})^{2}}$$
(1.33)

where $\Delta V = \Delta V_A + \Delta V_B$ is the line width with a unit cm⁻¹.

Under normal conditions the exchange interaction is negligible compared with the direct interaction, the magnetic multipole interactions are negligible compared with the electric multipole interactions of the same order, and the dipole-quadrupole interaction are negligible compared with the dipole-dipole interaction, so we only consider the electric dipole-dipole interaction.

An electric multipole of a charge distribution $\rho(x)$ with $x\equiv(r,\theta,\Phi)$ is defined as follows:

$$D_{l,m} = \sqrt{\frac{4\pi}{2l+1}} \int d\tau \rho (\vec{x}) r^{l} Y_{lm}(\theta, \phi)$$
 (1.34)

If set

$$\rho(\vec{x}) = \sum_{s} e\delta(\vec{x} - \vec{x}_{s}) \qquad (1.35)$$

Thus

$$D_{l,m} = \sqrt{\frac{4\pi}{2l+1}} \int d\tau \sum_{s} e\delta (\vec{x} - \vec{x}_{s}) r^{l} Y_{lm}(\theta, \phi)$$

$$= e \sum_{s} \sqrt{\frac{4\pi}{2l+1}} r_{s}^{l} Y_{lm}(\theta_{s}, \phi_{s})$$
(1.36)

These quantities $(D_{1,m}/e)$ are the same as the quantities $D_m^{\ 1}$ defined in Equation (1.18).

The electric multipole energy transfer rate can be written as:

$$\gamma_{AB} = \frac{4\pi^2}{h} \left| \langle |H_{AB}| \rangle |^2 S = \frac{C^{(6)}}{R^6} + \frac{C^{(8)}}{R^8} + \frac{C^{(10)}}{R^{10}} + \dots \right| (1.37)$$

where

$$\frac{C^{(6)}}{R^6} = \frac{4\pi^2}{h} \frac{e^4}{R^6} \frac{4!}{3!3!} \left[\sum_{m=-1}^{1} |\langle a'|D_m^1|a\rangle|^2 \right]
\cdot \left[\sum_{m=-1}^{1} |\langle b|D_m^1|b'\rangle|^2 \right] S$$
(1.38)

is the dipole-dipole term,

$$\frac{C^{(8)}}{R^8} = \frac{4\pi^2}{h} \frac{e^4}{R^8} \frac{6!}{3!3!} \left(\left[\sum_{m=-1}^{1} |\langle a'|D_m^1|a\rangle|^2 \right] \left[\sum_{m=-2}^{2} |\langle b|D_m^2|b\rangle|^2 \right] + \left[\sum_{m=-2}^{2} |\langle a'|D_m^2|a\rangle|^2 \right] \left[\sum_{m=-1}^{1} |\langle b|D_m^1|b\rangle|^2 \right] \right) S$$
(1.39)

is the dipole-quadrupole term, and

$$\frac{C^{(10)}}{R^{10}} = \frac{4\pi^2}{h} \frac{e^4}{R^{10}} \frac{8!}{5!5!}
\cdot \left[\sum_{m=-2}^{2} |\langle a'|D_m^2|a\rangle|^2 \right] \left[\sum_{m=-2}^{2} |\langle b|D_m^2|b'\rangle|^2 \right] S$$
(1.40)

is the quadrupole-quadrupole term.

Considering only the electric dipole-dipole interaction the energy transfer rate is given by [21]:

$$\gamma_{AB} = \frac{C^{(6)}}{R^6} = \frac{1}{\tau_A} \left(\frac{R_0}{R} \right)^6 \tag{1.41}$$

where τ_{A} is the radiative lifetime of atom A, R₀ is the radius at which the energy transfer rate is equal to the decay rate.

1.4.3 The Judd[11]-Ofelt[12] parameter expression of the two-body transfer rate

The Judd-Ofeld parameter expressions of the two-body electric dipole-dipole and dipole-quadrupole transfer rates in rare-earth ion doped crystals were developed by Kushida[23]. The results are the following:

$$\begin{split} & \overline{\gamma}_{AB}^{dd} = \frac{1}{(2J_a+1)(2J_b+1)} \left(\frac{2}{3}\right) \left(\frac{4\pi^2}{h}\right) \left(\frac{\theta^2}{R^3}\right)^2 \\ & \cdot \left[\sum_{\lambda} \Omega_{A\lambda} \langle J_a || U^{(\lambda)} || J_a^{\prime} \rangle^2\right] \left[\sum_{\lambda} \Omega_{B\lambda} \langle J_b || U^{(\lambda)} || J_b^{\prime} \rangle^2\right] S \\ & = \frac{C_{AB}^{dd}}{R^6} \end{split}$$
(1.42)

$$\frac{\overline{\gamma}_{AB}^{dq}}{\overline{\gamma}_{AB}^{dq}} = \frac{1}{(2J_{a}+1)(2J_{b}+1)} \left(\frac{4\pi^{2}}{h}\right) \left(\frac{e^{2}}{R^{4}}\right)^{2} \\
\cdot \left[\sum_{\lambda=2,4,6} \Omega_{A\lambda} \langle J_{a} | U^{(\lambda)} | | J_{a}^{\lambda} \rangle^{2} \right] \langle 4f | x_{B}^{2} | 4f \rangle^{2} \\
\langle f | C^{(2)} | f \rangle^{2} \langle J_{b} | U^{(2)} | J_{b}^{\lambda} \rangle^{2} S \\
= \frac{C_{AB}^{dq}}{R^{8}}$$
(1.43)

The above equations can be used to calculate the energy transfer rates if the Judd-Ofelt parameters Ω_{λ} and $\langle J | U^{(\lambda)} | J' \rangle^2$ (λ =2, 4, 6) are available and the donor-acceptor distance R is given.

1.5 Upconversion

1.5.1 Brief introduction

Upconversion is a phenomenon in which the wavelength of emitted light is shorter than that of the pumping light. The first upconversion lasers, demonstrated more than 20 years were flash-lamp-pumped, pulsed lasers limited to ago, operation at cryogenic temperatures [24]. In the past ten years, upconversion lasing has been observed in a number of materials doped with trivalent rare-earth ions, notably praseodymium[25],[26],neodymium[27],[28],holmium[29], erbium[30],[31],[32],[33],[34],[35],[36],and thulium[29],[37],[38],[39]. Upconversion is caused by multiple excitations (direct pump or energy transfer or both). For instance an exited ion absorbs a photon and reaches a higher excited level, when it later returns to the ground state the emitted photon has a higher energy than the absorbed

photon.

The central role of energy transfer in the dynamics of energy upconversion by rare earth ions was recognized in 1966[40],[41]. Nearly all theoretical treatments date have assumed a random distribution of donors and acceptors among the lattice points of the For distribution. crystal[21],[42],[43]. a random two-body process is characterized by an $n_{D}n_{A}$ dependence in the rate equations and a concentration independent transfer parameter[21].

1.5.2 Basic rate equation model to describe upconversion dynamics

The basic rate equation model used to describe the upconversion dynamics is based on two-body interaction electric dipole-dipole energy transfer and random distribution of the donors and acceptors. This model is called Static transfer model [21].

a). Static transfer model for a pulsed excitation case In a crystal which consists of $N_D(t)$ donors and $N_A(t)$ acceptors distributed among the lattice points, the basic rate equation for the donors take the form[44],[45], [46]:

$$\frac{d\rho_{i}^{D}(t)}{dt} = -\frac{1}{\tau_{D}}\rho_{i}^{D}(t) - \sum_{j=1}^{N_{T}} \gamma_{DA}(|R_{i}-R_{j}|) \rho_{i}^{D}(t) \rho_{j}^{A}(t) + \cdots
= -\frac{1}{\tau_{D}}\rho_{i}^{D}(t) - \sum_{j=1}^{N_{T}} \frac{C}{R_{ij}^{6}}\rho_{i}^{D}(t) \rho_{j}^{A}(t) + \cdots$$
(1.44)

where $1/\tau_D$ is the decay rate of the donor, ${\rho_1}^D(t)$ is the probability that the ith lattice point is occupied by a donor at time t, and ${\rho_1}^A(t)$ is the probability that the jth lattice point is occupied by an acceptor at time t. N_T is the total number of lattice points. Considering the average density of the probability, we should sum all the lattice points and divide by the total interaction volume V_T both sides of equation (1.44). Thus we obtain the following expression of the rate equation:

$$\frac{dn_D(t)}{dt} = -\frac{1}{\tau_D} n_D(t) - \frac{1}{V_T} \sum_{i=1}^{N_T} \sum_{j=1}^{N_T} \frac{C}{R_{ij}^6} \rho_i^D(t) \rho_j^A(t) + \dots$$
 (1.45)

In the above equation

$$n_D(t) = \frac{1}{V_T} \sum_{i=1}^{N_T} \rho_i^D(t) = \frac{N_D(t)}{V_T}$$
 (1.46)

is the concentration of the donors. From the same considerations we get the rate equation for the acceptors

$$\frac{dn_{A}(t)}{dt} = -\frac{1}{\tau_{A}}n_{A}(t) - \frac{1}{V_{T}}\sum_{i=1}^{N_{T}}\sum_{j=1}^{N_{T}}\frac{C}{R_{ij}}\rho_{i}^{D}(t)\rho_{j}^{A}(t) + \dots$$
 (1.47)

and for any state M at which the donor or acceptor stays after the energy transfer process

$$\frac{dn_{M}(t)}{dt} = -\frac{1}{\tau_{M}}n_{M}(t) + \frac{1}{V_{T}}\sum_{i=1}^{N_{T}}\sum_{j=1}^{N_{T}}\frac{C}{R_{ij}^{6}}\rho_{i}^{D}(t)\rho_{j}^{A}(t) + \dots \qquad (1.48)$$

The general rate equations take the form:

$$\frac{dn_{x}(t)}{dt} = -\frac{1}{\tau_{x}}n_{x}(t) \pm \frac{1}{V_{T}} \sum_{i=1}^{N_{T}} \sum_{j=1}^{N_{T}} \frac{C}{R_{ij}^{6}} \rho_{i}^{D}(t) \rho_{j}^{A}(t) + \dots$$
 (1.49)

In the above equation if $n_x(t)$ is the M state ion concentration the sign preceding the energy transfer term is positive, if $n_x(t)$ is either the donor or the acceptor concentration the sign in front of the energy transfer term is negative.

If the donors and acceptors are randomly distributed among the lattice points the possibility of finding a donor at any lattice point is the same as $\rho_i^{\ p}(t) = N_p(t)/N_T$ where $N_p(t)$ is the number of donors and N_T is the total number of lattice points, and the possibility of finding an acceptor at any lattice point is also the same as $\rho_i^{\ h}(t) = N_A(t)/N_T$ where $N_A(t)$ is the number of acceptors. The energy transfer term of equation (1.49) takes the form:

$$\frac{1}{V_{T}} \sum_{i=1}^{N_{T}} \sum_{j=1}^{N_{T}} \frac{C}{R_{ij}^{6}} \frac{N_{D}(t)}{N_{T}} \frac{N_{A}(t)}{N_{T}}$$

$$= \frac{N_{T}}{V_{T}} \sum_{j=1}^{N_{T}} \frac{C}{R_{ij}^{6}} \frac{N_{D}(t)}{N_{T}} \frac{N_{A}(t)}{N_{T}}$$

$$= \frac{N_{T}}{V_{T}} \sum_{a}^{\infty} \frac{C}{R^{6}} \frac{N_{T}}{V_{T}} 4\pi R^{2} dR \cdot \frac{N_{D}(t)}{N_{T}} \frac{N_{A}(t)}{N_{T}}$$

$$= \int_{a}^{\infty} \frac{4\pi C}{R^{4}} dR n_{D}(t) n_{A}(t)$$

$$= (\frac{4\pi C}{3a^{3}}) n_{D}(t) n_{A}(t)$$

$$= Wn_{D}(t) n_{A}(t)$$

$$= Wn_{D}(t) n_{A}(t)$$

where W is the transfer parameter which can be expressed as:

$$W = \frac{CV_T}{N_T^2} N_T \sum_{i=1}^{N_T} \frac{1}{R_{1j}^6} = \frac{CV_T}{N_T^2} N_T \frac{N_T}{V_T} \iiint \frac{1}{R^6} dV$$

$$= 4\pi C \int_a \frac{1}{R^6} dV \approx 4\pi C \int_a \frac{1}{R^6} dR = \frac{4\pi}{3} \frac{C}{a^3} = \frac{\overline{\gamma}^{dd} (R=a)}{n_T}$$
(1.51)

where a is the lattice distance and n_T is the concentration of lattice points (in the crystals of Er^{3+} :YAG, Er^{3+} :YAlO₃, Tm^{3+} :YLiF₄ and Tm^{3+} :Y₂BaF₈ they are the concentrations of Yttrium ions in YAG, YAlO₃, YLiF₄ and Y₂BaF₈ that are given in Table 1.2). Clearly this approach yields a W that is an activator concentration independent constant.

b). Static transfer model for continuous pumping case In this case we need to add a pump term in (1.49). Thus the rate equations take the form:

$$\frac{dn_{x}(t)}{dt} = P_{yx}(n_{y}(t) - n_{x}(t)) - \frac{1}{\tau_{x}}n_{x}(t) \pm wn_{D}(t)n_{A}(t) + \dots$$
(1.52)

where $P_{yx}=\sigma I$ is the pump rate. I is the pump intensity and σ is the absorption cross-section which is given by[3]:

$$\sigma = A_{xy} \frac{c^2}{8\pi f_{yx}^2 n^2} g(v)$$
 (1.53)

where A_{xy} is the radiative decay rate from level x to level y, c is the velocity of light in vacuum, f_{yx} is frequency of the pump light, n is the refractive index of the medium, and g(v) is the line shape form factor. For a resonant pump and a Gaussian luminescence line of width Δv_{lum} , the line shape form factor take the form[3]:

$$g(\mathbf{v}) = \frac{1}{C\Delta \mathbf{v}_{1um}} \tag{1.54}$$

thus the absorption cross-section is given by[3]:

$$\sigma = A_{ji} \frac{C^2}{8\pi v_{ij}^2 n^2 c \Delta v_{lum}}$$

$$= A_{ji} \frac{\lambda_{ij}^2}{8\pi n^2 c \Delta v_{lum}}$$
(1.55)

1.5.3 Avalanche upconversion

a). The phenomenon of photon avalanche

The phenomenon of photon avalanche was first discovered in Pr^{3+} based infrared quantum counters[47]. A LaCl₃ or LaBr₃ crystal doped with Pr^{3+} was exposed to laser-pump radiation, in which the frequency matches the excited-state transition absorption $^3H_5 \rightarrow ^3P_1$. When this radiation was slightly in excess of a certain critical intensity, Pr^{3+}

orders of magnitude fluorescence increased by correspondingly, pump absorption was sufficient to cause a dimming of the laser light on passing through the crystal. This phenomenon was ascribed to an efficient cross-relaxation energy transfer between the lowest infrared levels of Pr3+ which induces the excited state absorption used in the quantum counter process. Such an avalanche process was also observed other rare-earth-doped crystals with such as Sm^{3+} : LaBr₃[48], Nd³⁺: LiYF₄[49], Pr³⁺: LaCl₃[25], $Tm^{3+}:LiYF_4[50]$, and $Tm^{3+}:YAlO_3[51]$. Experimentally, signature of avalanche upconversion has been the threshold behaviour of the upconversion emission, and a concomitant threshold for excited state absorption.

b). The avalanche upconversion model

÷-----

The fundamental avalanche upconversion model (the three level model[52]) relies on an excited state absorption, resonant with the pump wavelength, from a level which is populated by one cross-relaxation step.

The following gives an introduction of this basic theory[52] which gives the necessary and sufficient condition to observe an avalanche.

Figure 1.7 shows the general energy scheme for an avalanche process. The nonresonant absorption from the ground state populates level 2', which relaxes nonradiatively to the metastable level 2: The resonant absorption 2-3', followed by the nonradiative relaxation 3'-3, leads to the population of

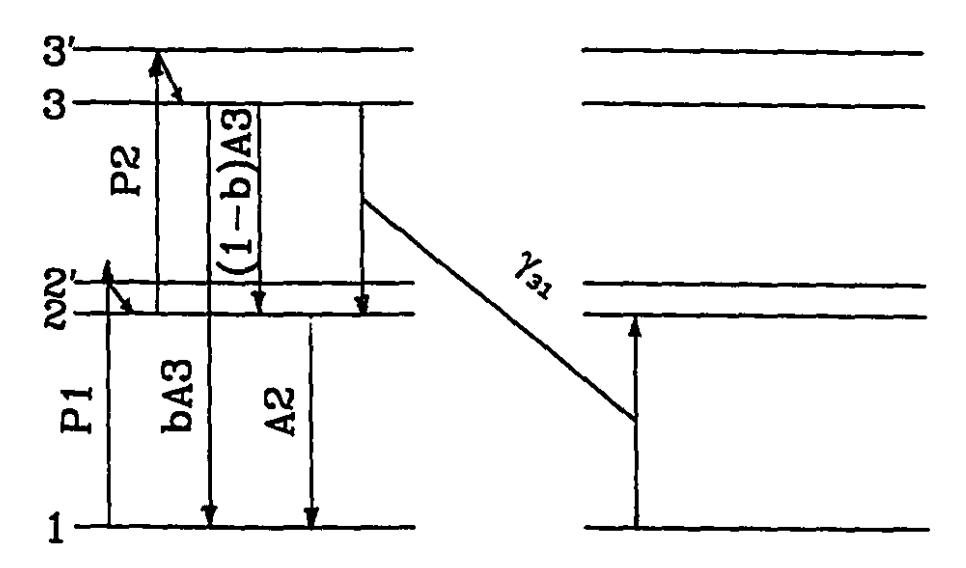


Figure 1.7

Three level schem for an avalanche process

the emission level 3. Then the cross-relaxation process permits a very efficient population of level 2 and enhances the excited-state absorption $2\rightarrow3'$. Since the phonon relaxation are fast compared to all other processes involved, the excitation process can be adequately described by the following rate equations (where ρ_1 , ρ_2 , and ρ_3 are the normalized population in level 1, 2, and 3, respectively):

$$\frac{d\rho_{1}}{dt} = -P_{1}\rho_{1} + A_{2}\rho_{2} + bA_{3}\rho_{3} - \gamma_{31}\rho_{3}\rho_{1}$$

$$\frac{d\rho_{2}}{dt} = P_{1}\rho_{1} - (A_{2} + P_{2})\rho_{2} + (1 - b)A_{3}\rho_{3} + 2\gamma_{31}\rho_{1}\rho_{3}$$

$$\frac{d\rho_{3}}{dt} = P_{2}\rho_{2} - A_{3}\rho_{3} - \gamma_{31}\rho_{1}\rho_{3}$$
(1.56)

with

$$\rho_1 + \rho_2 + \rho_3 = 1$$
.

The nonresonant absorption from the ground-state and the

resonant excited-state absorption are characterized by pumping rates P_1 and P_2 , respectively. A_2 and A_3 are the radiative relaxation rates of levels 2 and 3, respectively. The branching in the decay of level 3 is described by the parameter b with $(1-b)A_3$ being the decay rate to level 2. The energy-transfer process is described by the rate γ_{31} .

1). Stationary solutions

The system of equation (1.56) was solved explicitly in the long-time limit[52]. When t $\rightarrow \infty$, the following equations were obtained:

$$\frac{d\rho_1}{dt} = \frac{d\rho_2}{dt} = \frac{d\rho_3}{dt} = 0 \tag{1.57}$$

and the stationary solution for level 3 population is

$$\rho_3^{\infty} = \frac{B}{2C} \left[-1 + sgn(B) \left(1 + \frac{4CP_1}{B^2} \right)^{1/2} \right]$$
 (1.58)

with

$$C = \frac{\gamma_{31}}{P_2} \left[P_2 + A_3 (1+b) - A_2 \right] \tag{1.59}$$

and

$$B = \frac{1}{P_2} \left[A_2 (A_3 + \gamma_{31}) - P_2 (\gamma_{31} - bA_3) + P_1 A_3 + P_1 P_2 \right]$$
 (1.60)

In equation (1.58)

$$sgn(B)=+1 if B>0$$

$$sgn(B) = -1 if B < 0$$

Since P_1 corresponds to a nonresonant absorption, P_1 is very small compared to all the other terms. So

$$(1 + \frac{4CP_1}{B^2})^{1/2} \approx 1 + \frac{2CP_1}{B^2}$$
 (1.61)

This leads to the following solution for ρ_3^- : if B>0,

$$\rho_{3}^{\bullet} \approx \frac{B}{2C} \left[-1 + \left(1 + \frac{2CP_{1}}{B^{2}} \right) \right] \\
= \frac{P_{1}}{B} \\
= \frac{P_{1}P_{2}}{A_{2} \left(A_{3} + \gamma_{31} - P_{2} \left(\gamma_{31} - bA_{3} \right) + P_{1}P_{2} + P_{1}A_{3}} \\
= \frac{P_{1}P_{2}}{\gamma_{31} - bA_{3}} \frac{1}{A_{2} \left(A_{3} + \gamma_{31} \right) - P_{2} + \frac{P_{1} \left(P_{2} + A_{3} \right)}{\gamma_{31} - bA_{3}} \\
\approx \frac{P_{1}P_{2}}{\gamma_{31} - bA_{3}} \frac{1}{A_{2} \left(A_{3} + \gamma_{31} \right) - P_{2}} \\
= \frac{P_{1}P_{2}}{\gamma_{31} - bA_{3}} \frac{1}{P_{21imic} - P_{2}}$$
(1.62)

if B<0,

$$\rho_{3}^{\infty} \approx \frac{B}{2C} \left[-1 - \left(1 + \frac{2CP_{1}}{B^{2}} \right) \right]
\approx -\frac{B}{C}
= \frac{-A_{2} (A_{3} + \gamma_{31}) + P_{2} (\gamma_{31} - bA_{3}) - P_{1}P_{2} - P_{1}A_{3}}{\gamma_{31} \left[A_{3} (1 + b) + P_{2} - A_{2} \right]}
\approx (\gamma_{31} - bA_{3}) \frac{P_{2} - \frac{A_{2} (A_{3} + \gamma_{31})}{\gamma_{31} \left[A_{3} (1 + b) + P_{2} - A_{2} \right]}
\approx (\gamma_{31} - bA_{3}) \frac{P_{2} - P_{2,1,imit}}{\gamma_{31} \left[A_{32} (1 + b) + P_{2} - A_{32} \right]}$$
(1.63)

In the above equations

$$P_{21imic} = \frac{A_2 (\gamma_{31} + A_3)}{\gamma_{31} - bA_3} \tag{1.64}$$

is the threshold.

2). Discussion

If γ_{31}
bA₃, from equation (1.60) we get B>0, regardless of the excitation power there exists only one solution for ρ_3 .

$$\rho_3^{-} = \frac{P_1 P_2}{\gamma_{31} - b A_{32}} \cdot \frac{1}{P_{211min} - P_2}$$
 (1.65)

If $\gamma_{31} > bA_3$, there are two solution of ρ_3 :

i) if B>0 namely P2<P2limit

$$\rho_3^{\bullet} = \frac{P_1 P_2}{\gamma_{31} - bA_{32}} \cdot \frac{1}{P_{2,1 \min E} - P_2}$$
 (1.66)

ii) if B<O namely P2>P21imit

$$n_3 = (\gamma_{31} - hA_{32}) \cdot \frac{P_2 - P_{21imic}}{\gamma_{31} [A_{32} (1+b) + P_2 - A_{21}]}$$
(1.67)

Above the threshold, there is the avalanche effect. In conclusion, the avalanche effect may occur only if the cross-relaxation rate γ_{31} is bigger than the decay rate from level 3 to level 1 (bA₃).

1.6 High (higher than two) order concentration dependent energy transfer and concentration dependent transfer parameter

- 1.6.1 Observations
- a). High order concentration dependent energy transfer
 A very thorough discussion of the concentration dependent
 energy transfer is given by Grant[53]. He points out that
 it is a curious fact that the concentration dependence of the

energy transfer follows a square law in the vast majority of cases and powers up to three are not uncommon. The observation of nonlinear concentration dependence at low concentrations gives strong experimental evidence for the high order concentration dependent energy transfer process. As an example[54], the self-quenching of Eu3+ emission transition from the 5Do level can not be accounted for in terms of pairwise multipolar interaction in view of the fact that the energy separation between the 5D0 level and the 7F6 level is about 12000 cm-1 and the energy separation between the 7F6 level and ground ⁷F₀ level is only about 5000 cm⁻¹. In the process to populate the 5D_0 level two donors $(^7F_6 \rightarrow ^7F_0)$ and one acceptor $(^{7}F_{6} \rightarrow {}^{5}D_{0})$ must be involved. Another example[55] is the transfer between the $\mathrm{Tb}^{3+}\ ^5D_4$ level and the $\mathrm{Eu}^{3+}\ ^5D_1$ level which has a difference in energy by about 2000 cm-1 and can not be accounted for in terms of pairwise multipolar interaction.

b). Concentration dependent transfer parameter

In 1985 V. I. Zhekov et al[56] measured the energy transfer parameters W_{DA} of the energy transfer process $^6I_{13/2} \rightarrow$ $^6I_{15/2}$, $^6I_{13/2} \rightarrow$ $^6I_{9/2}$ in $Er^{3+}:Y_3Al_5O_{12}$ with different Er^{3+} concentrations (0.5-100%). They found that the energy transfer parameter is a function of the Er^{3+} concentration - proportional to the second power of the Er^{3+} concentration. This observation was reconfirmed in $Er^{3+}:Y_3Al_5O_{12}[57]$, [58], [59]. In references [58] and [59] it was also reported that there are deviations of this second power

concentration dependence of the transfer parameters at low (lower than 3%) and high (higher than 60%) Er³+ concentrations (there are three experimental points in this part as shown in fig.5 of ref.[58]). The details of these deviations are that when the Er³+ concentration is lower than 3% the transfer parameter is linearly dependent on the Er³+ concentration, and when the Er³+ concentration is higher than 60% the transfer parameter dependence is lower than the second power of the Er³+ concentration. These deviations, as reported in references [58] and [59], are difficult to explain with the current energy transfer theories.

1.6.2 The diffusion transfer model[42]

In this model the donors are treated like gas molecules that can move randomly within the crystal. The acceptors are treated like an array of static black holes. As soon as a donor gets close enough to an acceptor, it will transfer energy to the acceptor. The relevant equation that describes such a diffusion process is:

$$\frac{\partial}{\partial t} n_D(\mathbf{R}, t) = \left[D \nabla^2 - \frac{1}{\tau} - \sum_{j=1}^{N_A} \gamma_{DA} (|\mathbf{R} - \mathbf{R}_j|) \right] n_D(\mathbf{R}, t) \tag{1.68}$$

where the first term in the square brackets deals with diffusion among donors, the second with the self-decay of donors, and the third with donor-acceptor energy transfer. In the present case the analog of the average donor concentration is the function:

$$n_D(t) = \frac{1}{V} \int n_D(\mathbf{R}, t) d^3\mathbf{R}$$
 (1.69)

Yokota and Tanimoto[42] have obtained an expression for $n_{\rm p}(t)$ in the case of dipole-dipole interaction when

$$\gamma_{DA} = \frac{C_{DA}}{R^6} = \frac{1}{\tau} \left(\frac{R_0}{R} \right)^6 \tag{1.70}$$

This expression was reported

$$n_{D}(t) = n_{D}(0) \exp\left[-\frac{t}{\tau} - \frac{n_{A}}{c_{0}} \Gamma\left(\frac{1}{2}\right) \left(\frac{t}{\tau}\right)^{1/2} \cdot \left(\frac{1+10.87x+15.5x^{2}}{1+8.743x}\right)^{3/4}\right]$$
(1.71)

where $c_0=(4\pi R_0^3/3)^{-1}$, $x=Dc_{DA}^{-1}t^{2/3}$ where c_{DA} , as given in (1.70), is the microparameter of the dipole-dipole transfer between a donor and an acceptor , and n_A is the concentration of the acceptors. In the case for $t\to\infty$, namely $x\to\infty$

$$n_D(t) - n_D(0) \exp(-\frac{t}{\tau} - K_D t)$$
 (1.72)

where $K_D=3.64\pi D^{3/4}c_{DA}^{1/4}n_A$, the diffusion constant D=3.375 $n_{0D}c_{DD}^{3/4}$ where c_{DD} is the microparameter of the dipole-dipole transfer between two donors, and n_{0D} is the concentration of unexcited donors. Equation (1.72) leads to the following rate equation for the donors:

$$\frac{d}{dt}n_D(t) = -\frac{1}{\tau}n_D(t) - 9\pi c_{DD}^{3/4}c_{DA}^{1/4}n_{0D}(t)n_D(t)n_A(t)
= -\frac{1}{\tau}n_D(t) - W_d n_{0D}(t)n_D(t)n_A(t)$$
(1.73)

where

$$W_d = 9\pi C_{DD}^{3/4} C_{DA}^{1/4} \tag{1.74}$$

is the transfer parameter which is independent of the activator concentration.

It can be seen that the diffusion model yields a third power concentration dependent transfer term in the rate equation.

1.6.3 The many-body process

Grant [53] emphasized that for a random distribution of donors and acceptors the transition probability is determined by the number of interacting particles and not the spatial dependence of the interaction. Thus, for a random distribution a Q-particle process should be characterized by an no dependent transfer term in the rate equations. To date all the many-body theories are limited to three-body electric multipole interactions [60], [61].

a). The three-body theory[60]

The three-body interaction transfer arise from the dipole-dipole perturbation Hamiltonian. Considering a donor ion D initially in an excited state $|D_1\rangle$ interacting with acceptor ions A_1 and A_2 in states $|A_{11}\rangle$ and $|A_{21}\rangle$, respectively. The rate of radiationless energy transfer between the initial state and a quasicontinuous range of final states is given by:

$$\gamma_{if} = (4\pi^2/h) |\langle i|\tau|f \rangle|^2 S \qquad (1.75)$$

where S is the overlap integral and τ is given to the second

order in the perturbation by:

$$\tau = H' + \sum_{m=1}^{\infty} H' |m\rangle m |H'(\varepsilon_i - \varepsilon_m)^{-1}$$
 (1.76)

Assuming that |i> (or |f>) may be represented as a simple product of three one-electron atomic wave-functions:

$$|i\rangle = \psi(D_i) \psi(A_{1i}) \psi(A_{2i}) \tag{1.77}$$

Neglecting the exchange effects, The interaction Hamiltonian is

$$H' = H'_{DA_1} + H'_{DA_2} + H'_{A_1A_2} \tag{1.78}$$

with each of the three terms on the right side of (1.78) of the following form:

$$H_{DA}^{\prime} = (e^2/kR_{DA}^3) \mathbf{r}_D \cdot \mathbf{T}(DA) \cdot \mathbf{r}_A + higher-order-terms,$$
 (1.79)

where

$$T(DA) = 1 - 3 (\hat{R}_{DA} \hat{R}_{DA})$$
 (1.80)

and \mathbf{r}_D and \mathbf{r}_A are the electric dipole moment operators for D and A, \mathbf{R}_{DA} is the vector separation of D and A. For dipole-dipole interaction the higher order terms on the right-side of (1.79) are not considered.

For the second-order contribution to $\langle i | \tau | f \rangle$ we have:

$$\sum_{m \neq i} \langle i | H' | m \rangle m | H' | f \rangle (\varepsilon_i - \varepsilon_m)^{-1}$$
 (1.81)

A typical term in (1.81) is

$$\sum_{D_{m}} \sum_{A_{1m}} \sum_{A_{2m}} \langle D_{i} A_{1i} A_{2i} | H_{DA_{1}}' | D_{m} A_{1m} A_{2m}' \rangle \\ \langle D_{m} A_{1m} A_{2m} | H_{DA_{2}}' | D_{i} A_{1i} A_{2i}' \rangle (\epsilon_{i} - \epsilon_{m})^{-1}$$
(1.82)

which may be rewritten as:

$$\sum_{D_{n}}\sum_{\mathbf{A}_{1:n}}\sum_{\mathbf{A}_{2:n}}\langle D_{i}\mathbf{A}_{1:i}|H_{D\mathbf{A}_{1}}^{\prime}|D_{m}\mathbf{A}_{1:n}^{\prime}\rangle\mathbf{A}_{2:i}|\mathbf{A}_{2:n}\rangle$$

$$\langle D_{m}\mathbf{A}_{2:n}|H_{D\mathbf{A}_{2}}^{\prime}|D_{f}\mathbf{A}_{2:f}^{\prime}\rangle\mathbf{A}_{1:n}|\mathbf{A}_{1:f}^{\prime}\rangle(\varepsilon_{i}-\varepsilon_{f})^{-1}$$
(1.83)

By orthogonality, (1.83) may be reduced to:

$$\sum_{D_{\alpha}} \langle D_{i} A_{1i} | H'_{DA_{1}} | D_{m} A_{1f} \rangle \langle D_{m} A_{2i} | H'_{DA_{2}} | D_{f} A_{2f} \rangle \langle \varepsilon_{i} - \varepsilon_{m} \rangle^{-1}, \qquad (1.84)$$

By invoking the approximation that

$$\varepsilon_i - \varepsilon_m - \Delta \varepsilon$$
 (1.85)

for all intermediate states m. Thus, the second-order contribution (1.81) becomes:

$$(\Delta \epsilon)^{-1} \langle i | H'H' | f \rangle \qquad (1.86)$$

From Eqs. (1.75), (1.76), (1.78) and (1.86) the three-body dd-dd interaction transfer rate is obtained:

$$\gamma_{if} = (4\pi^{2}/h) |\langle i | \tau | f \rangle|^{2} S
\sim (16\pi^{2}/h) \Delta \varepsilon^{-2} |\langle i | H_{DA_{1}}^{\prime} H_{DA_{2}}^{\prime} | f \rangle
+ \langle i | H_{DA_{1}}^{\prime} H_{A_{1}A_{2}}^{\prime} | f \rangle + \langle i | H_{DA_{2}}^{\prime} H_{A_{1}A_{2}}^{\prime} | f \rangle|^{2} S$$
(1.87)

From Equation (1.79) the specific form for each of the three terms on the rhs of (1.87) is obtained as:

$$\langle i | H'_{DA_1} H'_{DA_2} | f \rangle = (e^4 / k^2 R_{DA_1}^3 R_{DA_2}^3) \langle A_{1i} | r_{A_1} | A_{1f} \rangle$$

$$\cdot T(DA_1) \langle D_i | (r_D r_D | D_i) \cdot T(DA_2) \langle A_{2i} | r_{A_1} | A_{2f} \rangle$$
(1.88)

$$\langle i | H_{Dh_1}^{\prime} H_{A_1 A_2}^{\prime} | f \rangle = \left(e^4 / k^2 R_{Dh_1}^3 R_{A_1 A_2}^3 \right) \langle D_i | r_D | D_i \rangle$$

$$\cdot T(DA_1) \langle A_{1i} | (r_{A_1} r_{A_1}) | A_{1i} \rangle \cdot T(A_1 A_2) \langle A_{2i} | r_{A_1} | A_{2i} \rangle$$

$$(1.89)$$

$$\langle i | H'_{DA_2} H'_{A_1A_2} | f \rangle = \left(e^4 / k^2 R_{DA_2}^3 R_{A_1A_2}^3 \right) \langle D_i | x_D | D_i \rangle$$

$$\cdot \mathbf{T} \langle DA_2 \rangle \langle A_{2i} | (x_{A_2} x_{A_3}) | A_{2i} \rangle \cdot \mathbf{T} \langle A_1 A_2 \rangle \langle A_{1i} | x_{A_1} | A_{1i} \rangle$$
(1.90)

Thus the transition rate contains terms that exhibit the following types of dependence on separation between the three ions: $R_{DA1}^{-6}R_{DA2}^{-6}$, $R_{DA1}^{-6}R_{A1A2}^{-6}$, $R_{DA2}^{-6}R_{A1A2}^{-6}$, $R_{DA2}^{-6}R_{A1A2}^{-6}$, $R_{DA1}^{-6}R_{DA2}^{-3}R_{A1A2}^{-3}$, $R_{DA1}^{-3}R_{DA2}^{-6}R_{A1A2}^{-6}$.

The total transfer rate is the ensemble

$$\langle \gamma_{123} \rangle_{T} = \langle 1/Z \rangle \sum_{x_{1}} \sum_{s_{1}} \sum_{t_{1}} \gamma \langle x_{1}, s_{1}, t_{1} \rangle \times \sum_{s_{1}} \cdots \sum_{t_{1}} e^{-U(x_{1}, x_{2}, \dots, x_{N_{1}}, s_{1}, s_{2}, \dots, s_{N_{2}}, t_{1}, t_{2}, \dots t_{N_{3}})/kT}$$

$$(1.91)$$

where Z is the partition function which can be written

$$Z = \sum_{a,c,} e^{-U(x_1, x_2, \dots, x_{N_1}, x_2, \dots, x_{N_2}, t_1, t_2, \dots t_{N_3})/kT}$$
 (1.92)

and the sum is carried over all configurations of energy U with the position vectors of the donor and acceptor ions given by **r**, **s**, and **t**, respectively. For a random distribution of the activator ions

$$Z=\mathbf{Q}(N, N_1, N_2, N_3) = N! / (N-N_1-N_2-N_3)! N_1! N_2! N_3!$$
 (1.93)

where N is the total number of lattice sites, and $(N-N_1-N_2-N_3)$ is the number of vacant lattice sites. Thus:

$$\langle \gamma_{123} \rangle_T = (N_1 N_2 N_3 / N^3) \sum_{\mathbf{r}_1} \sum_{\mathbf{s}_2} \sum_{\mathbf{t}_2} \gamma (\mathbf{r}_1, \mathbf{s}_1, \mathbf{t}_1)$$
 (1.94)

Since the lattice spacing is small compared with the

macroscopic dimensions, the sum in (1.94) may be replaced by a integral. The total transfer rate per volume (the transfer term in the rate equation) is then given by:

$$\frac{1}{V} \langle \gamma_{123} \rangle_{T} = \frac{N_{1}N_{2}N_{3}}{V^{3}} \int_{R_{0}}^{R_{2}} 4\pi R_{12}^{2} dR_{12} \int_{R_{0}}^{R_{2}} \gamma_{123} (R_{12}, R_{13}) 4\pi R_{13}^{2} dR_{13} \qquad (1.95)$$

$$= n_{1}n_{2}n_{3}w_{123}$$

where w_{123} is the three-body interaction transfer parameter which is a constant, and n_1 , n_2 and n_3 are the concentration of the three activators.

b) Judd[11]-Ofelt[12] parameter expression of the threebody transfer rates

The Judd-Ofeld parameter expression of the three-body electric dq-dq interaction energy transfer rate in rare-earth ion doped crystals were also developed by Kushidand[23]. The result is:

In (1.96) Ξ is the quantity defined as:

$$\mathbb{E}(k_{1},k) = 2\sum_{n',1'} \{ \frac{1}{f} \frac{K K_{1}}{f} | \langle 4f|r|n'l \langle k'l'|r^{k_{1}}|4f \rangle \\ \langle f||C^{(1)}||1' \langle l'||C^{(k_{1})}||f \rangle / \Delta(n'l') \}$$
(1.97)

where

$$\Delta (n'l') \approx E_{ab} - E_{\mu b'} \approx E_{a'b'} - E_{\mu b} \approx E_{a'c'} - E_{\mu c} \approx E_{ac} - E_{\mu c'}$$
 (1.98)

1.7 Statement of the Problem

The second order kinetic treatment of the energy transfer process, which results in n_0n_A dependence of the energy transfer term in the coupled rate equations, has gained wide acceptance in the analysis of upconversion dynamics[44], [45],[46],[52]. This approach was used to analyze data on the upconversion dynamics of Er^{3+} :YAlO₃ after excitation with a 1.55 μ m pulse[62]. To obtain a satisfactory fit to the Er^{3+} :YAlO₃ data, not only the energy transfer parameters but also the decay rates were required to be adjustable parameters. Attempts to fit similar data acquired for Er^{3+} :YAG were unsuccessful for any set of parameters we could find. This difficulty led us to ask the question: "are the second order kinetics valid in these cases?"

Although the three level model[52] can fit the time dependent upconversion intensity data of Nd³*LiYF4 below the avalanche threshold, model the time dependent upconversion data above the avalanche threshold and the pump power dependent upconversion data, it can not fit the data at high pump power (160 mW and 50-mm focal lens). When we undertook the study of avalanche upconversion dynamics of Tm³*:LiYF4, we found it impossible to fit the time dependent data, especially at high pump power (above the threshold) and high temperature (room temperature) by a simple three level model[52]. Even a

four or five level model which only included the cross-relaxation energy transfer processes and second order kinetics failed. It became clear that the experimental upconversion kinetics of Tm³⁺:LiYF₄ is complicated and it can not be adequately described by a simple avalanche model. This difficulty motivated the detailed examination of the avalanche upconversion kinetics of this work.

Upconversion pumped laser emission has been previously reported for Tm^{3+} : $Y_2BaF_8[63]$. But to date there has been no studies on the upconversion dynamics and the upconversion gain reported for this material. This work addresses this question by Pump-probe measurements, which are compared to similar results for Tm^{3+} : $YLiF_4[64]$.

1.8 Objectives of the research

- a). To understand the upconversion dynamics of Er^{3+} :YAG and Er^{3+} :YAlO₃.
- b). To understand the avalanche upconversion dynamics of Tm^{3+} : YLiF4 and Tm^{3+} : Y2BaF8.
- c). Through the investigation of the upconversion dynamics of Er^{3+} :YAG and Er^{3+} :YAlO₃, and of the avalanche upconversion dynamics of Tm^{3+} :YLiF₄ and Tm^{3+} :Y₂BaF₈ to understand the energy transfer kinetics particularly for high power excitation and high activator concentration (where second order kinetics fails).

CHAPTER 2

EXPERIMENTAL METHODS AND DATA TREATMENT

2.1 Time dependent upconversion intensity measurements

2.1.1 Upconversion emission in Er3+: YAG and YAlO3 (These data were provided by D. J. Simkin and P. Myslninski)

Measurements were made at room temperature using a single crystal of YAG containing 3 atomic percent Er3+(4.20×1020 cm-3) and a single crystal of YAlO, containing 10 atomic percent $\mathrm{Er}^{3+}(1.97\times10^{21}~\mathrm{cm}^{-3})$ and codoped with 1 atomic percent Yb³⁺. The sample was in the form of a laser rod, with flat polished end faces and the crystallographic c axis perpendicular to the rod axis. Pulsed measurements were made using a Q-switched erbium fibre laser (constructed at NRC) which provided pulses of ca. 0.5 µJ and 15 ns duration. The output wavelength of the laser was tunable from about 1.52 μm to 1.56 μm. The laser was focused to a spot size of approximately 20 µm in the sample, and the resulting upconversion fluorescence was focused on the a photon Technologies International 0.25 m slits of monochromator equipped with a 600 groove/mm holographic grating (<0.5 nm resolution). A Hamamatsu R928 photomultiplier was used as the detector, and the output was fed directly to a LeCroy 9420 digital oscilloscope. The system response time (limited primarily by the cable capacitance) was found to be <1 μs .

A disc of 2.15 mm thickness, polished on both faces, was cut from the laser rod and used to record the absorption spectrum with a Perkin-Elmer model Lambda 9 spectrophotometer. The same disc was used to record the upconversion emission

spectrum, and the variation of emission intensity with pump power. This was accomplished by optically coupling the disc to the optical fibre input of an Anritsu spectrum analyzer (resolution 5nm) using index matching grease. The Er-fibre laser, operating in continuous mode (maximum output power ca 20 mW), was focused to a spot size of ca 40 μ m on the disc. The laser power was attenuated using a variable neutral density filter.

2.1.2 Upconversion emission in Tm3+:YLiF4 and Y2BaF8

The optical arrangement used is illustrated in figure 2.1. Measurements were performed on a single crystal of YLiF4 3.37 mm thick and containing 3 at.% (1.98×10 20 cm $^{-3}$) Tm $^{3+}$ (obtained from Sanders Associates) and a single crystal of Y_2BaF_8 5.00mm thick and containing 5 at.% (6.50×10²⁰ cm⁻³) Tm³⁺ (obtained from Hans P. Jenssen), at 12° K and at room temperature with the crystal mounted on the cold finger of a closed cycle helium refrigerator. For Tm3+:YLiF, two polarizations were examined: σ - with the c-axis perpendicular to both the electric vector of the laser and to the direction of propagation, and π - with the c-axis parallel to the electric vector of the laser, but perpendicular to the direction of propagation. For Tm3+:Y2BaF8 the c-axis is perpendicular to electric vector of the laser and parallel to the direction of propagation. The pump light was provided by a Coherent 699-21 ring dye laser operating with DCM dye, and

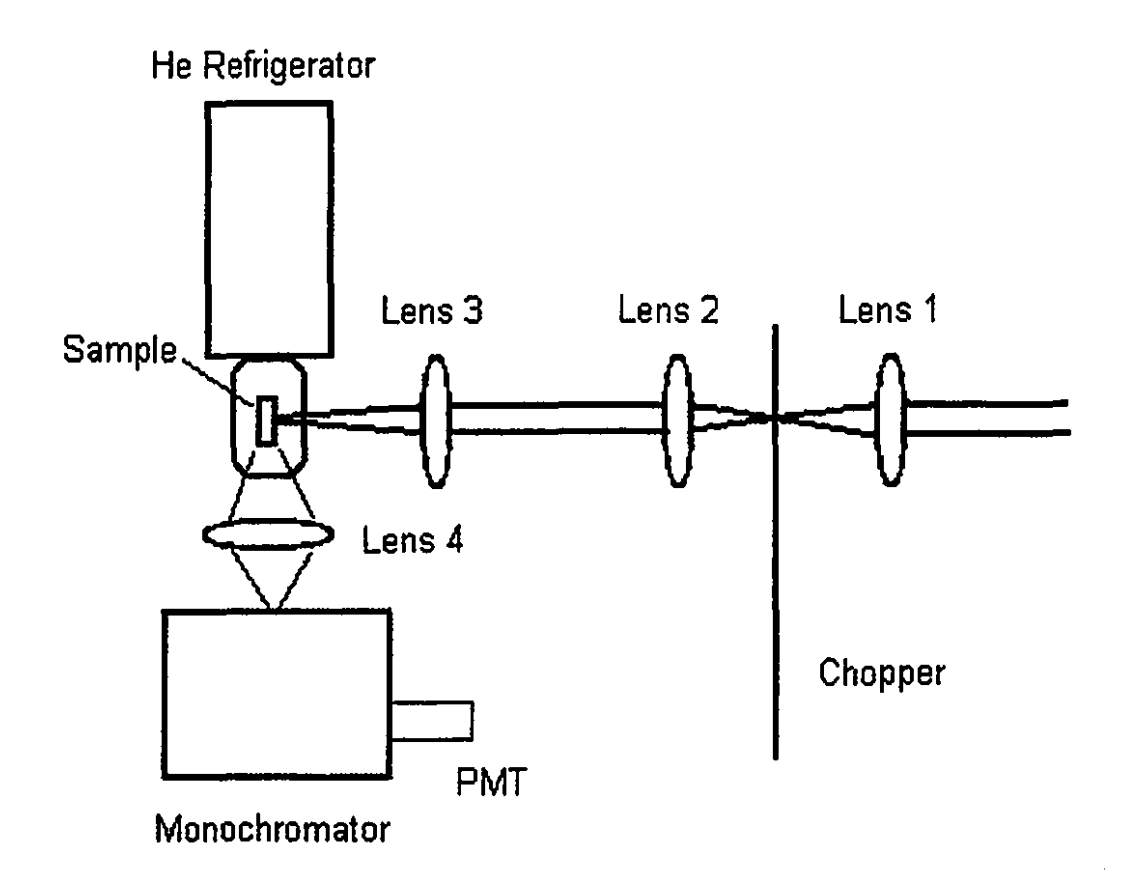


Figure 2.1

Optical arrangement for the time dependent upconversion emission measurement.

pumped with 6.0 W single line 514.5 nm from a Coherent C100 15 The pump light was focused on the crystal W Ar ion laser. using a lens of focal length chosen such that the Rayleigh range was longer than the crystal thickness (4.13 mm @ 650 The beam waist was determined to be 20.6 um as measured The luminescence from the crystal was with a knife edge. collected at right angles and focused onto the slits of a Photon Technologies International 0.25 m monochromator equipped with a 600 groove/mm holographic grating (<0.5 nm resolution). A Hamamatsu R928 photomultiplier was used as the detector, and the signal was fed via an impedance matching preamplifier to a Tektronix 2230 digital storage oscilloscope. The response time of the electronics was 200 ns. The laser was chopped at 5 Hz, slow enough to allow the population of the longest lived state (${}^{3}H_{4}$, 13 ms) to deplete between cycles. The pump laser was focused before the chopper blade and recollimated after so that the rise of the pump light was much shorter than the risetime of the upconversion emission.

2.2 Power dependence of the upconversion intensity measurement

The optical arrangement for the pump power dependence upconversion intensity measurement is the same as that for the time dependent upconversion intensity measurement as shown by Figure 2.1 except that the monochromator was replaced by an EG&G PARC OMA. The pump power dependence of the upconversion

intensities in Tm^{3+} :YLiF, were measurement at 12 k with pump power ranging from 20 mW/3.42×10⁻⁵cm² to 270 mW/3.42×10⁻⁵cm².

2.3 Pump-probe gain measurement

In the gain measurements the sample of Tm3+: Y2BaF8 was mounted on the cold finger of a closed cycle He refrigerator. The optical arrangement used is illustrated in figure 2.1. The blue probe radiation was provided by a Laser Science, Inc. model VSL-337ND pulsed N2 laser pumping a model DLMS-230 dye laser using Coumaring 480 dye. The probe beam was attenuated to obtain comparable intensity to that of the luminescence. Pump light was provided by a Coherent 699 ring dye laser (in broadband configuration) using DCM and pumped with an argon ion laser at 514.5 nm. The direction of the polarization was the same for both lasers, and the crystal was oriented with the c-axis to be perpendicular to electric vector of the laser and to be parallel to the direction of propagation. The focal length of lens L2 was chosen so that the Rayleigh range was longer than the crystal length for both pump (4.13 mm @ ~650.5 nm) and probe (5.52 mm at ~482 nm) wavelengths. This resulted in a beam waist of radius 20.6 µm for both beams as measured with a knife edge. This corresponded to an average intensity of 7.5 kw cm⁻² for each 100 mW of incident pump power. All measurements were made using an EG&G OMA with an intensified 1024 element diode array detector. The OMA was synchronized with the N₂ laser pulses. The resolution of the spectrograph

OPTICAL ARRANGEMENT

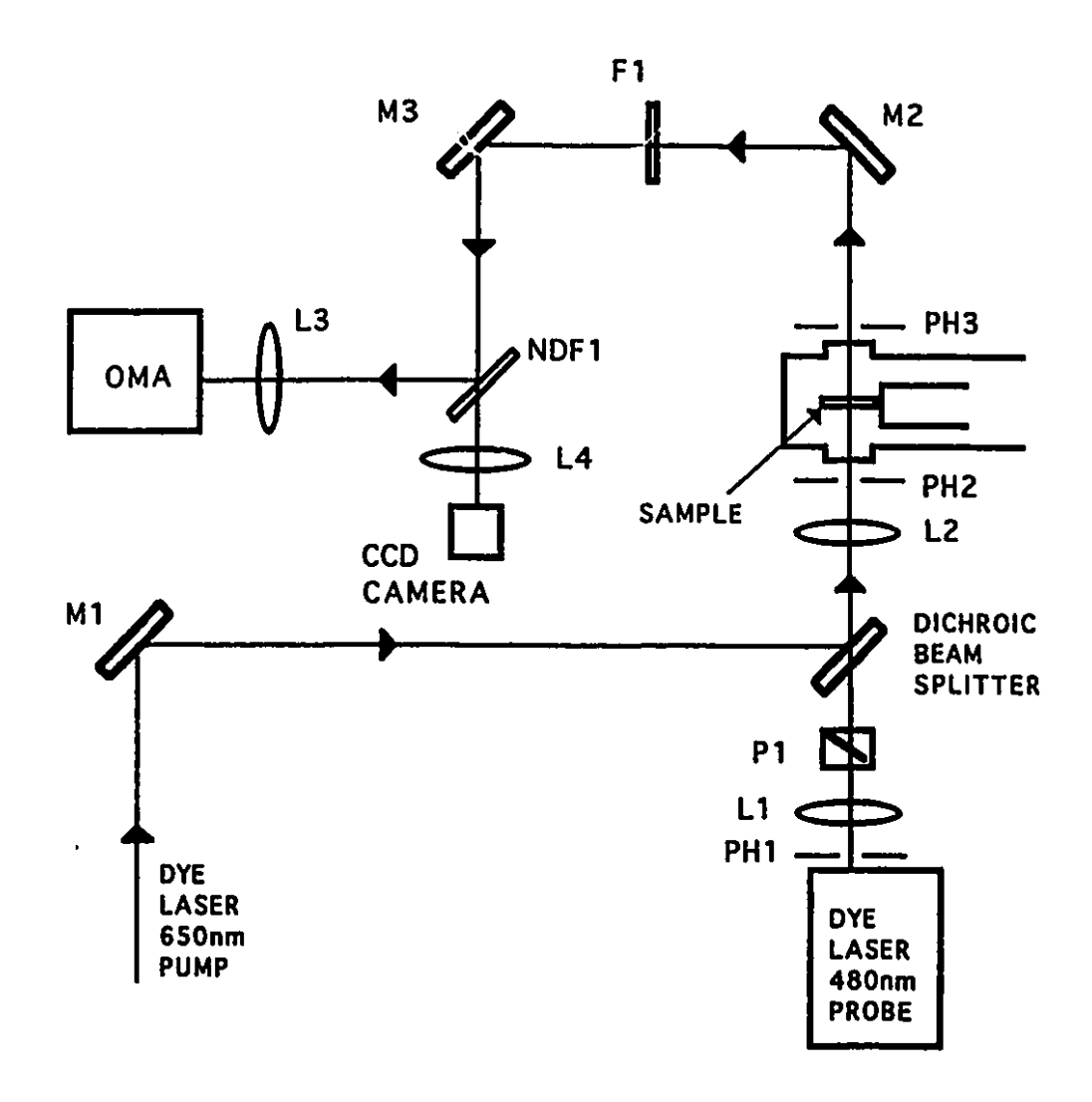


Figure 2.2

Optical arrangement for the pump-probe gain measurement.

at 500 nm was 0.3 nm. To determine the gain we recorded three complete spectra, one with both the pump and probe lasers present, one with only the pump, and one with only the probe. We then subtracted the pump only spectrum from the pump plus probe spectrum and compared the result to the probe only spectrum to obtain the numerical value of the gain at the probe wavelength. To eliminate pulse-to-pulse jitter we averaged one hundred samples in each case. This approach led to an error of less than 3% of the measured gain. The accuracy was not as high as the precision due to the systematic error introduced by variations in pump-probe beam overlap.

2.4 Data treatment

2.4.1 Numerical methods for the solution of the coupled rate equations

The upconversion dynamics is described by the coupled rate equations. In the computer program the coupled rate equations were normalized by the total doped rare-earth ion concentration. The normalized coupled rate equation are solved with a program that employs the IMSL library routine "DVERK", employing a RUNGE KUTTA - VERNIER fifth and sixth order method. The program used the solutions provided by DVERK as the fitting functions for the routine ZXMIN, which could vary the chosen parameters and seek a minimum in the square deviation to the experimental data. The time dependent upconversion intensity obtained from the numerical solution of

the coupled rate equations could be compared with the experimental data to determine the best values for the parameters in the rate equations.

2.4.2 Choice of parameters to vary and choice of parameter values

The coupled rate equations contain pump terms, self decay terms and energy transfer terms. The radiative decay rates can be obtained from the Judd-Ofelt parameters so they could be used as fixed values in the solution of the rate equations. The pump rates, theoretically, can be calculated if values of the line shape overlap function are known. The value of the line shape overlap function is determined by many factors that include the mismatch of the pump energy with the energy gap between the two energy levels pumped, the absorption crosssection of the line shape of the laser and of the absorption band. Thus it is too complicated to calculate the pump rates accurately. However, the pump rates under perfect resonant condition can be reasonably estimated. The actual pump rates must be smaller than the estimated ones. For these reasons the pump rate (for continuous pump case), or initial population of the excited state (for pulsed pump case), are chosen as variable parameters.

The energy transfer parameters are determined by the kinetics (two-body interaction, or many-body interaction, dipole-dipole transfer or dipole-quadruple transfer...) and

the values of the overlap of the line shape functions. Since one of the main goals of this study was to understand the kinetics of the energy transfer, the energy transfer parameters are chosen as parameters to vary to fit the experimental data. Thus by comparing the fitted values of the energy transfer parameters with the calculated ones we can obtain information about the kinetics, and test the validity of the kinetic model used.

2.4.3 Fitting to more than one level when possible

In our study the rate equations for Er³⁺:YAG, Er³⁺:YAlO₃ and Tm³⁺:Y₂BaF₈ require five energy levels, and Tm³⁺:YLiF₄ six energy levels. Even with as many of the parameters fixed as possible, it is still advantageous to further constrain the computer modelling. This was achieved by simultaneous fitting to two experimental levels whenever possible. This approach gives greater confidence in the significance of the values found for the variable parameters, and as a result, in the kinetic model.

2.4.4 Treatment of the gain data

The gain is obtained from $[I_{(pump+probe)} - I_{pump}] / I_{probe}$. $I_{(pump+probe)}$, I_{pump} and I_{probe} are determined from the integrated intensities under the peak centred at the probe wavelength. Because the dye laser used to provide the probe beam contained broad amplified spontaneous emission (ASE) in the wings, the

difference spectra $I(\lambda)_{(pump+probe)}$ - $I(\lambda)_{pump}$ can reveal qualitative spectral features, such as excited state absorption and stimulated emission in regions outside the narrow probe laser wavelength.

CHAPTER 3 RESULTS AND DISCUSSIONS

3.1 Upconversion dynamics of Er3+: YAG and Er3+: YAlO3

Figure 3.1 shows the energy levels and various decay and energy transfer processes which we consider in treating the upconversion dynamics of Er^{3+} in both YAG, and YAlO₃. The decay rates A_{ij} indicate the rate from state i to state j, by either radiative or non-radiative (multiphonon) processes. The energy transfer parameters are indicated as W_{ij} where i and j refer to the transfer occurring from an ion in state i to another ion in state j. To simplify the scheme as much as possible, we have considered the $^4I_{11/2}$ and the $^4I_{9/2}$ levels as one level[65]. This leads to the following set of rate equations.

$$\begin{split} \dot{n}(4) &= -\left[A_{43} + A_{42} + A_{41} + A_{40} \right] n(4) \\ &+ W_{2222} n^4 (2) + W'_{1122} n^2 (1) n^2 (2) \\ \dot{n}(3) &= A_{43} n(4) - \left[A_{32} + A_{31} + A_{30} \right] n(3) \\ &+ W_{1122} n^2 (1) n^2 (2) \\ \dot{n}(2) &= A_{42} n(4) + A_{32} n(3) - \left[A_{21} + A_{20} \right] n(2) \\ &+ W_{1111} n^4 (1) - 2 W_{2222} n^4 (2) \\ &- \left[W_{1122} + W'_{1122} \right] n^2 (1) n^2 (2) \\ \dot{n}(1) &= A_{41} n(4) + A_{31} n(3) + A_{21} n(2) - A_{10} n(1) \\ &- 2 W_{1111} n^4 (1) \\ &- \left[W_{1122} + W'_{1122} \right] n^2 (1) n^2 (2) \\ \dot{n}(0) &= A_{40} n(4) + A_{30} n(3) + A_{20} n(2) + A_{10} n(1) \\ &+ W_{1111} n^4 (1) + W_{2222} n^4 (2) \\ &+ \left[W_{1122} + W'_{1122} \right] n^2 (1) n^2 (2) \end{split}$$

where n(i) are concentration of ions in state i and W_{iijj} are fourth-order transfer parameters. Using the above equations to treat the energy transfer processes, the same ion in different energy levels is either the donor or acceptor. Since this kinetic scheme includes five levels, there can be as many as four different donors and four different acceptors.

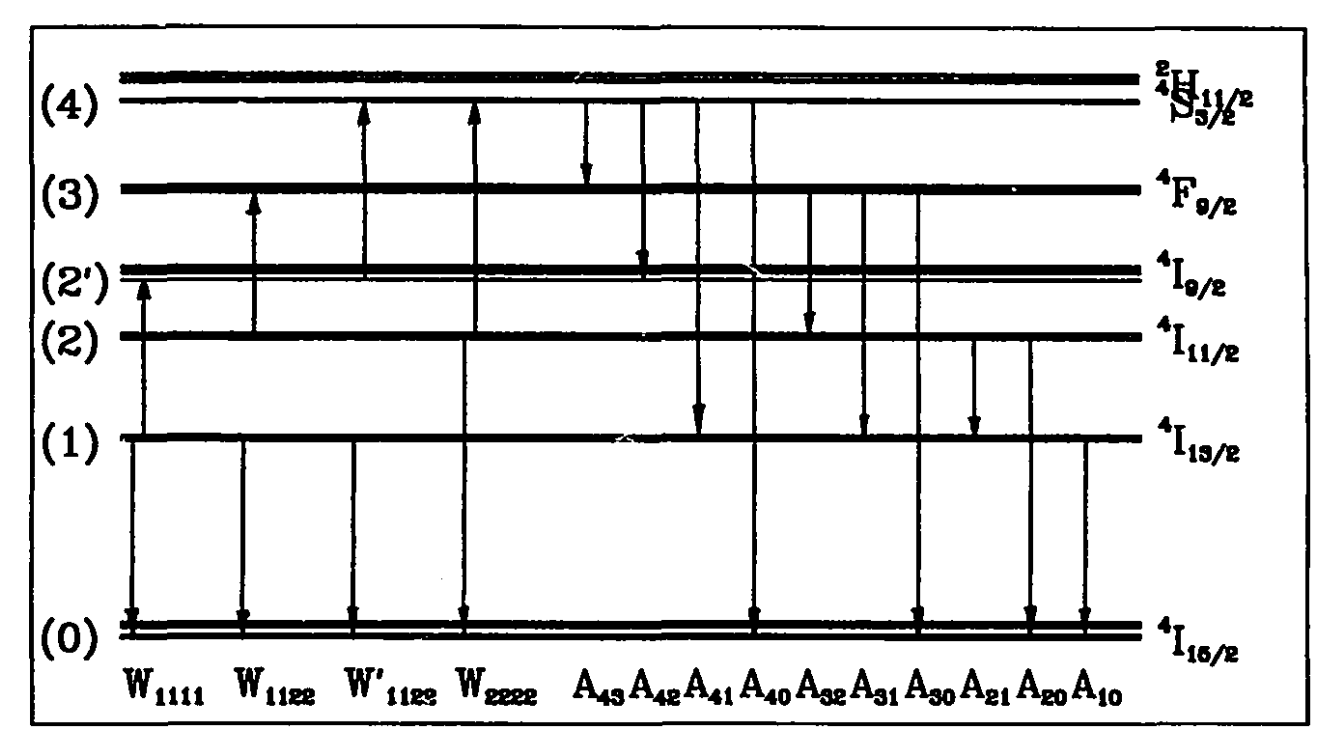


Figure 3.1

Energy level scheme of Er^{3+} showing the energy transfer and decay processes considered in the rate equations for the upconversion dynamics of Er^{3+} :YAG and Er^{3+} :YAlO₃.

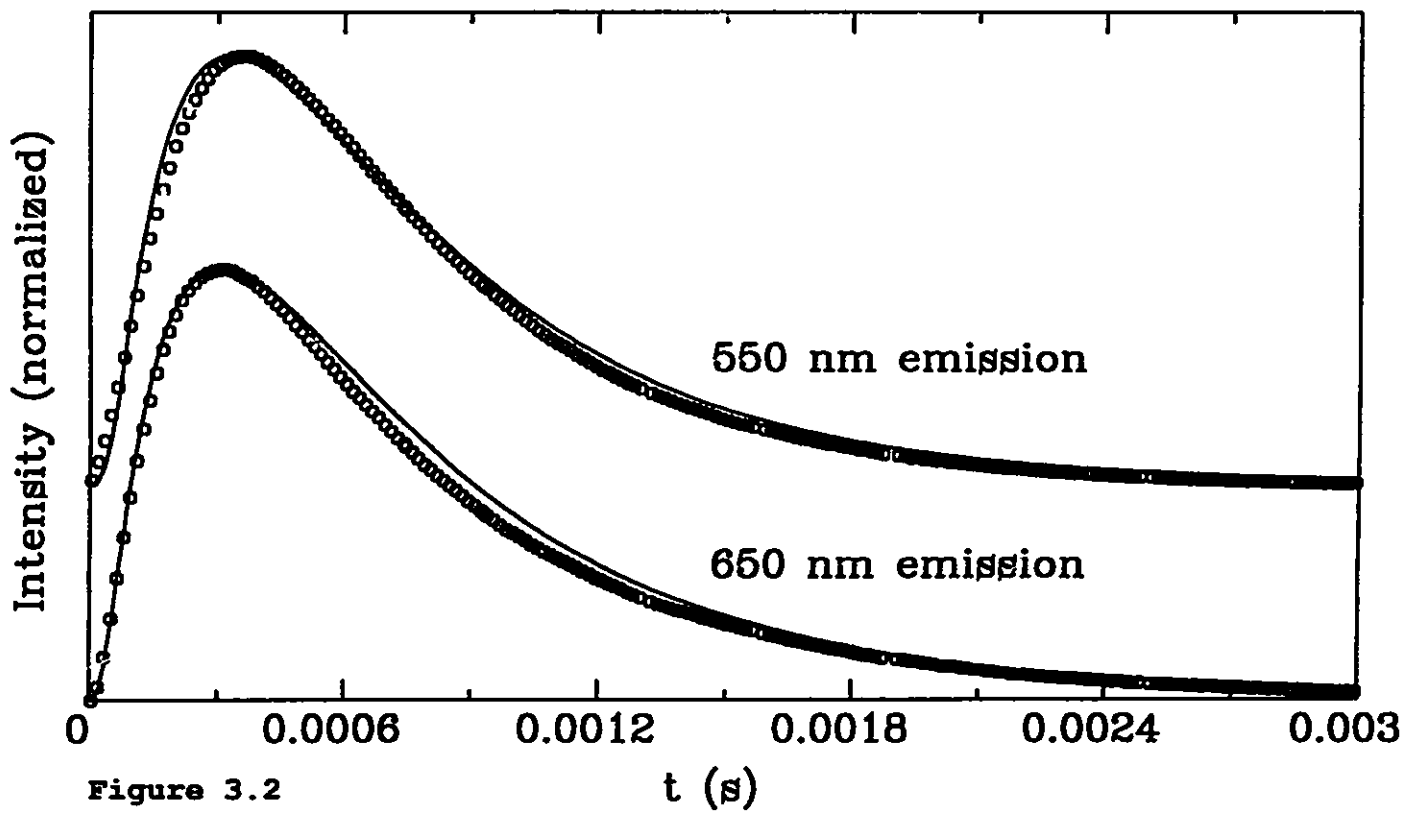
Considering donor-acceptor energy matching we have included only the above four energy transfer process. Dividing the total $\rm Er^{3+}$ concentration $\rm n_{Er}$ (for $\rm Er^{3+}:YAG$ $\rm n_{Er}=4.20\times10^{20}$ cm⁻³ and for $\rm Er^{3+}:YAlO_3$ $\rm n_{Er}=1.97\times10^{21}$ cm⁻³) on both sides of the coupled rate equations (3.1), we obtain the following normalized coupled rate equations:

$$\begin{split} \dot{\rho}\left(4\right) &= -\left[A_{43} + A_{42} + A_{41} + A_{40}\right] \rho\left(4\right) \\ &+ K_{2222} \rho^4\left(2\right) + K'_{1122} \rho^2\left(1\right) \rho^2\left(2\right) \\ \dot{\rho}\left(3\right) &= A_{43} \rho\left(4\right) - \left[A_{32} + A_{31} + A_{30}\right] \rho\left(3\right) \\ &+ K_{1122} \rho^2\left(1\right) \rho^2\left(2\right) \\ \dot{\rho}\left(2\right) &= A_{42} \rho\left(4\right) + A_{32} \rho\left(3\right) - \left[A_{21} + A_{20}\right] \rho\left(2\right) \\ &+ K_{1111} \rho^4\left(1\right) - 2K_{2222} \rho^4\left(2\right) \\ &- \left[K_{1122} + K'_{1122}\right] \rho^2\left(1\right) \rho^2\left(2\right) \\ \dot{\rho}\left(1\right) &= A_{41} \rho\left(4\right) + A_{31} \rho\left(3\right) + A_{21} \rho\left(2\right) - A_{10} \rho\left(1\right) \\ &- 2K_{1111} \rho^4\left(1\right) \\ &- \left[K_{1122} + K'_{1122}\right] \rho^2\left(1\right) \rho^2\left(2\right) \\ \dot{\rho}\left(0\right) &= A_{40} \rho\left(4\right) + A_{30} \rho\left(3\right) + A_{20} \rho\left(2\right) - A_{10} \rho\left(1\right) \\ &+ K_{1111} \rho^4\left(1\right) + K_{2222} \rho^4\left(2\right) \\ &+ \left[K_{1122} + K'_{1122}\right] \rho^2\left(1\right) \rho^2\left(2\right) \end{split}$$

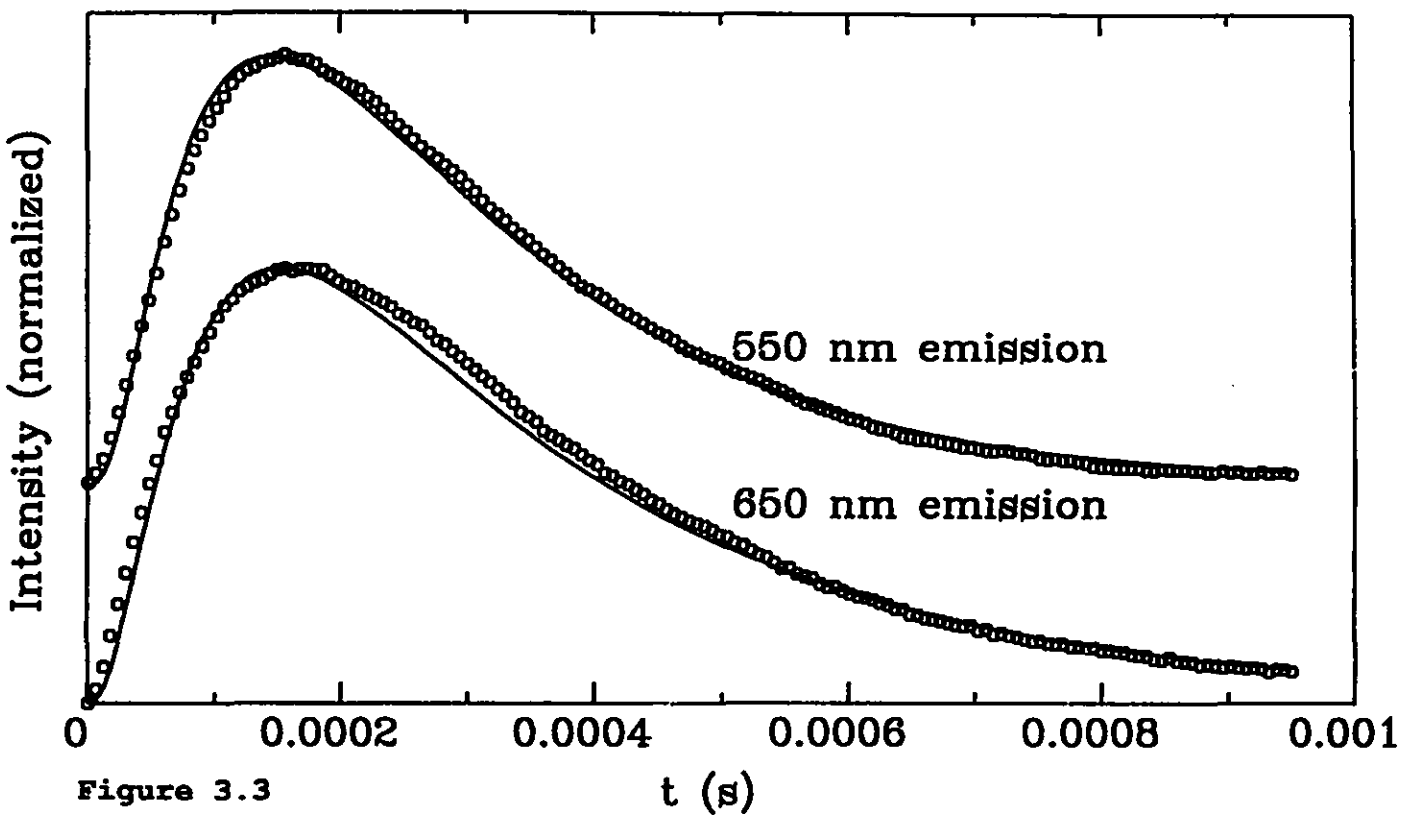
where $\rho(i)=n(i)/n_{Er}$ are normalized concentrations and $K_{iijj}=W_{iijj}n_{Er}^3$. Using equations (3.2), we fitted the experimental data with the help of a computer program that employs the IMSL library routine "DEVERK". In fitting the experimental cata, the radiative decay rates are fixed using values determined by calculations (Eq. (1.3)). The fixed values of the radiative decay rates are listed in Table 3.1. The nonradiative decay rates, the initial population of level 1, and the parameters K_{iijj} are allowed to vary to obtain the best fit to the experimental data. Fits of acceptable quality are obtained for both the Er^{3+} :YAG and the Er^{3+} :YAlO₃ experimental data, and are shown in Figure 3.2 and 3.3. The values of the variable

Table 3.1 Fixed radiative decay rates in the fitting of the time dependent upconversion emission intensity experimental data of Er^{3+} :YAG and Er^{3+} :YAlO₃[62].

	Er³+: YAG	Er3+:YAlO3
A ₁₀ (s ⁻¹)	73	92
A ₂₁ (s ⁻¹)	34	49
A ₂₀ (s ⁻¹)	230	356
A ₃₂ (s ⁻¹)	37	49
A ₃₀ (s ⁻¹)	1537	2306
A ₄₂ (s ⁻¹)	76	105
A ₄₁ (s ⁻¹)	315	405
A ₄₀ (s ⁻¹)	782	992



Time dependence of the upconversion emission at 550 nm ($^4\mathrm{S}_{3/2}$) and 650 nm (${}^4F_{9/2}$) from Er^{3+} :YAlO₃ at room temperature, subsequent to a 15 ns pulse at ca. 1550 nm. (STD deviation=0.020668)



Time dependence of the upconversion emission at 550 nm ($^4S_{3/2}$) and 650 nm ($^4F_{9/2}$) from Er $^{3+}$:YAG at room temperature, subsequent to a 15 ns pulse at ca. 1550 nm. (STD deviation=0.012717)

parameters found from this procedure are given in Table 3.2 (the values of the parameters K_{iijj} were obtained directly from the normalized rate equations (3.2), and the transfer parameters W_{iijj} were obtained by dividing K_{iijj} with the third power of the Er^{3+} concentration n_{TE}^{3}).

Finally, we consider the steady state intensity dependence of the upconversion emission upon continuous 1.55 μm pump power. These data were only acquired for Er3+:YAlO3, and are taken from reference [62]. The experimental data for levels 2, 2', 3 and 4 are shown in Figure 3.4, along with the calculated curves. The calculated curves were obtained from the steady state solutions for the normalized rate equations (3.2), with the addition of a pump term from level 0 to level 1, and using the values of the parameters given in Table 3.1 and 3.2. The range of pump rates which gave steady state solutions in agreement with the data (for the range of pump powers used) corresponds to an absorption cross-section, $\sigma=6.6\times10^{-20}$ cm², somewhat larger than the literature[66] value of 1.2×10⁻²⁰ cm². The calculated values of slopes of lnI versus lnP obtained in this way are listed along with the experimental slopes in Table 3.3. As can be seen from Figure 3.4, the agreement is good.

From Table 3.2 we may see that the nonradiative decay rates A_{43} , A_{32} and A_{21} are large. Figure 3.1 shows that the separations between $^4S_{3/2}$ level and $^4F_{9/2}$ level, $^4F_{9/2}$ level and $^4I_{19/2}$ level, $^4I_{11/2}$ level and $^4I_{13/2}$ level all are small, thus at

Table 3.2 Fitted values of the nonradiative decay rates and energy transfer parameters in the fitting of the time dependent upconversion emission intensity experimental data of Er^{3+} :YAG and Er^{3+} :YAlO₃ [62]

	Er³+: YAG	Er3+:YAlO3
A ₂₁ (s ⁻¹) nonradiative	2966	617
A_{32} (s ⁻¹) nonradiative	15107	767
A ₄₃ (s ⁻¹) nonradiative	65987	2185
K ₁₁₁₁ (s ⁻¹)	(1.00±0.06)×108	(1.00±0.06)×108
W ₁₁₁₁ (s ⁻¹ cm ⁹)	(1.35±0.08)×10 ⁻⁵⁴	(1.31±0.07)×10 ⁻⁵⁶
K ₂₂₂₂ (s ⁻¹)	(1.00±0.57)×108	(1.00±0.50)×108
W ₂₂₂₂ (s ⁻¹ Cm ⁹)	(1.35±0.77)×10 ⁻⁵⁴	(1.31±0.66)×10 ⁻⁵⁶
K ₁₁₂₂ (s ⁻¹)	(4.20±0.38)×108	(5.00±0.74)×108
W ₁₁₂₂ (s ⁻¹ cm ⁹)	(5.67±0.51)×10 ⁻⁵⁴	(6.55±0.96)×10 ⁻⁵⁶
K' ₁₁₂₂ (s ⁻¹)	(2.00±0.26)×10 ⁶	(6.20±4.70)×10°
W' ₁₁₂₂ (s ⁻¹ cm ⁹)	(2.70±0.35)×10 ⁻⁵⁶	(8.12±6.17)×10 ⁻⁵⁵
n(1)/n _{Er} , t=0	0.043	0.040
n _{Er} (cm ⁻³)	4.20×10 ²⁰	1.97×10 ²¹

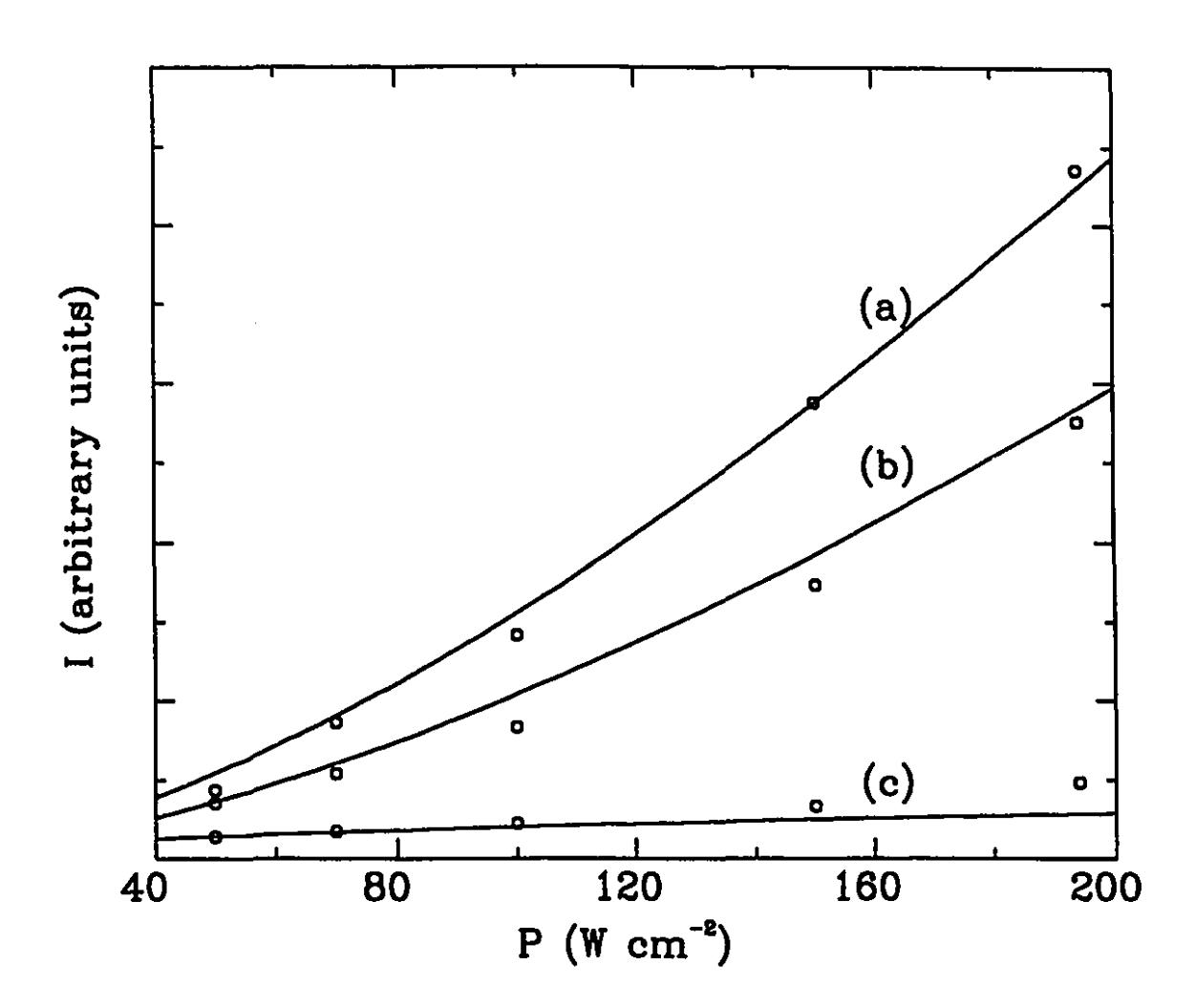


Figure 3.4

Dependence of the upconversion emission intensity of $Er^{3+}:YAlO_3$ on cw 1550 nm laser power. Open circles: experimental points[62], solid lines: fitted using $I = P^m$, values of m given in Table 3.3. (a): ${}^4F_{9/2}$ emission; (b): ${}^4S_{3/2}$ emission; (c): ${}^4I_{11/2}$ emission.

Table 3.3 Dependence of upconverted emission and intensity (I) on 1550 nm pump power (P), according to $I=P^m$.

LEVELS	⁴ I _{11/2}	⁴ F _{9/2}	⁴ S _{3/2}
λ(nm)	997	673	550
m observed	1.06	1.67	1.51
m calculated	0.52	1.51	1.51

room temperature the nonradiative decay rates between these levels are expected to be large.

3.2 Avalanche upconversion dynamics of Tm3+:YLiF4

First we examined the time dependence behaviour at high pumping power (370 mw/3.42×10⁻⁵cm²) and 12 k with different pumping wavelengths. When tuning the single wavelength pump laser through the range of DCM (620-670 nm) one observes strong blue upconversion emission from Tm^{3+} :YLF at several discrete wavelengths. At low temperature (12 K) these excitation wavelengths are quite sharp. It is interesting to note the remarkable differences in the upconversion dynamics found for different excitation wavelengths, and crystal orientations. This is illustrated in Figure 3.5 for σ polarization, and in Figure 3.6 for π polarization. Figure 3.7 shows the energy levels and three different pump steps and Table 3.4 shows the resonance mismatch of these three pumping

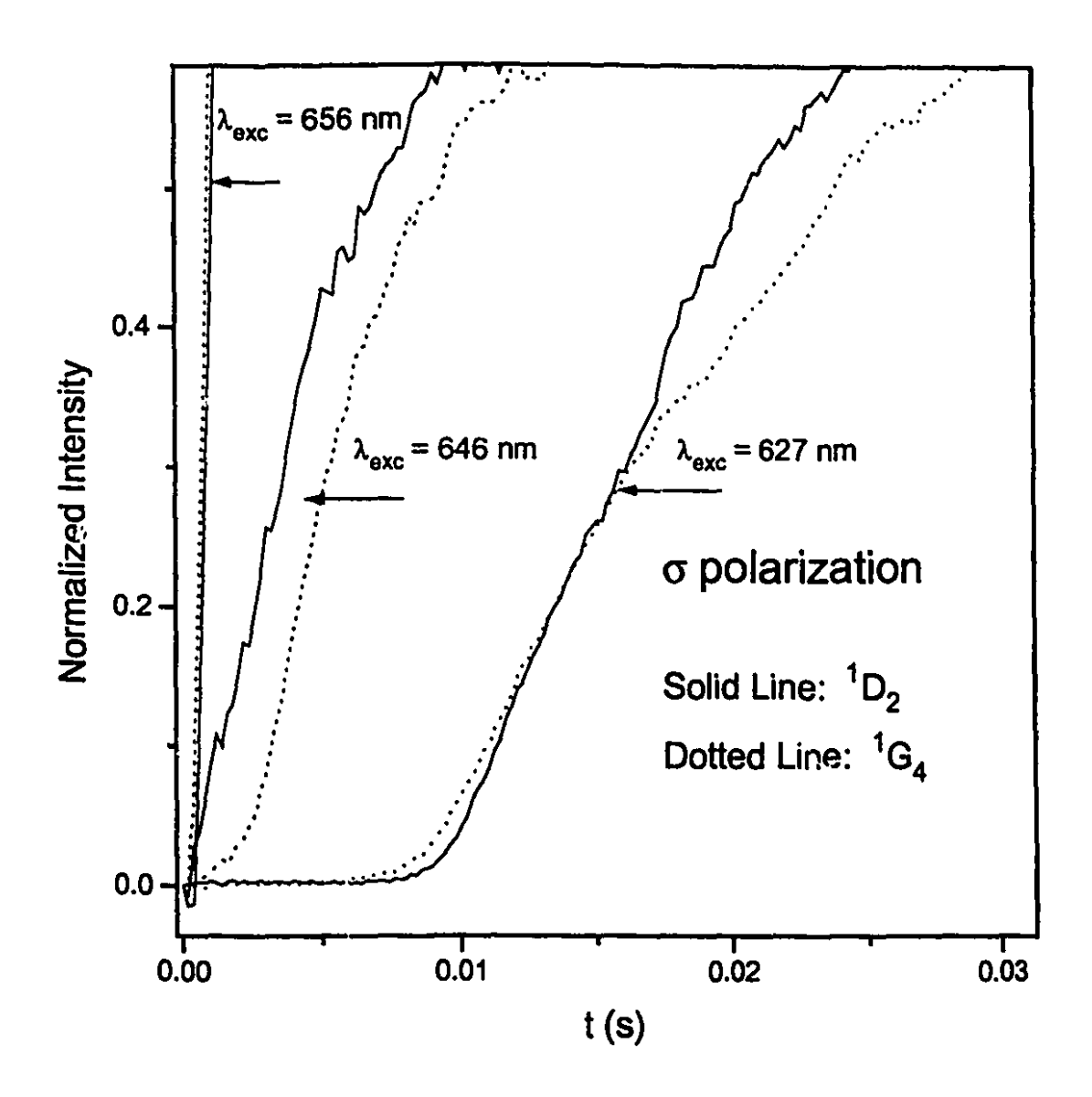


Figure 3.5 Rise time behaviour of the upconversion emission of Tm^3 :YLiF, under 370 mW/3.42×10⁻⁵cm² and σ polarization pump at different pump wavelengths.

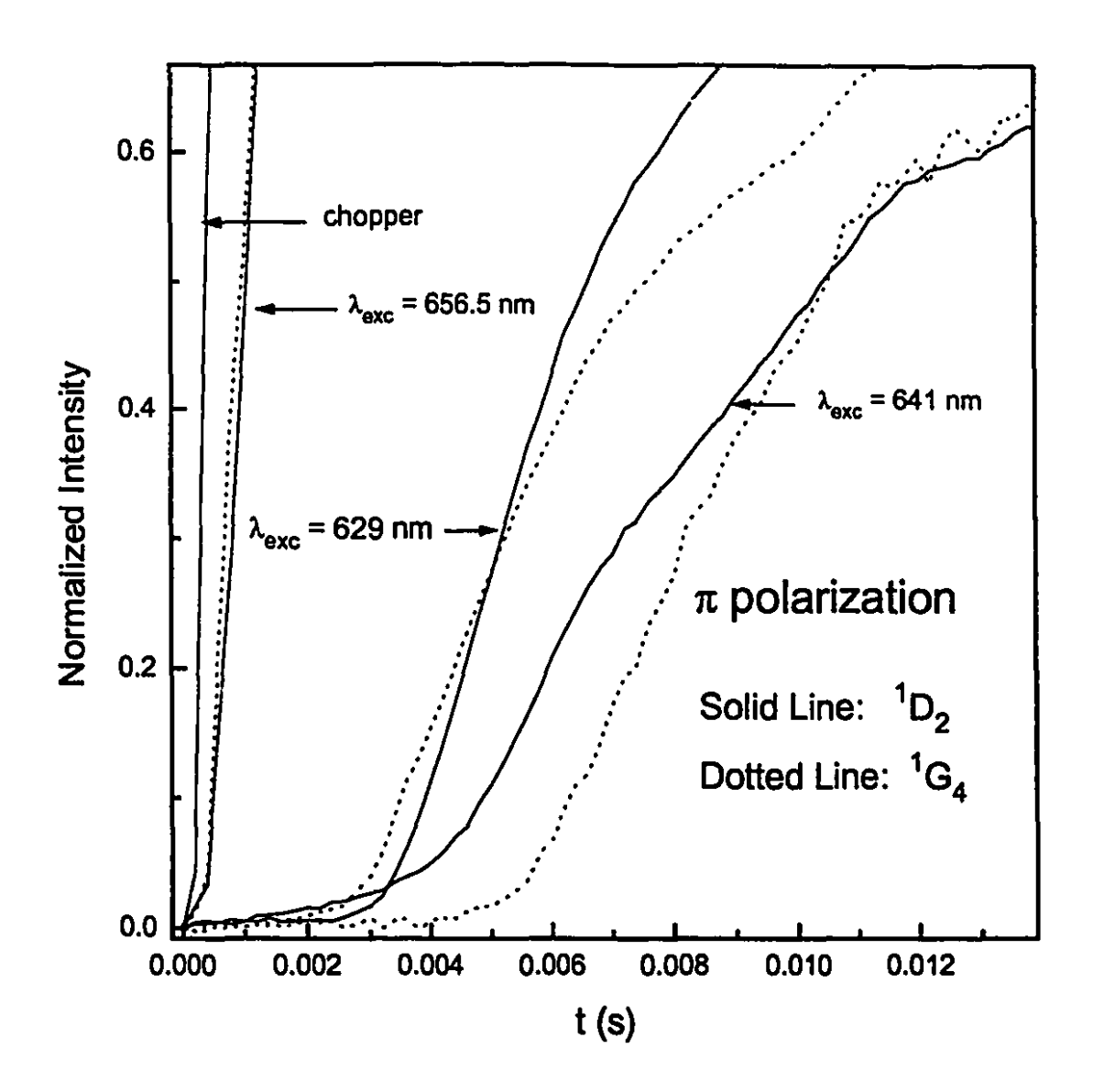
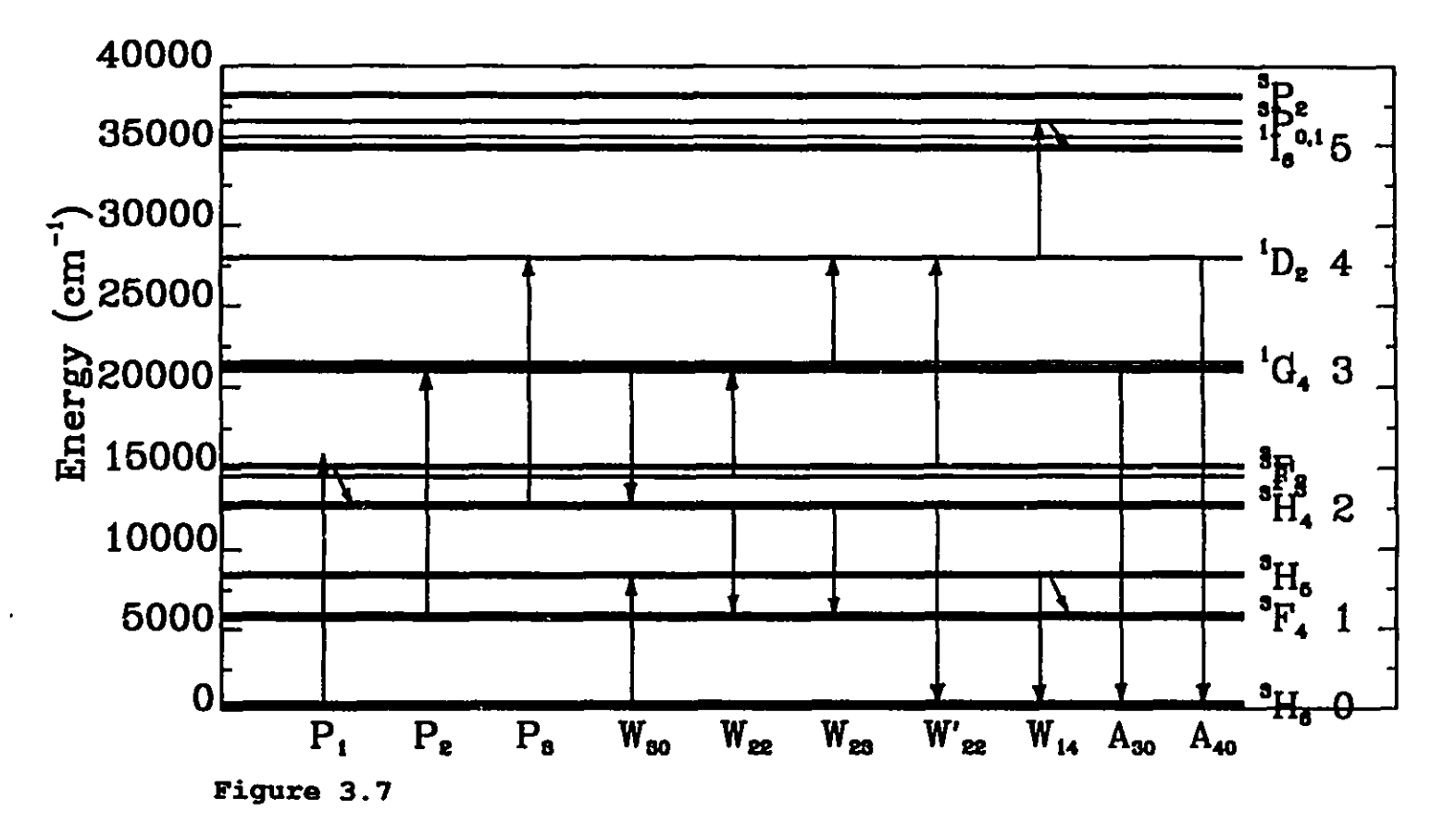


Figure 3.6 Rise time behaviour of the upconversion emission of Tm^3 :YLiF4 under 370 mW/3.42×10⁻⁵cm² and π polarization pump at different pump wavelengths.



Energy level scheme of Tm^{3+} showing the energy transfer the pump and the decay processes considered in the rate equations for the avalanche upconversion dynamics of Tm^{3+} :YLiF₄.

Table 3.4 Resonances for the three different pump wavelengths at each of the two different polarizations.

	σ	polariza	ation	π	polariza	ation
λ _{exc.} (nm)	627.0	646.0	656.0	629.0	641.0	656.5
ΔV ₁ (cm ⁻¹)	749	229	44	666	332	13
ΔV_2 (cm ⁻¹)	3	166	351	30	67	412
ΔV ₃ (Cm ⁻¹)	622	102	83	550	253	36

steps for the different wavelengths and polarizations.

At the longest wavelengths (656.0 nm for σ polarization and 656.5 nm for π polarization) the first pump is close to resonance. The rise of the upconversion follows the opening of the chopper, as would be expected for upconversion via direct excited state absorption. At intermediate wavelengths (ca. 646.0 nm for σ polarization and 641.0 nm pump for π polarization) the upconversion dynamics are different for the 1D_2 and 1G_4 emissions, and for the two polarizations. In π polarization (P₁ and P₃ are not resonant but P₂ is) and the 1G_4 emission begins only after an initial delay of over 6 ms, while the 1D_2 emission rises very gradually at first, but changes to a steeper slope after about 4 ms. In σ polarization (P₁, P₂ and P₃ all are non resonant) the rise of the 1G_4 emission is essentially the same as it is in π polarization, while the rise of the 1D_2 emission shows no

initial delay or change in slope. At the shortest wavelength (ca. 627 nm for σ polarization and 629.0 nm pump for π polarization) P_1 is far from resonance while but P_2 is close to resonance, and in this instance the rise of the upconversion has the longest delay. This case represents the conditions of typical avalanche upconversion.

We examined the details of the pump power dependence of the ${}^{1}G_{4}$ (487 nm) emission intensity at 12 K under 627 nm σ polarized pumping (from 30 mw/3.42×10⁻⁵cm² to 270 mw/3.42×10⁻⁵cm²). These are expected to be typical avalanche upconversion conditions, and the results shown in Figure 3.8 confirm this, exhibiting a threshold at ca. 125 mW/3.42×10⁻⁵cm². We also examined the power dependence of the dynamic behaviour under the same conditions, and these results are shown in Figure 3.9. Below threshold (at 30 mW/3.42×10⁻⁵cm²) no delay is seen. Above threshold the initial delay at first increases with increasing pump power, and then decreases again at the highest powers (above 220 mW/3.42×10⁻⁵cm²).

Figure 3.7 also shows the decay and energy transfer processes which we include in treating the avalanche upconversion dynamics of Tm^{3+} :YLiF₄. In the course of fitting the experimental data, we examined all the energetically possible energy transfer processes, and eliminated those which had no noticeable effect on the quality of the fit to the experimental data. To simplify the rate equations as much as possible, we combine the 3F_2 ; 3F_3 and 3H_4 levels into a single

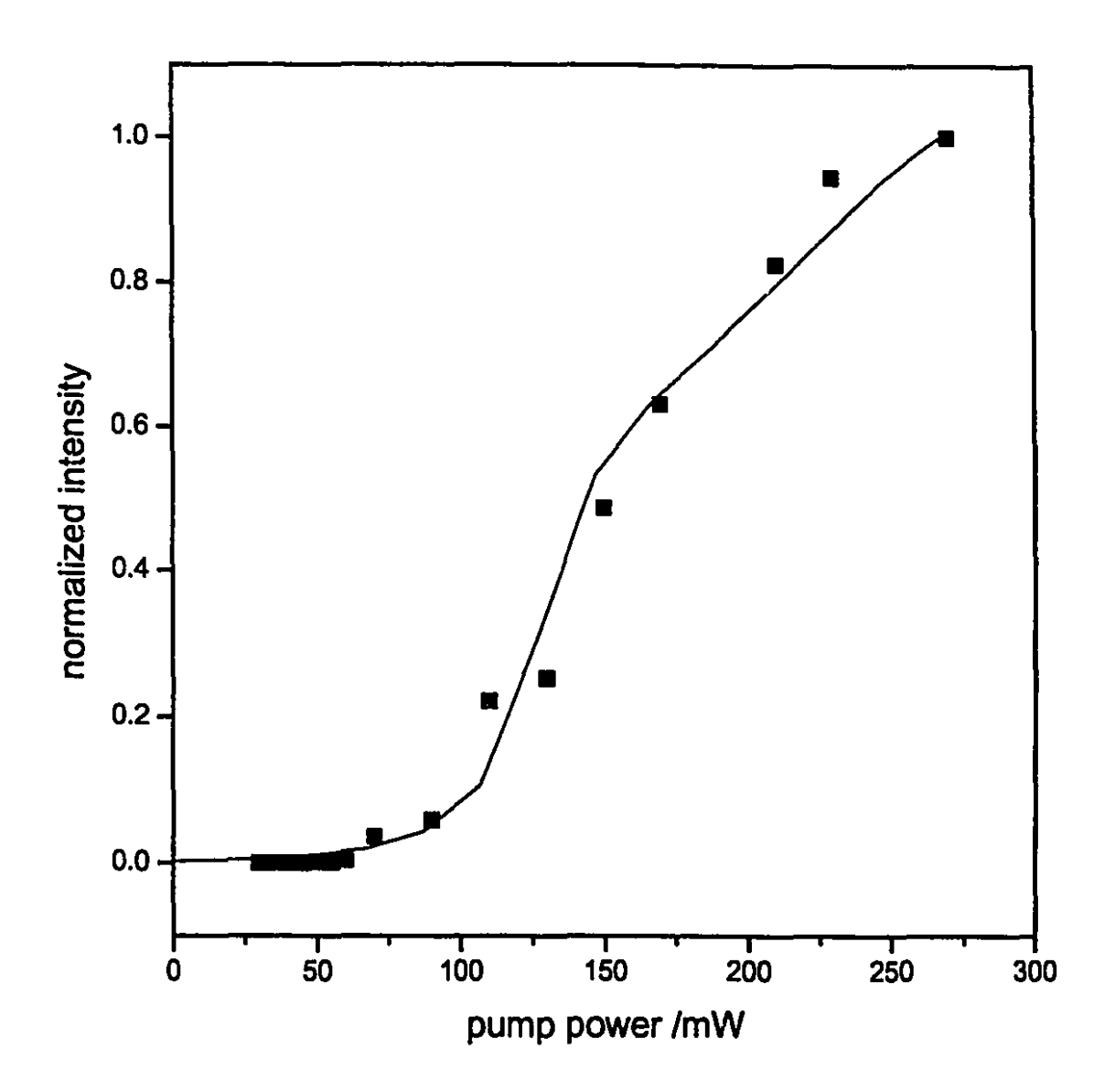


Figure 3.8

Dependence of the 487 nm upconversion emission intensity of Tm^{3^*} :YLiF₄ on 627 nm σ polarization laser power at 12 K. Square points: experimental points, solid line: fitted using the steady solutions of Equations (3.4).

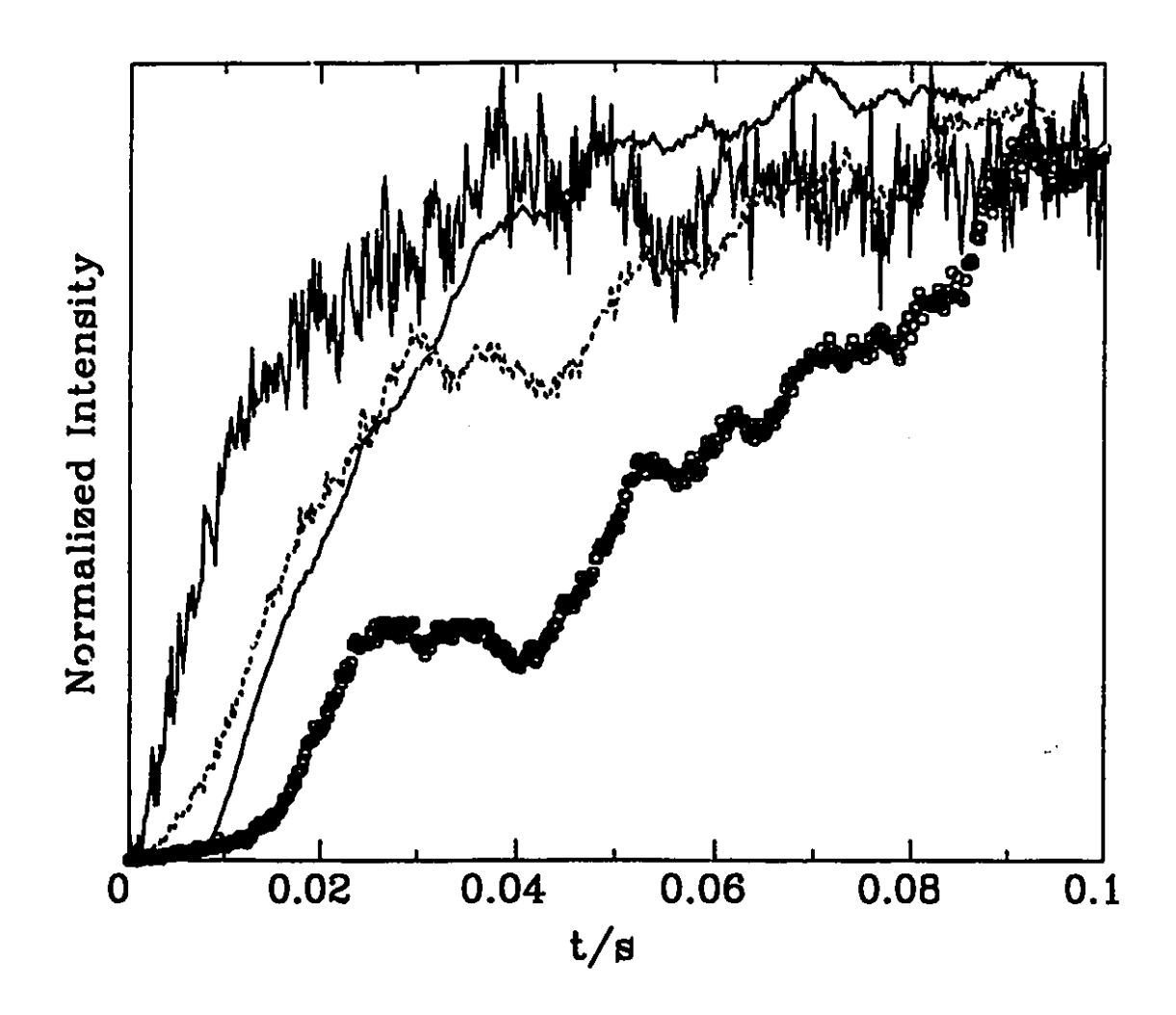


Figure 3.9

Dependence of the 487 nm upconversion rise time on 627 nm σ polarization laser power at 12 K. (left solid) 30 mW/3.42×10⁻⁵cm², (dashed) 160 mW/3.42×10⁻⁵cm², (dotted) 220 mw/3.42×10⁻⁵cm², and (right solid) 370 mW/3.42×10⁻⁵cm².

level, and do the same with 3H_5 and 3F_4 . We then obtain the following set of coupled rate equations:

$$\begin{split} \dot{n}(0) &= -P_1 \left[n(0) - n(2) \right] \\ &+ A_{50} n_5 + A_{40} n(4) + A_{30} n(3) + A_{20} n(2) + A_{10} n(1) \\ &+ W'_{22} n^2(2) + W_{14} n(1) n(4) - W_{30} n(3) n(0) \\ \dot{n}(1) &= -P_2 \left[n(1) - n(3) \right] \\ &+ A_{51} n(5) + A_{41} n(4) + A_{31} n(3) + A_{21} n(2) - A_{10} n(1) \\ &+ W_{22} n^2(2) + W_{23} n(2) n(3) - W_{14} n(1) n(4) \\ &+ W_{30} n(3) n(0) \\ \dot{n}(2) &= P_1 \left[n(0) - n(2) \right] - P_3 \left[n(2) - n(4) \right] \\ &+ A_{52} n(5) + A_{42} n(4) + A_{32} n(3) - A_{2} n(2) \\ &- 2 \left[W_{22} + W'_{22} \right] n^2(2) - W_{23} n(2) n(3) \\ &+ W_{30} n(3) n(0) \\ \dot{n}(3) &= P_2 \left[n(1) - n(3) \right] \\ &+ A_{53} n(5) + A_{43} n(4) - A_{3} n(3) \\ &+ W_{22} n^2(2) - W_{23} n(2) n(3) - W_{30} n(3) n(0) \\ \dot{n}(4) &= P_3 \left[n(2) - n(4) \right] + A_{54} n(5) - A_4 n(4) \\ &+ W'_{22} n^2(2) + W_{23} n(2) n(3) - W_{14} n(1) n(4) \\ \dot{n}(5) &= -A_5 n(5) + W_{14} n(1) n(4) \end{split}$$

where W_{ij} are two-body energy transfer parameters, $P_1=\sigma_1 I$, $P_2=\sigma_2 I$ and $P_3=\sigma_3 I$ are pump rates, σ_1 ; σ_2 ; and σ_3 are absorption cross sections, I is the intensity of the pump laser, and λ_{ij} are the radiative decay rates. By dividing the total Tm^{3+} concentration n_{Tm} (1.98×10²⁰ cm⁻³) on both sides of equations (3.3), we obtain the following normalized rate equations:

```
\rho(0) = -P_1[\rho(0) - \rho(2)]
        +A_{50}\rho_5+A_{40}\rho (4) +A_{30}\rho (3) +A_{20}\rho (2) +A_{10}\rho (1)
        +K'_{22}\rho^{2}(2)+K_{14}\rho(1)\rho(4)-K_{30}\rho(3)\rho(0)
\dot{\rho}(1) = -P_2[\rho(1) - \rho(3)]
        +A_{51}\rho(5)+A_{41}\rho(4)+A_{31}\rho(3)+A_{21}\rho(2)-A_{10}\rho(1)
        +K_{22}\rho^{2}(2)+K_{23}\rho(2)\rho(3)-K_{14}\rho(1)\rho(4)
        +K_{30}p(3)p(0)
\dot{\rho}(2) = P_1[\rho(0) - \rho(2)] - P_3[\rho(2) - \rho(4)]
        +A_{52}\rho(5)+A_{42}\rho(4)+A_{32}\rho(3)-A_{2}\rho(2)
                                                                                        (3.4)
       -2[K_{22}+K'_{22}]\rho^2(2)-K_{23}\rho(2)\rho(3)
        +K_{30}\rho(3)\rho(0)
\dot{\rho}(3) = P_2[\rho(1) - \rho(3)]
        +A_{53}\rho(5)+A_{43}\rho(4)-A_{3}\rho(3)
        +K_{22}\rho^{2}(2)-K_{23}\rho(2)\rho(3)-K_{30}\rho(3)\rho(0)
\phi(4) = P_3[\rho(2) - \rho(4)] + A_{54}\rho(5) - A_4\rho(4)
        +K'_{22}\rho^{2}(2)+K_{23}\rho(2)\rho(3)-K_{14}\rho(1)\rho(4)
\dot{\rho}(5) = -A_5 \rho(5) + K_{14} \rho(1) \rho(4)
```

where $\rho(i) = n(i) / n_{Tm}$ are normalized concentrations and $K_{ij} = W_{ij} n_{Tm}$. Using equation (3.4) and the IMSL library routine "DEVERK" program, the experimental data were fitted. In the fitting most of the radiative decay rates were fixed at the calculated values which are listed in Table 3.5. The parameters K_{i+} and pump rates $P_{1,2,3}$ were used as adjustable parameters to obtain the best fit for the low pump power (30 mw/3.42×10⁻⁵cm²) data (with no initial delay), which is shown in Figure 3.10. The values of the parameters found from this procedure are listed in Table 3.6 (the transfer parameters W₁, were obtained by deviding K_{ij} with the Tm^{3+} concentration in $Tm^{3+}:YLiF_4$, n_{Tm}), where they may be compared with values calculated from Judd-Ofelt theory. For a resonant pump, the absorption crosssection may be found from (1.55) with the refractive index n=1.79[3] and the line width $\Delta v=5$ cm⁻¹[8]. The transfer rates may found from (1.42) with values of Ω_{λ} from Table 1.8

Table 3.5 Fixed radiative decay rates in fitting the time dependent upconversion 487 nm emission experimental data of Tm³⁻:YLiF₄ under 30 mW/3.42×10⁻⁵cm² pump

A ₅₀ (s ⁻¹)	492
A ₅₁ (s ⁻¹)	3265
A ₅₂ (s ⁻¹)	1267
A ₅₃ (s ⁻¹)	876
A ₅₄ (s ⁻¹)	30
A ₄₀ (s ⁻¹)	3388
A_{41} (s ⁻¹)	6614
A ₄₂ (s ⁻¹)	1495
A ₄₃ (s ⁻¹)	75
A ₃₀ (s ⁻¹)	399
A ₃₁ (s ⁻¹)	227
A ₃₂ (s ⁻¹)	114
A ₂₀ (s ⁻¹)	434
A ₂₁ (s ⁻¹)	49

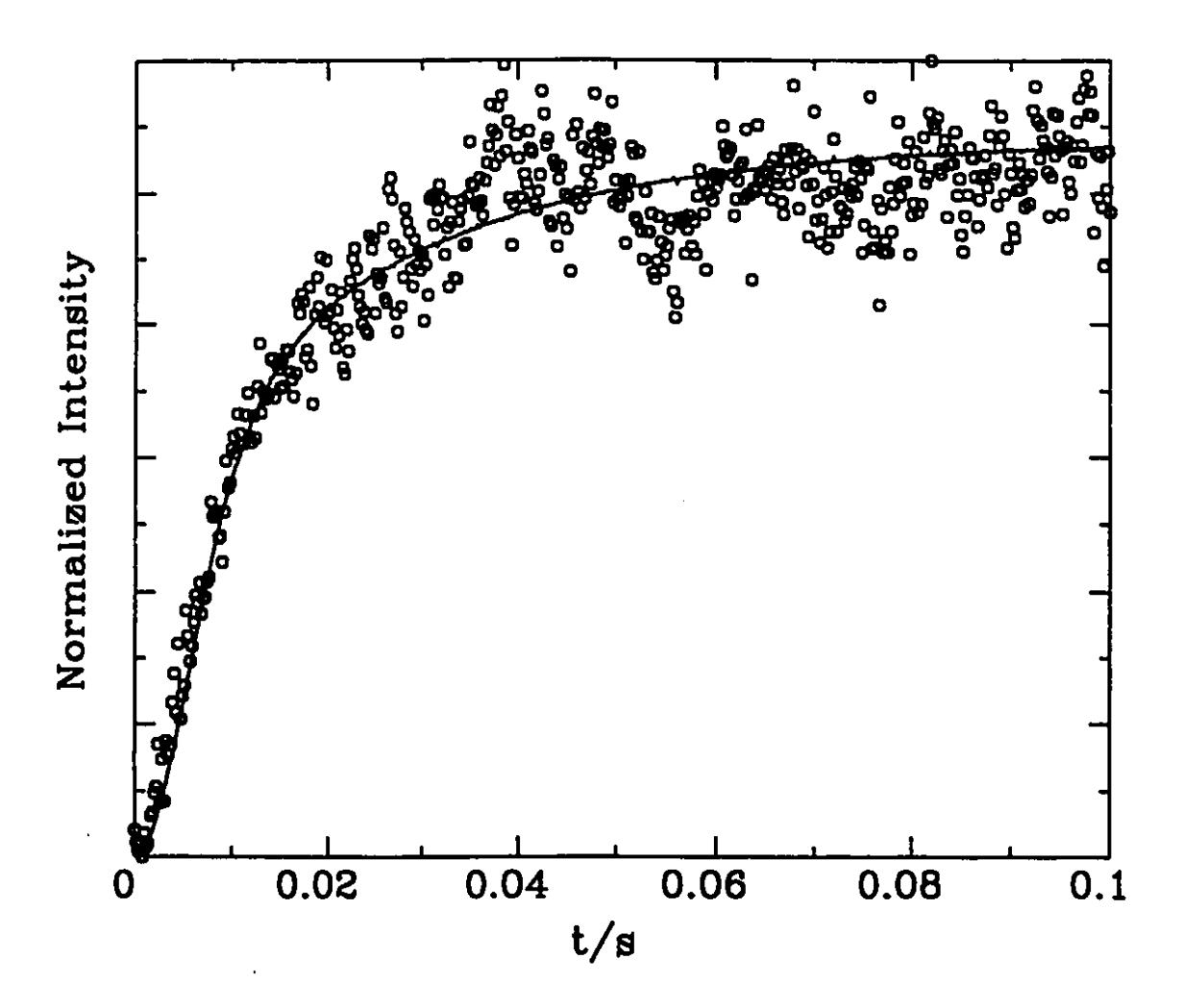


Figure 3.10

Time dependence of the upconversion emission of $Tm^3 cdot YLiF_4$ at 487 nm ($^3H_6 \leftarrow ^1G_4$) and 12 K under 30 mw/3.42×10⁻⁵cm² 627 nm and σ polarization pump. Open circles: experimental points, solid lines: calculated from Equations (3.4) using the parameter values given by Table 3.5 and 3.6.

(STD deviation=0.044061)

Table 3.6 Parameters obtained from the fitting of the time dependent upconversion 487 nm emission experimental data of Tm^3 :YLiF₄ under 30 mW/3.42×10⁻⁵cm² pump compared with the calculated values.

 $(n_{\text{m}}=1.98\times10^{20} \text{ cm}^{-3}, n_{\text{y}}=1.39\times10^{22} \text{ cm}^{-3}, a_{\text{y}}=5.16 \text{ Å})$

(112-1:30/10 Cm / 11/21:35/10 Cm / 41/-3:10 14/			
	calculated	fitted	
A ₁₀ (s ⁻¹)	89	50	
σ_1 (cm ²)	1.54×10 ⁻²⁰	$(7.71\pm0.15)\times10^{-24}$	
σ_2 (cm ²)	4.04×10 ⁻²¹	(2.00±0.06)×10 ⁻²¹	
σ_3 (cm ²)	4.25×10 ⁻²¹	$(1.60\pm1.02)\times10^{-25}$	
$v_{A}-v_{B} = 11 \text{ (cm}^{-1})$	$C_{30}(s^{-1}cm^6) = 1.70 \times 10^{-34}$	$K_{30}(s^{-1}) = (3.12\pm0.62) \times 10^{5}$	
$W_{30} (s^{-1}cm^3)$	5.18×10 ⁻¹²	$(1.58\pm0.32)\times10^{-15}$	
$V_A - V_B = 1 \text{ (cm}^{-1})$ $W_{22} \text{ (s}^{-1} \text{cm}^3)$	$C_{22}(s^{-1}cm^6) = 9.38 \times 10^{-35} \\ 2.86 \times 10^{-12}$	$K_{22}(s^{-1}) = (1.40\pm0.03)\times10^{5} (7.07\pm0.15)\times10^{-16}$	
		 	
$V_{A}-V_{B} = 12 \text{ (cm}^{-1})$	$C_{23}(s^{-1}cm^6) = 1.60 \times 10^{-34}$	$K_{23}(s^{-1}) = (6.81 \pm 4.43) \times 10^{5}$	
$W_{23} (s^{-1}cm^3)$	4.88×10 ⁻¹²	$(3.45\pm2.24)\times10^{-15}$	
$v_{A}-v_{B} = 268 \text{ (cm}^{-1})$	$C'_{22}(s^{-1}cm^6) = 3.76 \times 10^{-34}$	$K'_{22}(s^{-1}) = 0$	
$W'_{22}(s^{-1}cm^3)$	1.15×10 ⁻¹¹	0	
$v_{A}-v_{B} = 15 (cm^{-1})$	$C_{14} (s^{-1}cm^{6}) = 3.91 \times 10^{-35}$	$K_{14}(s^{-1}) = 0$	
$W_{14} (s^{-1}cm^3)$	1.19×10 ⁻¹²	0	

 $(\Omega_2=2.43\times10^{-20}~{\rm cm}^2,~\Omega_c=1.08\times10^{-20}~{\rm cm}^2$ and $\Omega_c=0.67\times10^{-20}~{\rm cm}^2)$ and the values of $<J^{\dagger}U^{(\lambda)}$ $J^{\prime}>^2$ from Table 1.9. Considering only the nearest neighbour transfer the distance R in Equation (1.42) was treated as the lattice distance a (obtained from the Yttrium concentration in YLiF₄ which is given in Table 1.2). The overlap integral S can be estimated from (1.32) and (1.33) where, we take the line width to be $\Delta V=10^{-3}{\rm cm}^{-1}$ [23], and assume perfectly resonant energy transfer $(V_A-V_B=0)$ with Lorentzian lineshape. The transfer parameter W_{11} is then obtained by (1.51) (by dividing the transfer rate by the total concentration of the Yttrium in YLiF₄). The calculated values of the absorption cross sections and the transfer parameters are given in Table 3.6, along with the values used for fitting the experimental data.

The fitted energy transfer parameters agree with the calculated values reasonably well. As expected, the calculated values, based on exact resonance, are larger than those found experimentally. In the fitting it was found that the transfer parameters W'_{22} and W_{14} had little or no effect on the solutions. This may be the result of the lack of resonance at low temperature (as can be seen from Table 3.6). Reasonable agreement is also found for the fitted and calculated values of the absorption cross-section, but only for the second (resonant) pump. The fitted values of both σ_1 and σ_3 are much smaller than the calculated ones, which is consistent with the fact that the pump is only in the wings of these absorptions

as shown by Table 3.4.

The coupled rate equations (3.4) were solved different pump powers from $30 \text{ mW}/3.42\times10^{-5}\text{cm}^2$ to 340 $mW/3.42\times10^{-5}cm^2$, using the same parameters found by fitting the data at 30 mW/3.42×10 $^{-5}$ cm². We note that at powers above 30 mW/3.42×10⁻⁵cm² the calculated rise of the upconversion emission did not follow the shape of the experimental data well, but for the calculated power dependence we are primarily interested in the steady state populations (solutions at long The steady state solutions for $\rho(3)$, the ${}^{1}G_{4}$ level, obtained in this way display the power dependence of the upconversion emission intensity. This is shown as the solid line in Figure 3.8, which also shows the measured power dependence of the intensity. The calculated curve had to be shifted (on the power axis) by -60 mW/3.42×10⁻⁵cm² to bring it into accord with the data points, but the shape found can be seen to be correct. The shift along the energy axis may simply reflect a systematic error in the measurement of the beam waist.

It is interesting to examine the qualitative behaviour of the rise of the upconversion emission with increasing pump power. In Figure 3.9, we see that at the lowest pump power (30 mW/3.42×10⁻⁵cm²) there is essentially no initial delay. At higher pump power (160 mW/3.42×10⁻⁵cm²) an initial delay becomes evident. This delay increases with increasing pump power to 220 mW/3.42×10⁻⁵cm², but decreases again at higher

powers (370 mW/3.42×10⁻⁵cm²). Figure 3.11 shows calculated solutions to the coupled rate equations (3.4) for the corresponding pump rates (all parameters fixed at the 30 mW/3.42×10⁻⁵cm² value except the pump rate), and the same qualitative trend as shown in Figure 3.9 is again observed, although the calculated curves do not fit the experimental ones at powers above 30 mW/3.42×10⁻⁵cm².

The impossibility of simulating the experimental risetime behaviour (especially under high pump powers) within the framework of a second order kinetic model led us to consider alternatives. The most successful, in terms of fitting the experimental data, was the inclusion of fourth order kinetic terms in the coupled rate equations[67]. To avoid a multiplication of fitting parameters, we simply replaced the second order energy transfer terms with the equivalent fourth Inclusion of third order terms would have to order terms. involve different donor-acceptor combinations than second order terms, to ensure energy conservation, which is not true of fourth order interactions. By simply changing the energy transfer terms in Equations (3.3) from: $W_{DA}n_Dn_A$ to: $W_{DDAA}n_D^2n_A^2$ we obtain the following rate equations:

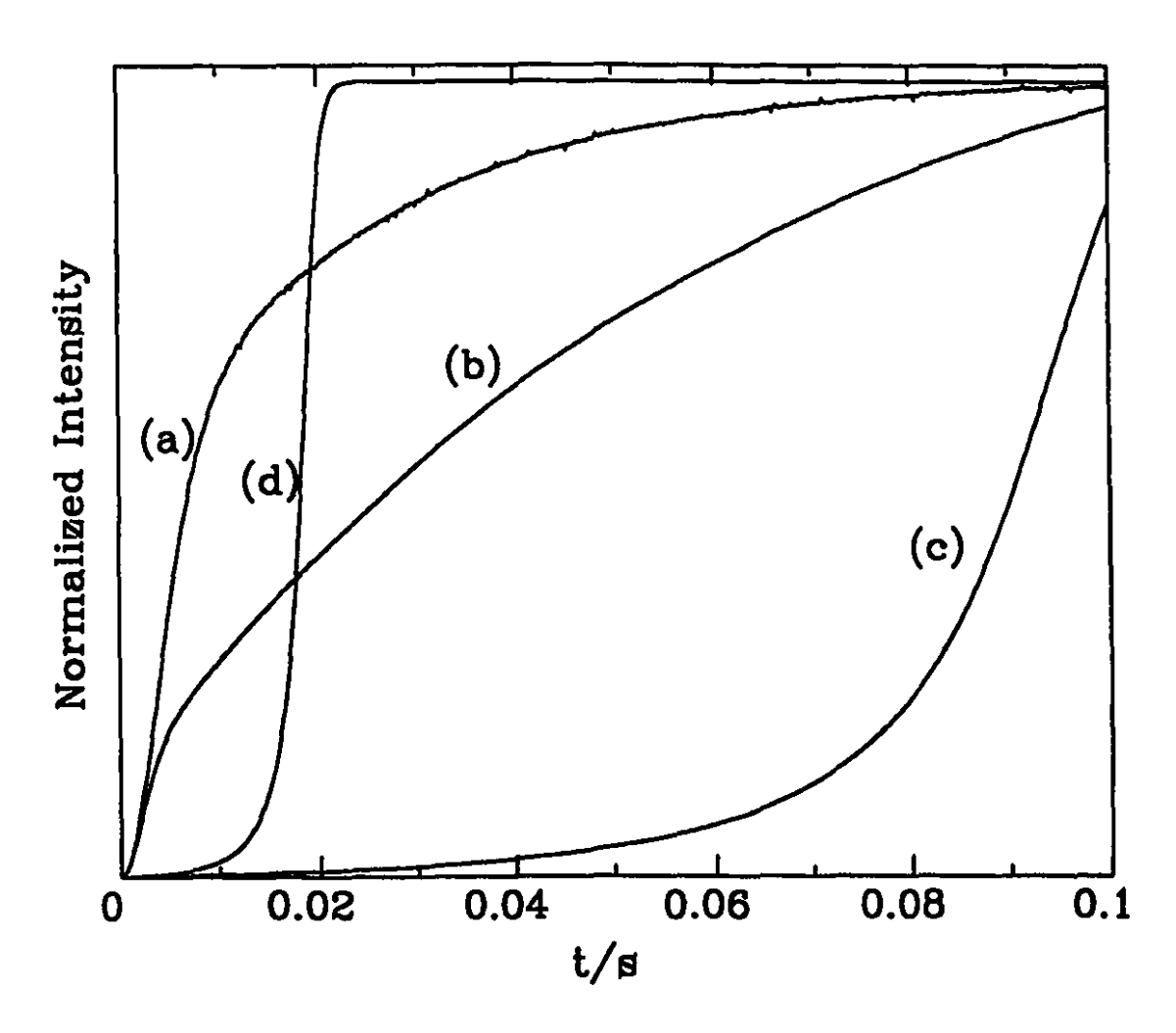


Figure 3.11

Simulations of the dependence of the 487 nm upconversion rise time of Tm^{3+} :YLiF₄ on 627 nm σ polarization laser power at 12 K with the solutions of Equation (3.4) by changing only the pump power. (a) 30 mW/3.42×10⁻⁵cm², (b) 160 mW/3.42×10⁻⁵cm², (c) 220 mw/3.42×10⁻⁵cm², and (d) 370 mW/3.42×10⁻⁵cm².

```
\dot{n}(0) = -P_1[n(0) - n(2)]
      +A_{50}n(5)+A_{40}n(4)+A_{30}n(3)+A_{20}n(2)+A_{10}n(1)
      +2W_{2222}^{\prime}n^{4}(2) +2W_{1144}n^{2}(1)n^{2}(4)
      -2W_{3300}n^2(3)n^2(0)
n(1) = -P_2[n(1) - n(3)]
      +A_{51}n(5) +A_{41}n(4) +A_{31}n(3) +A_{21}n(2) -A_{10}n(1)
      +2W_{2222}n^4(2) + 2W_{2233}n^2(2)n^2(3)
      -2W_{1144}n^2(1)n^2(4)+2W_{3300}n^2(3)n^2(0)
h(2) = P_1[n(0) - n(2)] - P_3[n(2) - n(4)]
      +A_{52}n(5)+A_{42}n(4)+A_{32}n(3)-A_{2}n(2)
                                                                         (3.5)
      -4 [W_{2222} + W'_{2222}] n^4 (2) -2 W_{2233} n^2 (2) n^2 (3)
      +4W_{3300}n^2(3)n^2(0)
\dot{n}(3) = P_2[n(1) - n(3)]
      +A_{53}n(5)+A_{43}n(4)-A_{3}n(3)
      +2W_{2222}n^4(2)-2W_{2233}n^2(2)n^2(3)
      -2W_{3300}n^2(3)n^2(0)
\dot{n}(4) = P_3[n(2) - n(4)] + A_{54}n(5) - A_4n(4) + 2W'_{2222}n^4(2)
      +2W_{2233}n^2(2)n^2(3)-2W_{1144}n^2(1)n^2(4)
\dot{n}(5) = -A_{51}n(5) + 2W_{1144}n^2(1)n^2(4)
```

where W_{iijj} are fourth-order energy transfer parameters. By dividing the total Tm^{3+} concentration n_{Tm} (1.98×10²⁰ cm⁻³) on both sides of equations (3.5) we obtain the following normalized rate equations:

$$\begin{split} \dot{\rho}\left(0\right) &= -P_{1}\left[\rho\left(0\right) - \rho\left(2\right)\right] \\ &+ A_{50}\rho\left(5\right) + A_{40}\rho\left(4\right) + A_{30}\rho\left(3\right) + A_{20}\rho\left(2\right) + A_{10}\rho\left(1\right) \\ &+ 2K'_{2222}\rho^{4}\left(2\right) + 2K_{1144}\rho^{2}\left(1\right)\rho^{2}\left(4\right) \\ &- 2K_{3300}\rho^{2}\left(3\right)\rho^{2}\left(0\right) \\ \dot{\rho}\left(1\right) &= -P_{2}\left[\rho\left(1\right) - \rho\left(3\right)\right] \\ &+ A_{51}\rho\left(5\right) + A_{41}\rho\left(4\right) + A_{31}\rho\left(3\right) + A_{21}\rho\left(2\right) - A_{10}\rho\left(1\right) \\ &+ 2K_{2222}\rho^{4}\left(2\right) + 2K_{2233}\rho^{2}\left(2\right)\rho^{2}\left(3\right) \\ &- 2K_{1144}\rho^{2}\left(1\right)\rho^{2}\left(4\right) + 2K_{3300}\rho^{2}\left(3\right)\rho^{2}\left(0\right) \\ \dot{\rho}\left(2\right) &= P_{1}\left[\rho\left(0\right) - \rho\left(2\right)\right] - P_{3}\left[\rho\left(2\right) - \rho\left(4\right)\right] \\ &+ A_{52}\rho\left(5\right) + A_{42}\rho\left(4\right) + A_{32}\rho\left(3\right) - A_{2}\rho\left(2\right) \\ &- 4\left[K_{2222} + K'_{2222}\right]\rho^{4}\left(2\right) - 2K_{2233}\rho^{2}\left(2\right)\rho^{2}\left(3\right) \\ &+ 4K_{3300}\rho^{2}\left(3\right)\rho^{2}\left(0\right) \\ \dot{\rho}\left(3\right) &= P_{2}\left[\rho\left(1\right) - \rho\left(3\right)\right] \\ &+ A_{53}\rho\left(5\right) + A_{43}\rho\left(4\right) - A_{3}\rho\left(3\right) \\ &+ 2K_{2222}\rho^{4}\left(2\right) - 2K_{2233}\rho^{2}\left(2\right)\rho^{2}\left(3\right) \\ &- 2K_{3300}\rho^{2}\left(3\right)\rho^{2}\left(0\right) \\ \dot{\rho}\left(4\right) &= P_{3}\left[\rho\left(2\right) - \rho\left(4\right)\right] + A_{54}\rho\left(5\right) - A_{4}\rho\left(4\right) + 2K'_{2222}\rho^{4}\left(2\right) \\ &+ 2K_{2233}\rho^{2}\left(2\right)\rho^{2}\left(3\right) - 2K_{1144}\rho^{2}\left(1\right)\rho^{2}\left(4\right) \\ \dot{\rho}\left(5\right) &= -A_{51}\rho\left(5\right) + 2K_{1144}\rho^{2}\left(1\right)\rho^{2}\left(4\right) \end{split}$$

where $\rho(i)=n(i)/n_{Tm}$ are normalized concentrations and $K_{iijj}=W_{iijj}n_{Tm}^3$. Using equation (3.6) to fit the experimental data we fix the radiative decay rates (except A_{20} , A_{21} and A_{10}) at their calculated values and then vary the pump rates and parameters K_{iijj} to obtain the best fit for both the 1G_4 and 1D_2 emissions simultaneously. These are shown in Figures 3.12, 3.13, 3.14, and 3.15 for the low temperature (12 k) data.

The normalized coupled rate equations (3.6) also yield good fits for the room temperature data, which also could not be simulated using second order rate equations. These are shown in Figures 3.16 and 3.17.

The radiative decay rates fixed in the fitting are listed in Table 3.7. The other parameters found in the fitting for both the low temperature and the room temperature data for

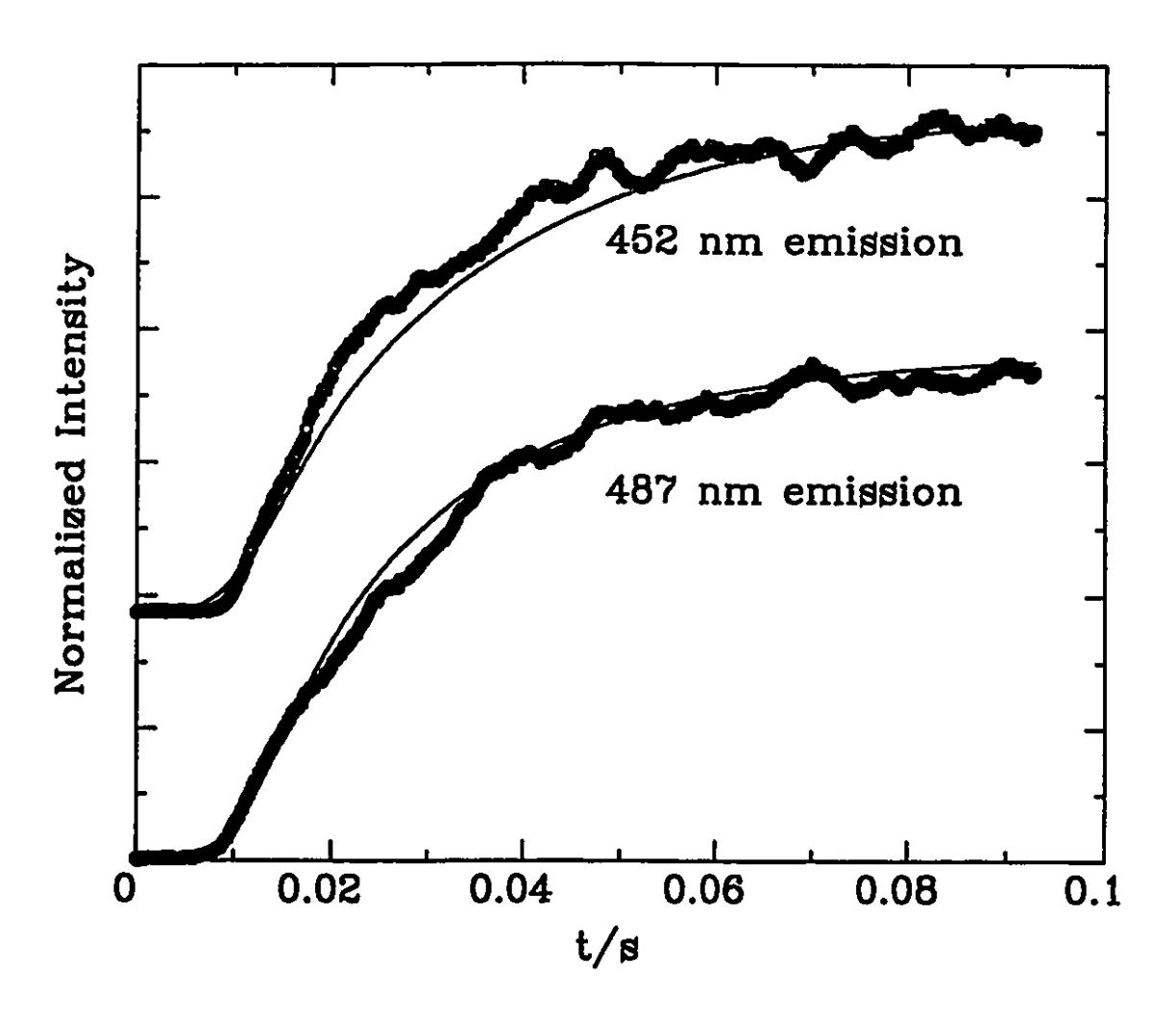


Figure 3.12

Time dependence of the upconversion emission of Tm^{3+} :YLiF₄ at 487 nm ($^3H_6 \leftarrow ^1G_4$) and 452 nm ($^3F_4 \leftarrow ^1D_2$) at 12 K under 370 mw/3.42×10⁻⁵cm² σ polarization 627 nm pump. Open circles: experimental points, solid lines: calculated from Equations (3.6) with parameter values given by Table 3.7 and 3.8.

(STD deviation=0.043207)

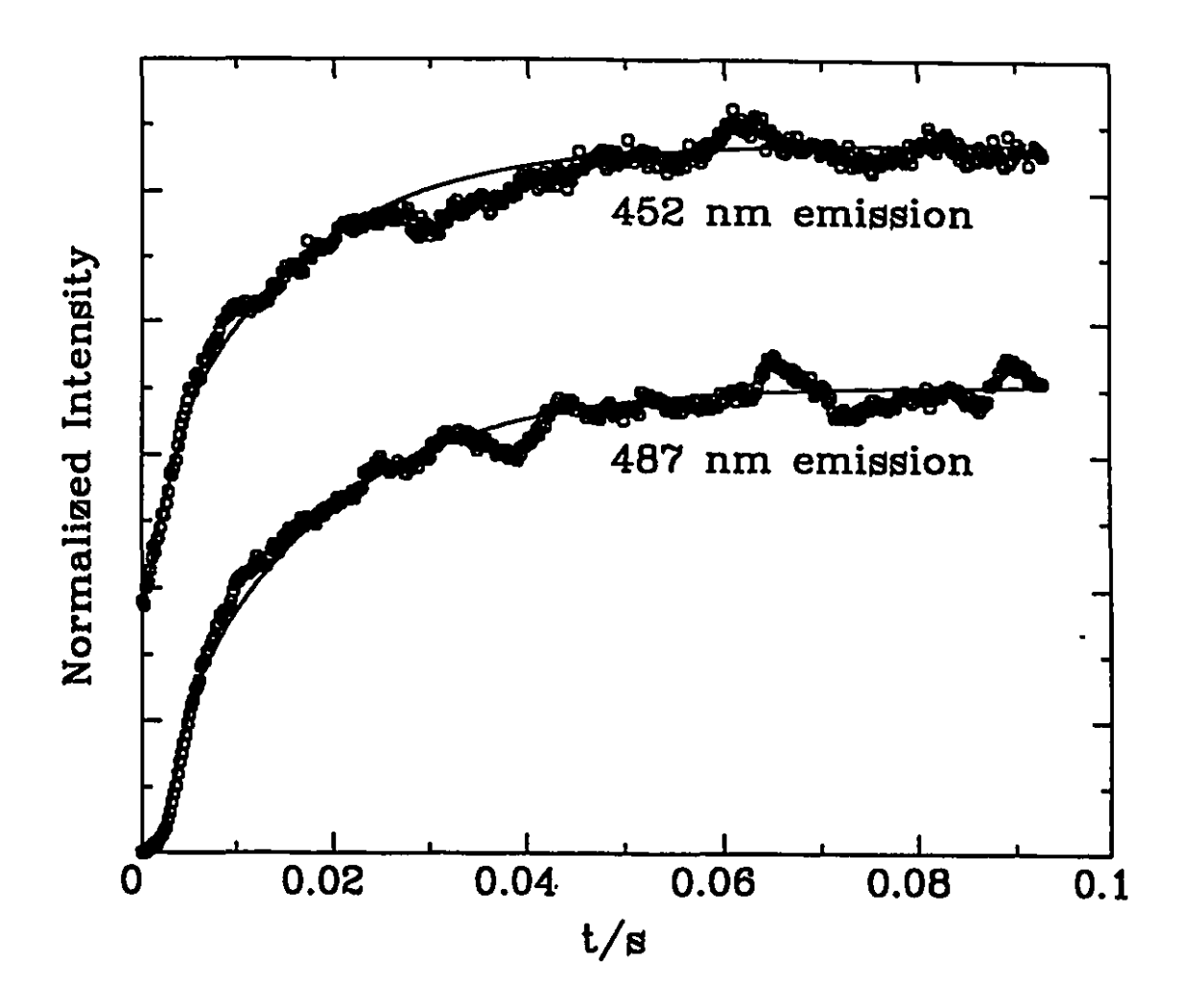


Figure 3.13

Time dependence of the upconversion emission of Tm3+:YLiF, at 487 nm (${}^{3}H_{6} \leftarrow {}^{1}G_{4}$) and 452 nm (${}^{3}F_{4} \leftarrow {}^{1}D_{2}$) at 12 K under 370 mw/3.42×10⁻⁵cm² σ polarization 646 nm pump. Open circles: experimental points, solid lines: calculated from Equations (3.6) with parameter values given by Table 3.7 and 3.8.

(STD deviation=0.034778)

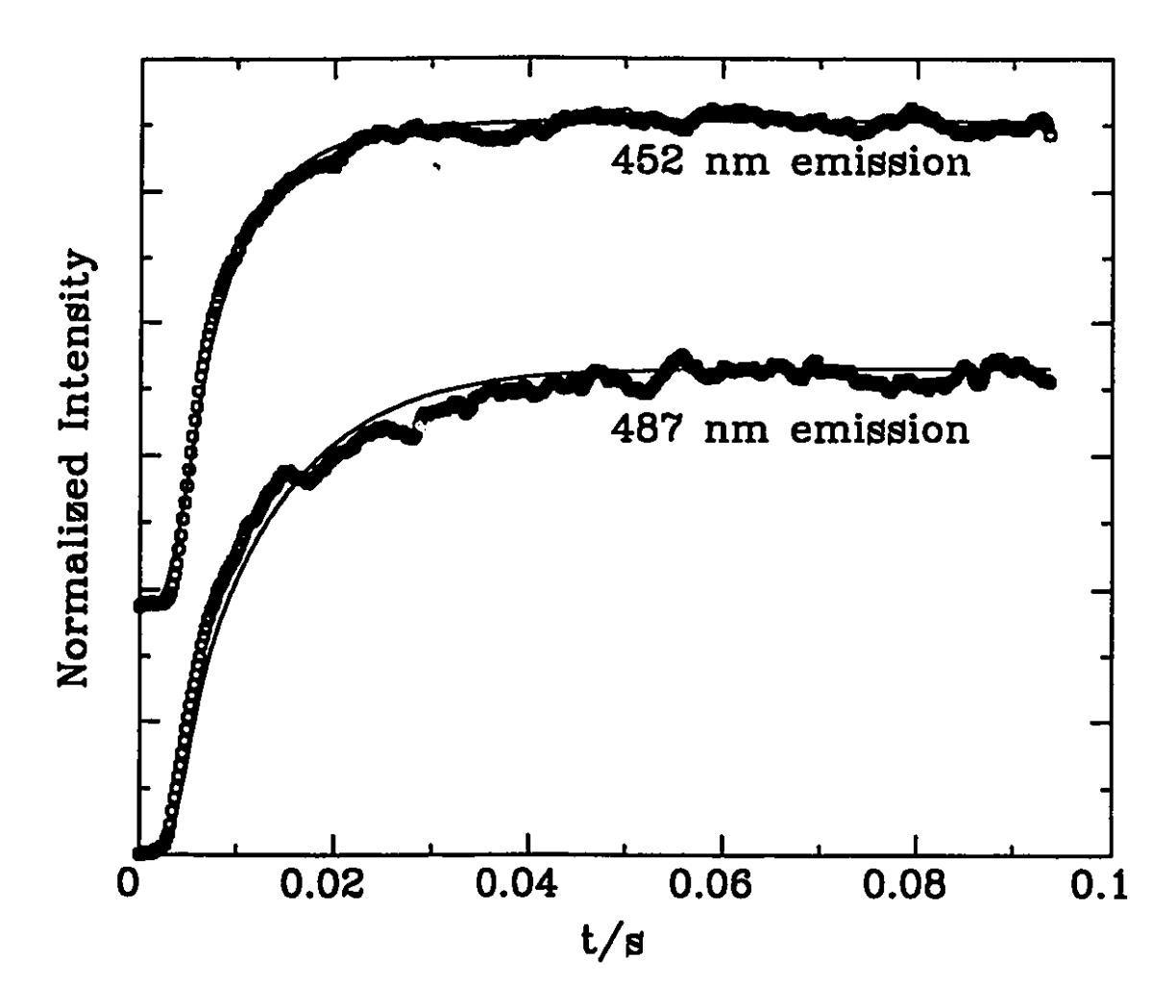


Figure 3.14

Time dependence of the upconversion emission of Tm^{3+} :YLiF₄ at 487 nm ($^3H_6 \leftarrow ^1G_4$) and 452 nm ($^3F_4 \leftarrow ^1D_2$) at 12 K under 370 mw/3.42×10⁻⁵cm² π polarization 629 nm pump. Open circles: experimental points, solid lines: calculated from Equations (3.6) with parameter values given by Table 3.7 and 3.9. (STD deviation=0.026423)

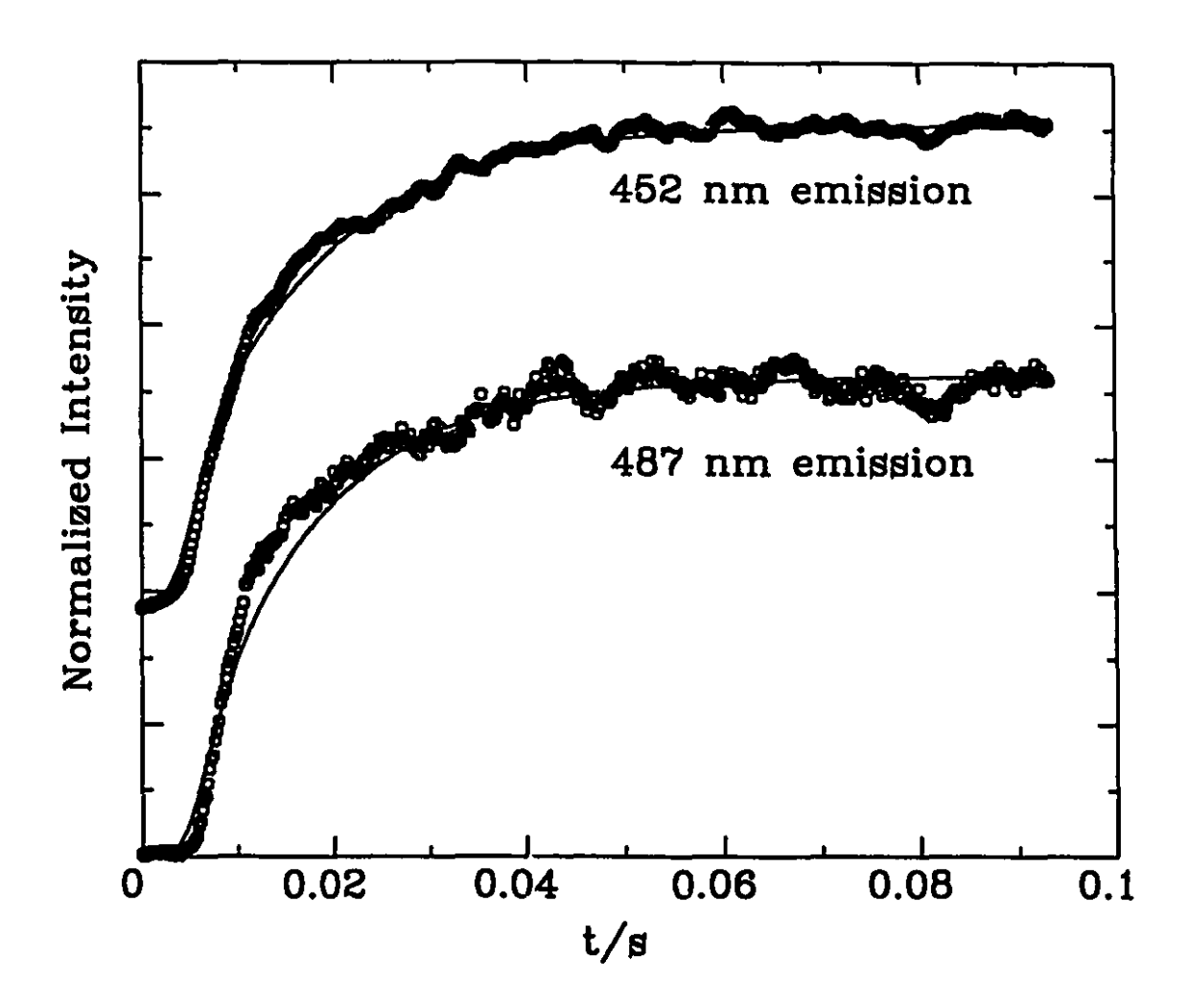


Figure 3.15

Time dependence of the upconversion emission of Tm^{3+} :YLiF₄ at 487 nm ($^3H_6 \leftarrow {}^1G_4$) and 452 nm ($^3F_4 \leftarrow {}^1D_2$) at 12 K under 370 mw/3.42×10⁻⁵cm² π polarization 641 nm pump. Open circles: experimental points, solid lines: calculated from Equations (3.6) with parameter values given by Table 3.7 and 3.9. (STD deviation=0.029645)

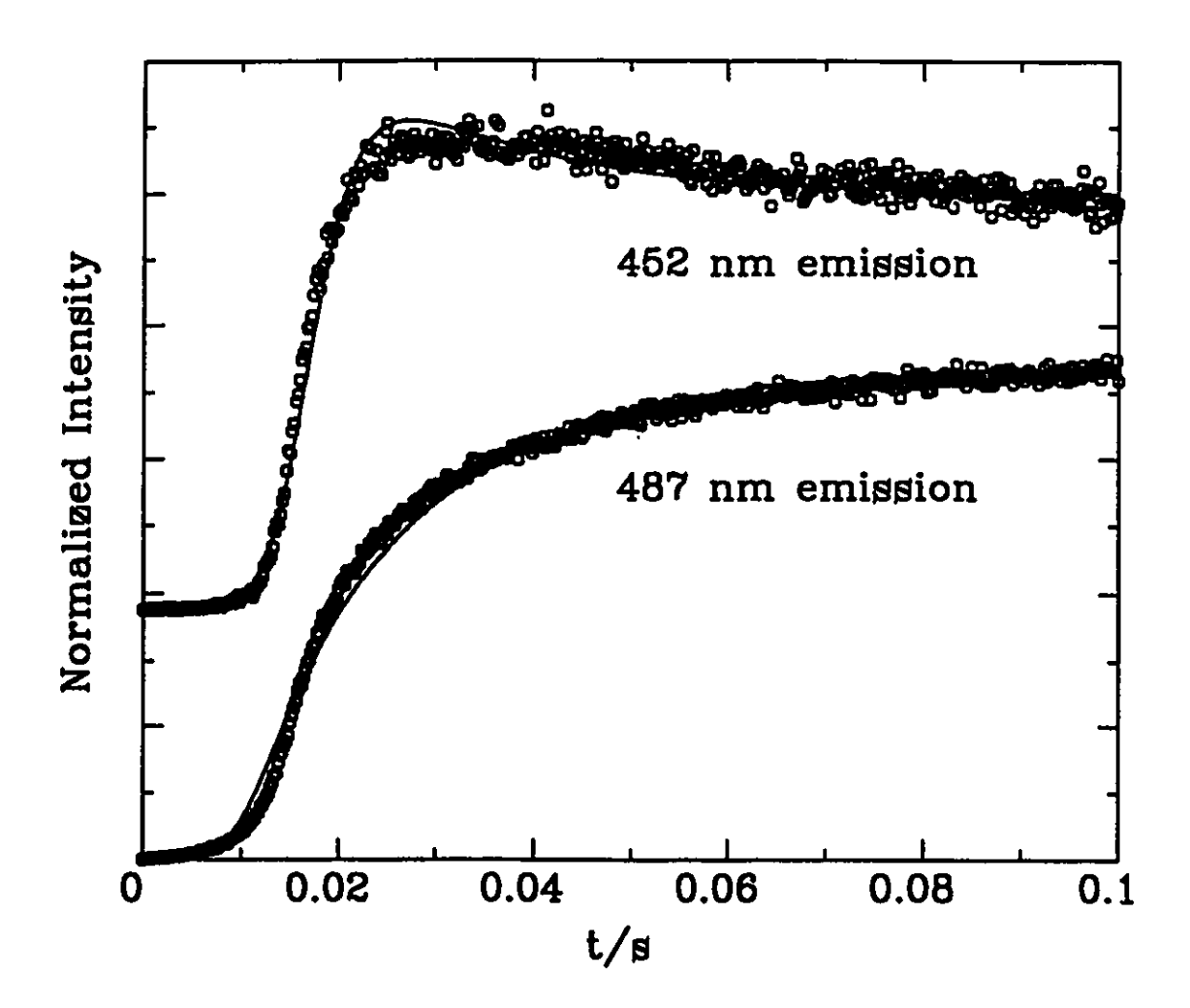


Figure 3.16

Time dependence of the upconversion emission of Tm^{3+} :YLiF₄ at 487 nm ($^3H_6 \leftarrow ^1G_4$) and 452 nm ($^3F_4 \leftarrow ^1D_2$) at 300 K under 370 mw/3.42×10⁻⁵cm² σ polarization 650 nm pump. Open circles: experimental points, solid lines: calculated from Equations (3.6) with the parameter values in Table 3.7 and 3.8.

(STD deviation=0.032999)

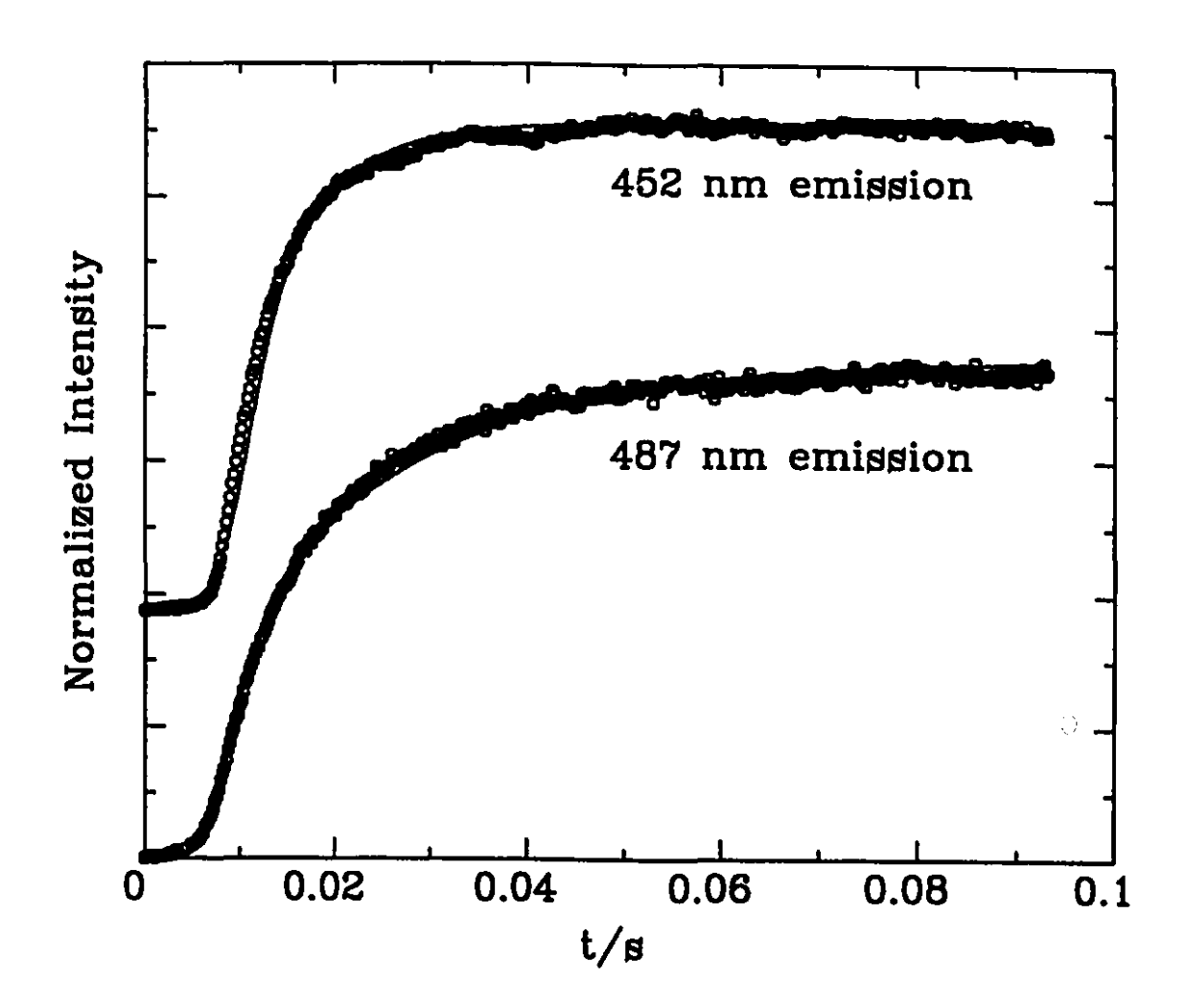


Figure 3.17

Time dependence of the upconversion emission of Tm^{3+} :YLiF₄ at 487 nm ($^3H_6 \leftarrow ^1G_4$) and 452 nm ($^3F_4 \leftarrow ^1D_2$) at **300 K** under 370 mw/3.42×10⁻⁵cm² π polarization 654 nm pump. Open circles: experimental points, solid lines: calculated from Equations (3.6) with the parameter values in Table 3.7 and 3.9. (STD deviation=0.023898)

Table 3.7 Fixed radiative decay rates in the fitting of the time dependent upconversion emissions of Tm^{3-} :YLiF₄ under 370 mW/3.42×10⁻⁵cm² pump.

A ₅₀ (s ⁻¹)	492
A ₅₁ (s ⁻¹)	3265
A ₅₂ (s ⁻¹)	1267
A ₅₃ (s ⁻¹)	876
A ₅₄ (s ⁻¹)	30
A ₄₀ (s ⁻¹)	3388
A ₄₁ (s ⁻¹)	6614
A ₄₂ (s ⁻¹)	1495
A ₄₃ (s ⁻¹)	75
A ₃₀ (s ⁻¹)	399
A ₃₁ (s ⁻¹)	227
A ₃₂ (S ⁻¹)	114

both σ and π polarizations are listed in Tables 3.8 and 3.9 (the parameters K.,, were obtained directly from the normalized rate equations (3.6) and the transfer parameters W_{iij} were obtained by dividing K_{iij} with the third power of the Tm^{3+} concentration n_{Tm}^{-3}). The transfer process W_{1144} turned out to be unimportant with σ polarized pump at low temperature (12 k) as can be seen from Table 3.8 (where the fitted values of W_{1144} was found to be zero). This may be the result of bad resonance in this transfer. However, at high temperature (300 k) it gains important as can seen in Table 3.8 and 3.9 (where W1144 has large values compared with the other transfer parameters). From figure 3.7 we can see that level (5) consists of many sublevels. These sublevels become broad at high temperature leading to a band structure of level (5) thus much better resonance for the energy transfer process W1144. At low temperature and in π polarization W_{1144} makes a significant contribution to the upconversion dynamics as shown in Table 3.9. This may also be the result of improved resonance of the transfer process.

3.3 Upconversion dynamics and pump-probe measurements of the upconversion gain in Tm³⁺:Y₂BaF₈

Figure 3.18 shows energy levels and various processes (pump, energy transfer, and radiative decay) which we used to determine the dynamics of upconversion in Tm³⁺:YBF. In treating the energy transfer processes, we first included in the rate

Table 3.8 Values of the parameters found in the fitting of the time dependent upconversion emissions of Tm^{3+} :YLiF₄ under σ polarization 370 mW/3.42×10⁻⁵cm² pump. (all the fitted K_{3300} =0)

Polar.	(σ)	(σ)	(o)
$\lambda_{\rm exc}$ (nm)	627	64€	650
T (K)	12	12	300
	Fit. Cal.	Fit. Cal.	Fit. Cal.
A ₂₀ (s ⁻¹)	0 434	0 434	0 434
A ₂₁ (s ⁻¹)	0 49	0 49	0 49
A ₁₀ (s ⁻¹)	15 89	15 89	15 89
σ ₁ (cm ²)	(7.71±0.14)	(6.86±0.71)	(5.20±0.03)
fit.	×10 ⁻²⁴	×10 ⁻²³	×10 ⁻²⁴
cal.	1.54×10 ⁻²⁰	1.54×10 ⁻²⁰	1.54×10 ⁻²⁰
σ ₂ (cm ²)	(2.00±0.16)	(3.86±0.38)	(1.90±0.05)
fit.	×10 ⁻²¹	×10 ⁻²¹	×10 ⁻²¹
cal.	4.04×10 ⁻²¹	4.04×10 ⁻²¹	4.04×10 ⁻²¹
σ_3 (Cin^2) fit. cal.	0.00	(3.42±0.28)×10 ⁻²¹	0
	4.25×10 ⁻²⁰	4.25×10 ⁻²⁰	4.25×10 ⁻²⁰
	Fitted	Fitted	Fitted
K ₂₂₂₂	(7.00±1.68)	(7.00±1.17)	(1.68±0.06)
(S ⁻¹)	×10 ⁸	×10 ⁸	×10 ⁹
W ₂₂₂₂	(9.02±2.16)	(9.02±1.51)	(2.16±0.08)
(S ⁻¹ Cm ⁹)	×10 ⁻⁵³	×10 ⁻⁵³	×10 ⁻⁵²
K ₂₂₃₃	(1.03±0.05)	(1.03±0.20)	(6.16±0.36)
(S ⁻¹)	×10 ¹⁰	×10 ¹⁰	×10 ¹¹
W ₂₂₃₃	(1.33±0.07)	(1.33±0.26)	(7.94±0.46)
(S ⁻¹ Cm ⁹)	×10 ⁻⁵¹	×10 ⁻⁵¹	×10 ⁻⁵⁰
K' ₂₂₂₂	(6.84±0.25)	0	(7.19±2.88)
(S ⁻¹)	×10 ⁷		×10 ⁷
W' ₂₂₂₂	(8.81±0.32)		(9.26±3.70)
(S ⁻¹ Cm ⁹)	×10 ⁻⁵⁴		×10 ⁻⁵⁴
K ₁₁₄₄ (s ⁻¹) W ₁₁₄₄ (s ⁻¹ cm ⁹)	0	0	(9.38±0.70) ×10 ¹⁴ (1.21±0.09) ×10 ⁻⁴⁶

Table 3.9 Values of the parameters found in the fitting of the time dependent upconversion emissions of Tm^3 :YLiF₄ under π polarization 370 mW/3.42×10⁻⁵cm² pump. (all the fitted K_{3300} =0)

porarreaction 57			1100ed K3300-07
Polarization	(π)	(π)	(π)
λ _{exc} (nm)	629	641	654
T (K)	12 Fit. Cal.	12 Fit. Cal.	300 Fit. Cal.
A ₂₀ (s ⁻¹)	0 434	0 434	0 434
A ₂₁ (s ⁻¹)	0 49	0 49	0 49
A ₁₀ (s ⁻¹)	15 89	15 89	15 89
σ ₁ (cm ²) fit.	(4.63±0.07) ×10 ⁻²³ 1.05×10 ⁻²⁰	(3.00±0.15) ×10 ⁻²³ 1.05×10 ⁻²⁰	(7.68±0.07) ×10 ⁻²⁴ 1.05×10 ⁻²⁰
σ ₂ (cm ²) fit.	(3.86±0.55) ×10 ⁻²¹ 2.76×10 ⁻²¹	(5.600.33) ×10 ⁻²¹ 2.76×10 ⁻²¹	(1.40±0.07) ×10 ⁻²² 2.76×10 ⁻²¹
$\sigma_3(cm^2)$ fit.	0 2.90×10 ⁻²⁰	(2.00±0.64) ×10 ⁻²² 2.90×10 ⁻²⁰	0 2.90×10 ⁻²⁰
	Fitted	Fitted	Fitted
$k_{2222} (s^{-1})$ $W_{2222} (s^{-1}Cm^9)$	(3.02±0.36) ×10 ⁷ (3.89±0.47) ×10 ⁻⁵⁴	(3.02±0.29) ×10 ⁷ (3.89±0.37) ×10 ⁻⁵⁴	(2.51±0.15) ×10° (3.23±0.19) ×10 ⁻⁵²
k ₂₂₃₃ (s ⁻¹) W ₂₂₃₃ (s ⁻¹ Cm ⁹)	(4.24±0.59) ×10° (5.46±0.76) ×10 ⁻⁵²	(6.06±0.44) ×10 ⁹ (7.81±0.56) ×10 ⁻⁵²	(3.83±0.32) ×10 ¹¹ (4.93±0.41) ×10 ⁻⁵⁰
k' ₂₂₂₂ (s ⁻¹) W' ₂₂₂₂ (s ⁻¹ cm ⁹)	(8.61±0.73) ×10 ⁶ (1.11±0.09) ×10 ⁻⁵⁴	(1.72±0.17) ×10 ⁷ (2.22±0.22) ×10 ⁻⁵⁴	(2.92±0.23) ×10 ⁸ (3.76±0.30) ×10 ⁻⁵³
k ₁₁₄₄ (s ⁻¹) W ₁₁₄₄ (s ⁻¹ cm ⁹)	(9.00±0.68) ×10 ¹¹ (1.16±0.09) ×10 ⁻⁴⁹	0	(5.56±0.30) ×10 ¹³ (7.16±0.39) ×10 ⁻⁴⁸

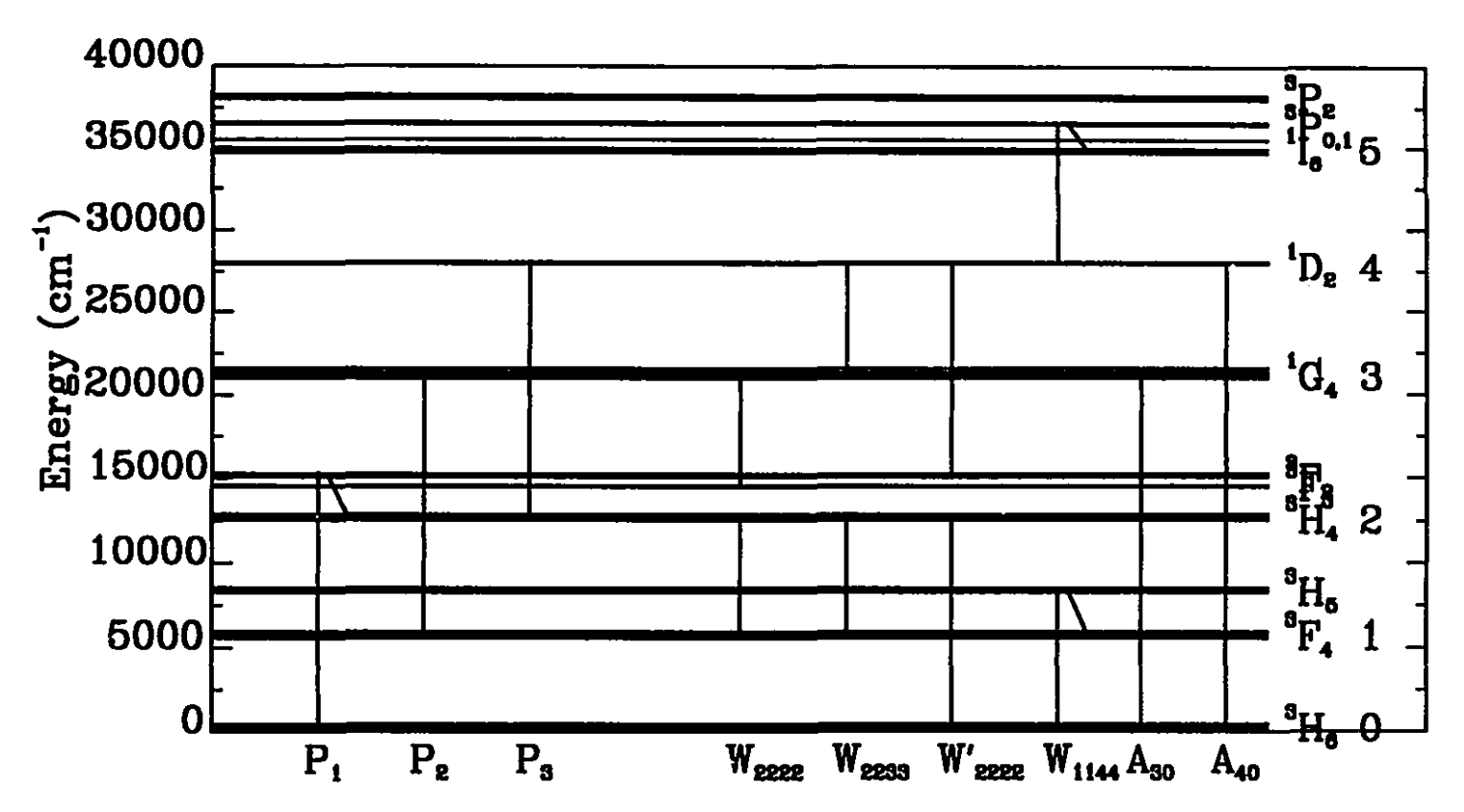


Figure 3.18

Energy level scheme of Tm^{3+} showing the energy transfer the pump and decay processes considered in the rate equations for the upconversion dynamics of $Tm^{3+}Y_2BaF_8$.

equations all the transfer processes with reasonable donor-acceptor energy matches, and then deleted those which had negligible effect on the solutions. To simplify the rate equations we treat the 3F_2 ; 3F_3 and 3H_4 levels as one level, and do the same with 3H_5 and 3F_4 . After the above considerations we get the following set of rate equations:

$$\begin{split} \dot{n}(0) &= -P_1 \left[n(0) - n(2) \right] \\ &+ A_{50} n(5) + A_{40} n(4) + A_{30} n(3) + A_{20} n(2) + A_{10} n(1) \\ &+ 2 W'_{2222} n^4(2) + 2 W_{1144} n^2(1) n^2(4) \\ &- 2 W_{3300} n^2(3) n^2(0) \\ \dot{n}(1) &= -P_2 \left[n(1) - n(3) \right] \\ &+ A_{51} n(5) + A_{41} n(4) + A_{31} n(3) + A_{21} n(2) - A_{10} n(1) \\ &+ 2 W_{2222} n^4(2) + 2 W_{2233} n^2(2) n^2(3) \\ &- 2 W_{1144} n^2(1) n^2(4) + 2 W_{3300} n^2(3) n^2(0) \\ \dot{n}(2) &= P_1 \left[n(0) - n(2) \right] - P_3 \left[n(2) - n(4) \right] \\ &+ A_{52} n(5) + A_{42} n(4) + A_{32} n(3) - A_{2} n(2) \\ &- 4 \left[W_{2222} + W'_{2222} \right] n^4(2) - 2 W_{2233} n^2(2) n^2(3) \\ &+ 4 W_{3300} n^2(3) n^2(0) \\ \dot{n}(3) &= P_2 \left[n(1) - n(3) \right] \\ &+ A_{53} n(5) + A_{43} n(4) - A_{3} n(3) \\ &+ 2 W_{2222} n^4(2) - 2 W_{2233} n^2(2) n^2(3) \\ &- 2 W_{3300} n^2(3) n^2(0) \\ \dot{n}(4) &= P_3 \left[n(2) - n(4) \right] + A_{54} n(5) - A_4 n(4) + 2 W'_{2222} n^4(2) \\ &+ 2 W_{2233} n^2(2) n^2(3) - 2 W_{1144} n^2(1) n^2(4) \\ \dot{n}(5) &= - A_{51} n(5) + 2 W_{1144} n^2(1) n^2(4) \end{split}$$

where W_{iijj} are fourth-order energy transfer parameters. By dividing the total Tm^{3+} concentration n_{Tm} (1.98×10²⁰ cm⁻³) on both sides of equations (3.7) we obtain the following normalized rate equations:

```
\phi(0) = -P_1[\rho(0) - \rho(2)]
        +A_{50}\rho(5)+A_{40}\rho(4)+A_{30}\rho(3)+A_{20}\rho(2)+A_{10}\rho(1)
        +2K'_{2222}\rho^{4}(2)+2K_{1144}\rho^{2}(1)\rho^{2}(4)
        -2K_{3300}\rho^{2}(3)\rho^{2}(0)
\phi(1) = -P_2[\rho(1) - \rho(3)]
        +A_{51}\rho(5)+A_{41}\rho(4)+A_{31}\rho(3)+A_{21}\rho(2)-A_{10}\rho(1)
        +2K_{2222}\rho^4(2)+2K_{2233}\rho^2(2)\rho^2(3)
        -2K_{1144}\rho^2(1)\rho^2(4)+2K_{3300}\rho^2(3)\rho^2(0)
\phi(2) = P_1 [\rho(0) - \rho(2)] - P_2 [\rho(2) - \rho(4)]
        +A_{52}\rho(5)+A_{42}\rho(4)+A_{32}\rho(3)-A_{2}\rho(2)
                                                                                              (3.8)
        -4 \left[ K_{2222} + K'_{2222} \right] \rho^4 (2) -2 K_{2233} \rho^2 (2) \rho^2 (3)
        +4K_{3300}\rho^{2}(3)\rho^{2}(0)
\dot{\rho}(3) = P_2[\rho(1) - \rho(3)]
        +A_{53}\rho(5)+A_{43}\rho(4)-A_{3}\rho(3)
        +2K_{223}\rho^{4}(2)-2K_{223}\rho^{2}(2)\rho^{2}(3)
        -2K_{3300}\rho^2(3)\rho^2(0)
\dot{\rho}(4) = P_3 \left[ \rho(2) - \rho(4) \right] + A_{54} \rho(5) - A_4 \rho(4) + 2K'_{2222} \rho^4(2)
        +2K_{2233}\rho^{2}(2)\rho^{2}(3)-2K_{1144}\rho^{2}(1)\rho^{2}(4)
\phi(5) = -A_{51}\rho(5) + 2K_{11A4}\rho^{2}(1)\rho^{2}(4)
```

 $\rho(i) = n(i) / n_{Tm}$ are normalized concentrations where $K_{ii+1}=W_{ii+1}n_{m}^{3}$. Using equation (3.8) to fit the experimental data we fix the radiative decay rates (except A_{20} , A_{21} and A_{10}) at their calculated values and then vary the pump rates and parameters K₁₁₁₁ to obtain the best fit for both the ¹G₄ and ¹D₂ emissions simultaneously. The fitting for the low temperature (11.9 K) data is shown in Figure 3.19, and for the room temperature data in Figure 3.20. The fixed rediative decay rates are listed in Table 3.10. The values of the other parameters determined from the fitting are listed in Table 3.11. In Table 3.11 the parameters Kiiii were obtained directly from the normalized rate equations (3.8) and the fitted transfer parameters W_{iiji} were obtained by dividing K_{iiii} with the third power of Tm3+ concentration in Tm3+:Y,BaFa.

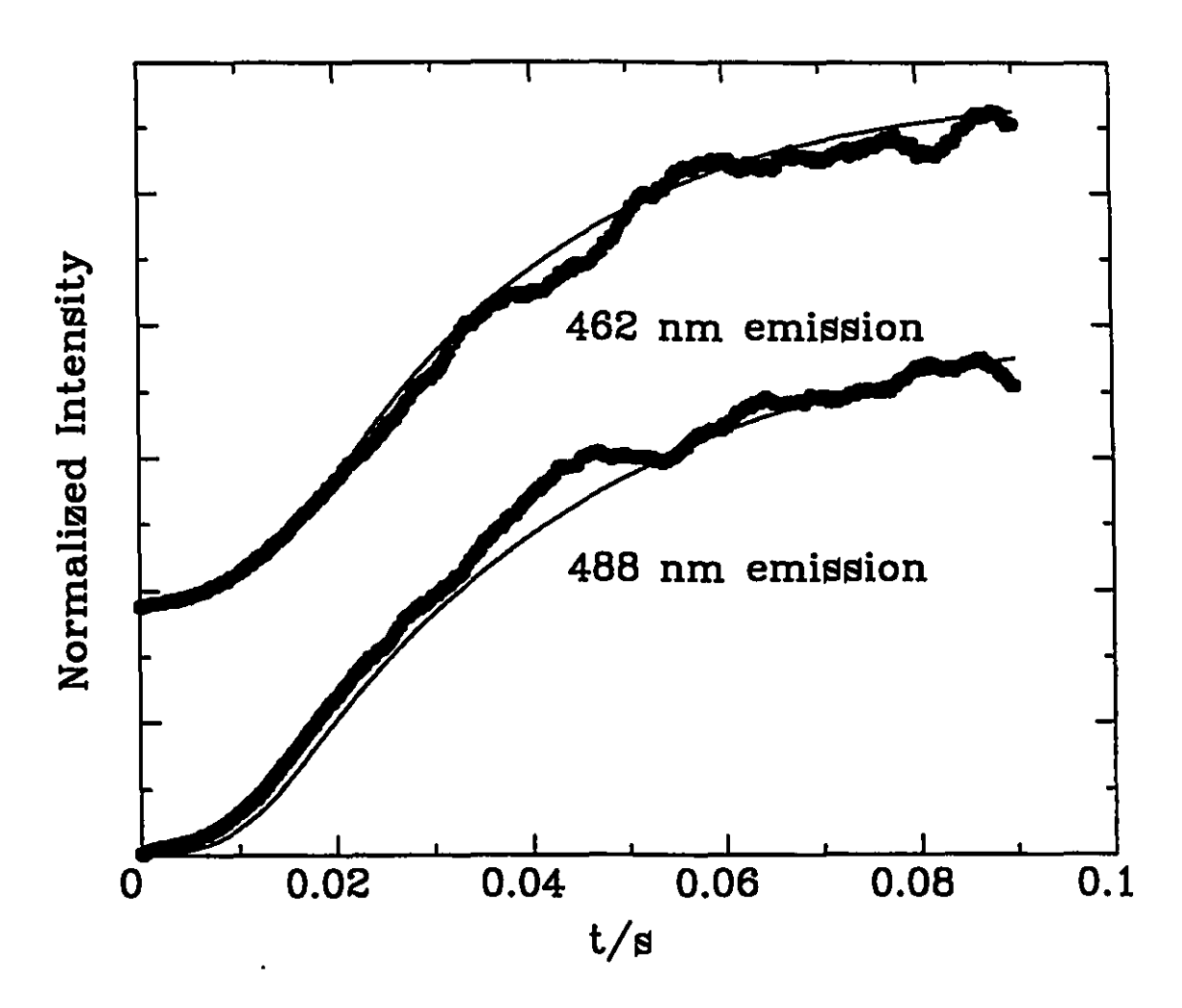


Figure 3.19

Time dependence of the upconversion emission of $Tm^{3+}:Y_2BaF_8$ at 491 nm ($^3H_6 \leftarrow ^1G_4$) and 464 nm ($^3F_4 \leftarrow ^1D_2$) at 12 K under 260 mw/3.42×10⁻⁵cm² 628.5nm pump. Open circles: experimental points, solid lines: calculated from Equations (3.8) using the parameter values in Table 3.10 and 3.11.

(STD deviation=0.039818)

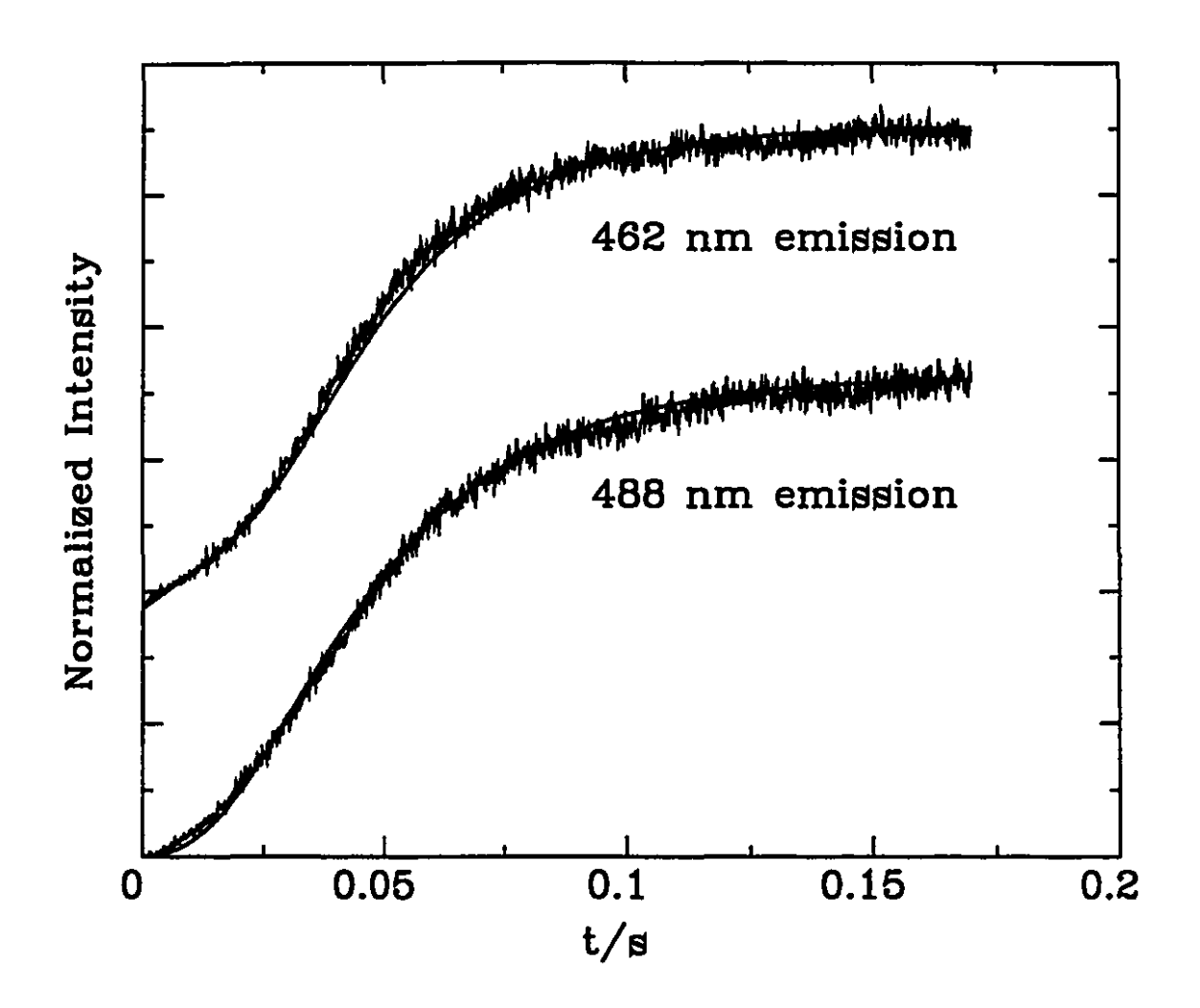


Figure 3.20

Time dependence of the upconversion emission of Tm^{3+} : Y_2BaF_8 at 488 nm ($^3H_6 \leftarrow ^1G_4$) and 462 nm ($^3F_4 \leftarrow ^1D_2$) at 300 K under 350 mw/3.42×10⁻⁵cm² 628.5 nm pump. Open circles: experimental points, solid lines: calculated from Equations (3.8) using the parameter values in Table 3.10 and 3.11.

(STD deviation=0.045920)

Table 3.10 Fixed decay rates in the fittings of the time dependent upconversion emission experimental data of Tm^{3+} : Y_2BaF_8 .

A ₅₀ (s ⁻¹)	A ₅₁ (s ⁻¹)	A ₅₂ (s ⁻¹)
420	3503	1353
A ₅₃ (s ⁻¹)	A ₅₄ (S ⁻¹)	A ₄₀ (s ⁻¹)
838	51	3427
A ₄₁ (s ⁻¹)	A ₄₂ (s ⁻¹)	A ₄₃ (s ⁻¹)
3553	1161	45
A ₃₀ (s ⁻¹)	A ₃₁ (s ⁻¹)	A ₃₂ (s ⁻¹)
277	379	126

Table 3.11 Values of parameters obtained from the fittings of the time dependent upconversion emission experimental data of $Tm^{3+}:Y_2BaF_8$ compared with the calculated values (all the fitted

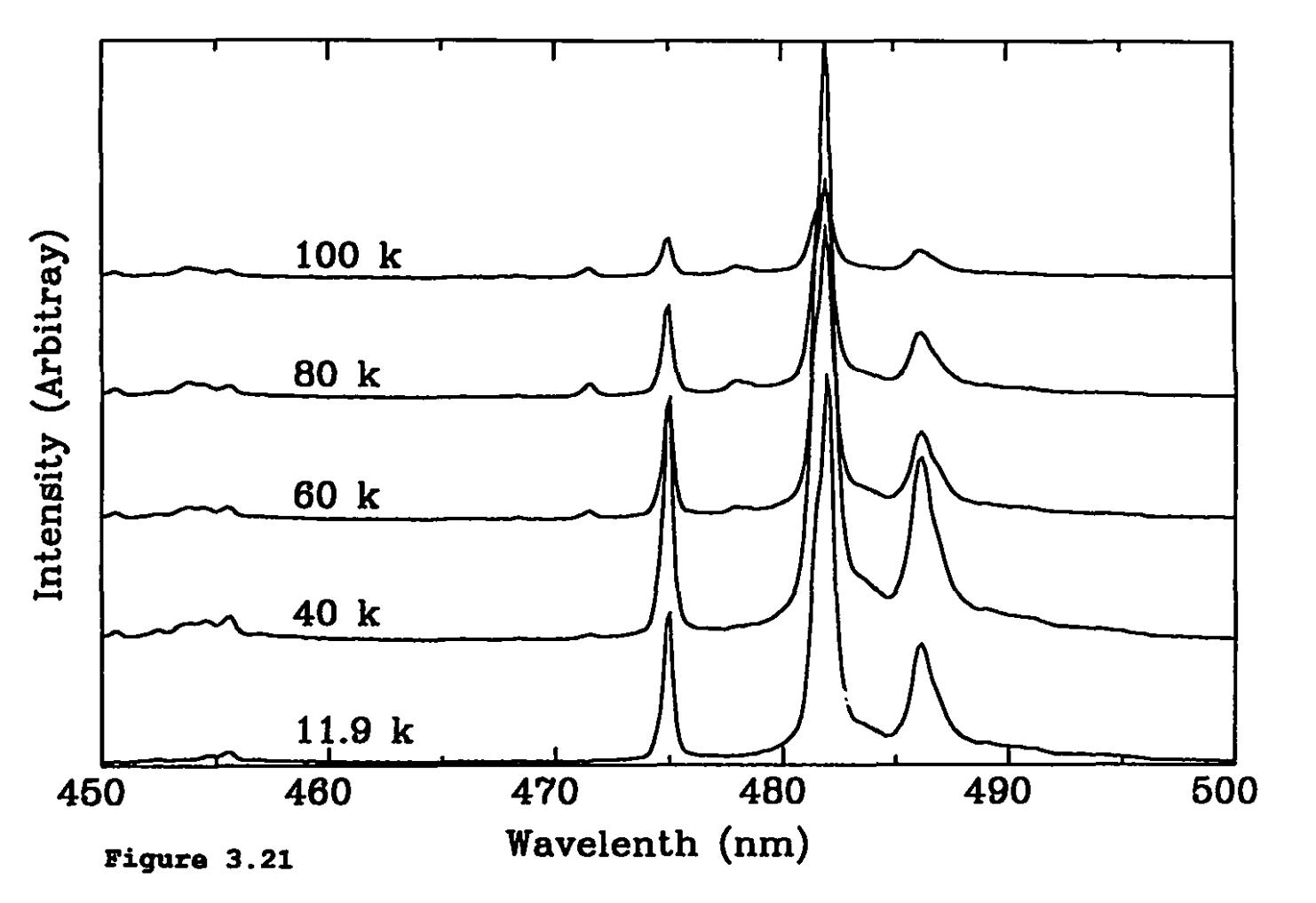
 $K_{3300}=0$). $(n_{Tm}=6.50\times10^{20} \text{ cm}^{-3}, n_{Y}=1.30\times10^{22} \text{ cm}^{-3}, a_{Y}=5.28 \text{ Å})$

Temperature	12 k	300 k
λ _{exc} (nm)	628.5	628.5
σ ₁ (cm²) fitted calculated	(9.90±0.16)×10 ⁻²⁴ 2.96×10 ⁻²⁰	(5.68±0.06)×10 ⁻²⁴ 2.96×10 ⁻²⁰
σ ₂ (cm ²) fitted calculated	(2.98±0.12)×10 ⁻²¹ 5.93×10 ⁻²¹	(2.84±0.04)×10 ⁻²¹ 5.93×10 ⁻²¹
σ_3 (cm ²) fitted calculated	(1.48±0.19)×10 ⁻²² 4.36×10 ⁻²⁰	(2.13±0.07)×10 ⁻²² 4.36×10 ⁻²⁰
A ₂₀ (s ⁻¹) fitted calculated	0 444	0 444
A ₂₁ (s ⁻¹) fitted calculated	15 50	15 50
A ₁₀ (s ⁻¹) fitted calculated	0 64	0 64
	fitted	fitted
K ₂₂₂₂ (s ⁻¹) W ₂₂₂₂ (s ⁻¹ cm ⁹)	(7.70±0.42)×10 ⁷ (2.80±0.15)×10 ⁻⁵⁵	(7.80±0.40)×10 ⁷ (2.84±0.14)×10 ⁻⁵⁵
K ₂₂₃₃ (s ⁻¹) W ₂₂₃₃ (s ⁻¹ cm ⁹)	(3.04±2.71)×10 ¹⁰ (1.09±0.98)×10 ⁻⁵²	(3.90±0.37)×10 ¹⁰ (1.42±0.14)×10 ⁻⁵²
K' 2222 (S ⁻¹) W' 2222 (S ⁻¹ CM ⁹)	(3.30±0.36)×10 ⁷ (1.20±0.13)×10 ⁻⁵⁵	(3.60±0.17)×10 ⁷ (1.31±0.06)×10 ⁻⁵⁵
$K_{1144} (s^{-1})$ $W_{1144} (s^{-1}cm^3)$	(5.60±1.46)×10 ¹⁰ (2.04±0.53)×10 ⁻⁵²	(5.80±1.62)×10 ¹⁰ (2.11±0.59)×10 ⁻⁵²

For reference we show the upconversion emission at various temperatures in Figure 3.21, and indicate the particular lines which were probed (the 475.04 nm line: ${}^{1}G_{4}$ (21183 cm⁻¹) \rightarrow ${}^{3}H_{6}$ (119 cm⁻¹), the 482.10 nm line: ${}^{1}G_{4}$ (20883cm⁻¹) \rightarrow ${}^{3}H_{6}$ (141 cm⁻¹), the 486.22 nm line: ${}^{1}G_{4}$ (20883 cm⁻¹) \rightarrow ${}^{3}H_{6}$ (186 cm⁻¹)). We recorded the power dependence of the gain for the 482.10 nm line at a series of temperatures between 11.9 k and 220 k. Figure 3.22 shows the power dependence of the gain for this transition measured at 11.9 k. Extrapolation to zero power reveals no threshold for the stimulated emission of this transition.

We specifically probed the ${}^1G_4 \rightarrow {}^3H_6$ transition at 482 nm. Because of the broad amplified spontaneous emission present in the wings of the probe laser pulses, relatively large spectral regions could be probed simultaneously. As in reference [64], spectra with pump plus probe, probe only, and pump only were recorded, and the gain spectrum was displayed by comparing I $_{(\text{pump+probe})}$ - I $_{\text{pump}}$ with I $_{\text{probe}}$. Figure 3.23 shows such an upconversion gain spectrum at 120 K for a pump wavelength of 628 nm and a probe wavelength centred at 482 nm. From Table 3.11 we may see that among the three absorption cross sections only G_2 is in reasonable agreement with the calculated value. The fitted G_1 and G_3 are much smaller than the calculated ones. The calculations assume perfect resonance, and we can see that pump one and three are not in resonance while pump two is close to resonance.





Upconversion emissions spectra of Tm^{3} ' Y_2BaF_8 at various temperatures.

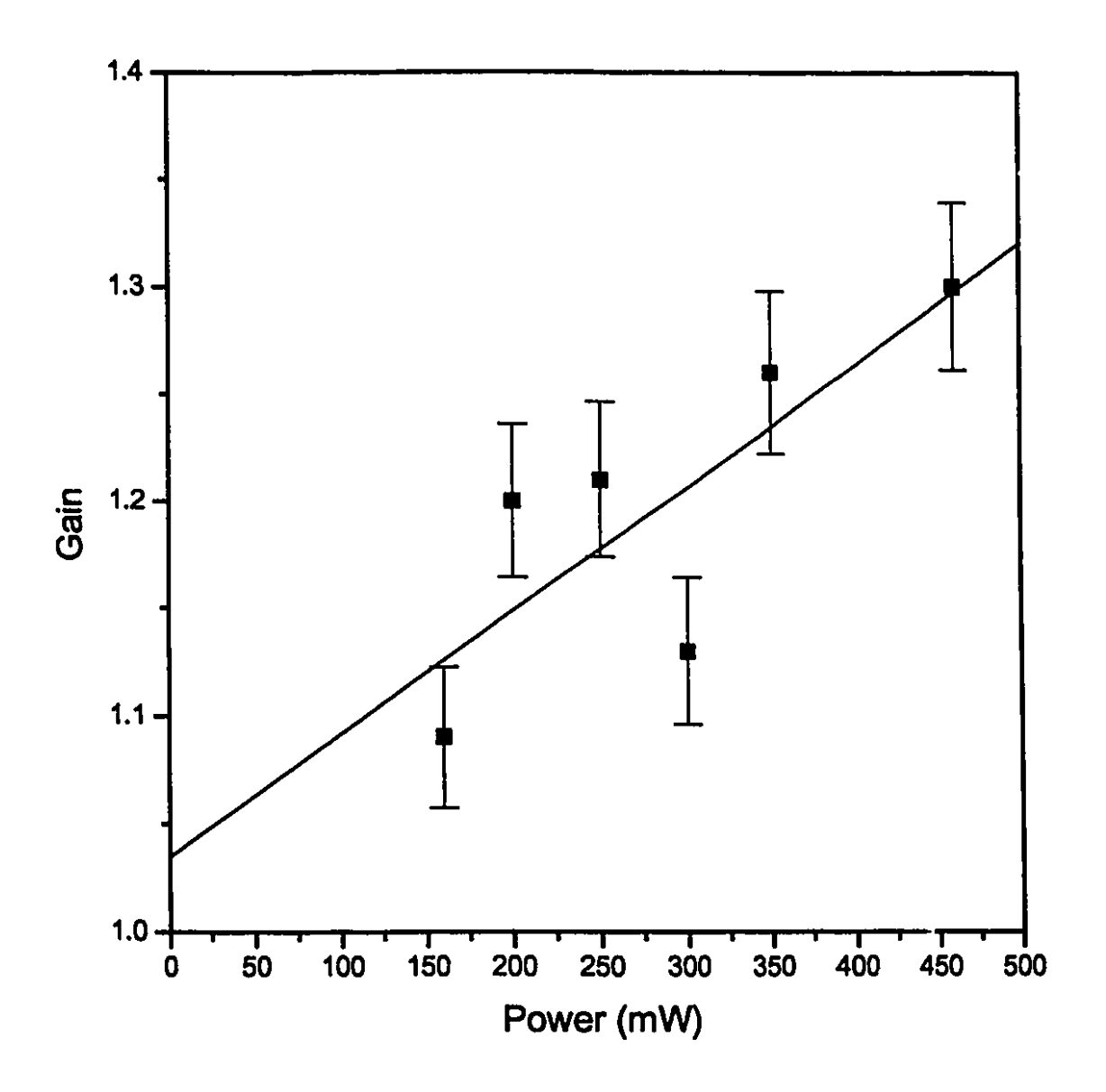
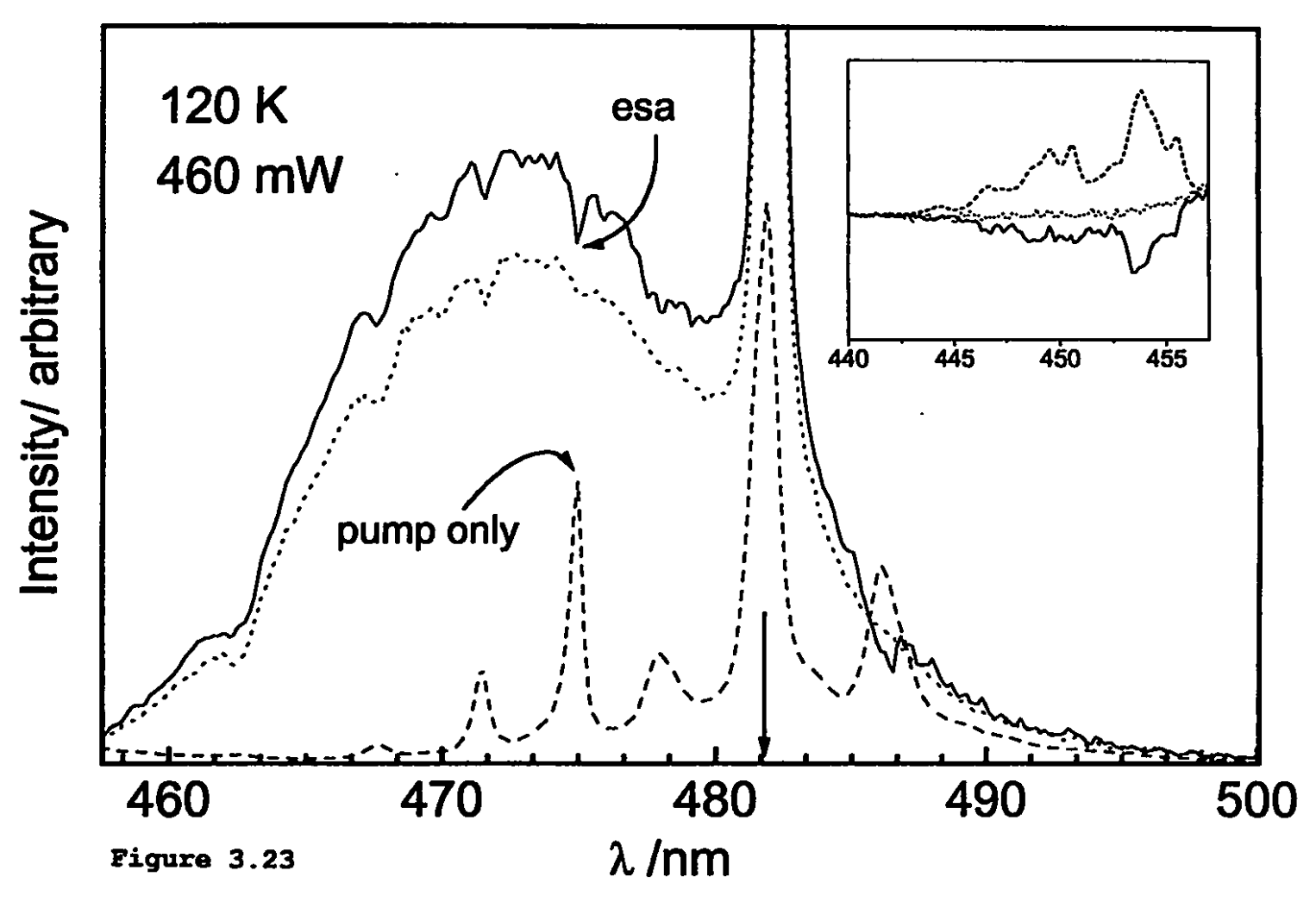


Figure 3.22 Pump power dependence of the 482.10 nm ($^3H_6 \leftarrow ^1G_4$) emission upconversion gain in Tm $^{3+}$:Y₂BaF₈.



Broad upconversion gain spectrum of $Tm^{3+}Y_2BaF_8$ at 120 K for a pump wavelength of 628 nm and a probe wavelength centred at 482.10 nm.

We notice that there is a broad gain bandwidth ranging from 460 nm to 490 nm. This observation is in sharp contrast to the results for Tm3+:YLF, in which case the gain was restricted to the narrow emission lines. We obtained numerical results for the gain at three different probe wavelengths from the areas of $[I_{(pump+probe)} - I_{pump}] / I_{probe}$. values are given in Table 3.12. In Table 3.12 we also include the temperature dependence of the gain of the 482.10 nm emission line, which exhibits a curious maximum at some temperature near 160 K, before decreasing to unity (no gain or loss) at higher temperatures (c.a. 200 K). This unusual temperature behaviour, and the broad band gain exhibited over the range of 460 nm - 490 nm, may both result from stimulated emission from thermally populated higher Stark levels at higher temperatures. Eventually the thermal population of the terminal Stark level of the 3H6 manifold reaches the point where further stimulated emission is discouraged.

Table 3.12 Measured gain for three emission lines in the ${}^{1}G_{4} \rightarrow {}^{3}H_{6}$ (475.0 nm: 21183 cm $^{-1} \rightarrow$ 119 cm $^{-1}$, 482nm: 20883 cm $^{-1} \rightarrow$ 141 cm $^{-1}$, 486.0 nm: 20883 cm $^{-1} \rightarrow$ 186 cm $^{-1}$) manifold of Tm $^{3+}$:Y₂BaF₈.

Probe	Pump power	Temp.	Gain	α
λ (nm)	(mW/3.42×10 ⁻⁵ cm ²)	(K)	ratio	(cm ⁻¹)
475.0	400	11.9	1.17±0.04	0.31±0.07
482.0	460	11.9	1.30±0.04	0.52±0.06
	420	40	1.31±0.04	0.54±0.05
	420	60	1.17±0.04	0.31±0.07
	420	80	1.14±0.03	0.26±0.05
	450	100	1.05±0.03	0.10±0.07
	460	120	1.26±0.04	0.46±0.06
	450	140	1.31±0.04	0.54±0.06
	450	160	1.40±0.04	0.67±0.06
	450	180	1.13±0.03	0.24±0.06
	450	200	1.01±0.03	0.02±0.06
	450	220	1.04±0.03	0.08±0.06
486.0	400	11.9	1.28±0.04	0.49±0.08

3.4 Theoretical considerations

3.4.1 Four-body interaction transfer model

The three-body process was previously analyzed[60],[61] and gives the third power energy transfer terms in the coupled rate equations. This approach is not suitable to our case because of the energy matches which can not yield a three-body transfer. So we consider the four-body process which involves four ions, each of which can act either as a donor or an acceptor. The rate of radiationless energy transfer between the initial states and the final states is given by[21]:

$$\gamma_{ir} = (2\pi/h) |\langle i|\tau|f \rangle|^2 S \tag{3.9}$$

where S is the overlap integral and τ is given to second order in the perturbation by:

$$\tau = H' + \sum_{m \neq i} H' | m \rangle m | H' (\varepsilon_i - \varepsilon_m)^{-1}$$
 (3.10)

where ε_i is the energy of the zero-order state $|i\rangle$.

We assume that $|i\rangle$ (or $|f\rangle$) may be represented as a simple product of four one-electron atomic wavefunctions:

$$|\vec{i}\rangle = \psi(a) \psi(b) \psi(c) \psi(d) |\vec{f}\rangle = \psi(a') \psi(b') \psi(c') \psi(d')$$
(3.11)

where a, b, c, and d label the electrons associated with ion a, ion b, ion c and ion d, respectively. Neglect the exchange effects the interaction Hamiltonian is

$$H' = H'_{ab} + H'_{ac} + H'_{ad} + H'_{bc} + H'_{bd} + H'_{cd}$$
 (3.12)

where in the dipole-dipole limit a typical term of the right

side takes the form:

$$H_{ab}^{\prime} = (e^2/\kappa R_{ab}^3) r_a \cdot T(ab) \cdot r_b \tag{3.13}$$

where

$$T(ab) = 1 - 3 \left(\hat{R}_{ab} \hat{R}_{ab} \right) \tag{3.14}$$

and H_{ab} ' is the interaction between ion a and ion b, \mathbf{r}_a and \mathbf{r}_b are the electric dipole moment operator for ion a and ion b, \mathbf{R}_{ab} is the vector separation of ion a and ion b, and

$$\hat{R}_{ab} = \frac{R_{ab}}{R_{ab}} \tag{3.15}$$

is the unit vector in the direction of R_{ab} .

The first-order contribution to the matrix element $\langle i|\tau|f\rangle$ is a sum of the terms of the form:

$$\langle i|H'_{ac}|f\rangle = \langle abcd|H'_{ac}|a'b'c'd'\rangle$$

$$= (e^{2}/\kappa R_{ac}^{3})$$

$$\times \langle a|\mathbf{r}_{a}|a'\rangle \cdot \mathbf{T}(ac) \langle c|\mathbf{r}_{c}|c'\rangle$$

$$\times \langle b|b'\rangle \langle d|d'\rangle$$
(3.16)

These matrix elements will vanish by orthogonality unless there is a simple pairwise transfer of the excitation.

$$\varepsilon_a + \varepsilon_c = \varepsilon_{a'} + \varepsilon_{c'} \tag{3.17}$$

or

$$\mathbf{e}_{\mathbf{a}} - \mathbf{e}_{\mathbf{a}'} = \mathbf{e}_{\mathbf{c}'} - \mathbf{e}_{\mathbf{c}} \tag{3.18}$$

which indicate the excitation is transferred directly from ion a to ion c. This process is a tow-body transfer process which is electric dipole-dipole forbidden for free ion case[1], [9], [10]. So this transition may be very weak.

For the second-order contribution to $\langle i | \tau | f \rangle$ we have

$$\sum_{m\neq i} \langle i | H' | m \rangle m | H' | f \rangle (\epsilon_i - \epsilon_m)^{-1}$$

$$= [H_{ab}] [H_{ac}] + [H_{ac}] [H_{bd}] + \cdots$$
(3.19)

There are 30 terms in (3.19). A typical term is

$$[H_{ac}] [H_{bd}] = \sum_{\mathbf{a}_{m}} \sum_{\mathbf{b}_{m}} \sum_{\mathbf{c}_{m}} \sum_{\mathbf{d}_{m}} \langle \mathbf{a} \mathbf{b} \mathbf{c} \mathbf{d} | H_{ac} | \mathbf{a}_{m} \mathbf{b}_{m} \mathbf{c}_{m} \mathbf{d}_{m} \rangle$$

$$\times \langle \mathbf{a}_{m} \mathbf{b}_{m} \mathbf{c}_{m} \mathbf{d}_{m} | H_{bd} | \mathbf{a}' \mathbf{b}' \mathbf{c}' \mathbf{d}' \rangle$$

$$\times (\varepsilon_{i} - \varepsilon_{m})^{-1}$$
(3.20)

which may be rewritten as:

$$[H_{ac}] [H_{bd}] = \sum_{a_{m}} \sum_{b_{m}} \sum_{c_{m}} \sum_{d_{m}} \langle ac|H'_{ac}|a_{m}c_{m} \rangle b|b_{m} \rangle d|d_{m} \rangle$$

$$\times \langle b_{m}d_{m}|H_{bd}|b'd' \rangle \langle a_{m}|a' \rangle \langle c_{m}|c' \rangle$$

$$\times (\varepsilon_{i}-\varepsilon_{m})^{-1}$$
(3.21)

by orthogonality, (3.21) may be reduced to

$$[H_{ac}] [H_{bd}]$$

$$= \langle ac|H'_{ac}|a'c'\rangle bd|H'_{bd}|b'd'\rangle$$

$$\times (\frac{1}{\varepsilon_{b'd'}^{-\varepsilon_{bd}}} + \frac{1}{\varepsilon_{ac}^{-\varepsilon_{a'c'}}})$$

$$= \frac{e^{2}}{kR_{ac}^{3}} \langle a|\mathbf{r}_{a}|a'\rangle \cdot \mathbf{T}(ac) \langle c|\mathbf{r}_{c}|c'\rangle$$

$$\times \frac{e^{2}}{kR_{bd}^{3}} \langle b|\mathbf{r}_{b}|b'\rangle \cdot \mathbf{T}(bd) \langle d|\mathbf{r}_{d}|d'\rangle$$

$$\times (\frac{1}{\varepsilon_{b'd'}^{-\varepsilon_{bd}}} + \frac{1}{\varepsilon_{ac}^{-\varepsilon_{a'c'}}})$$
(3.22)

We can obtain an approximate expression for the second-order transfer matrix element by the approximation that

$$\varepsilon_i - \varepsilon_m \sim \Delta \varepsilon$$
 (3.23)

for all intermediate states m. and define

$$\beta_{ac} = \frac{e^2}{k} \langle a | x_a | a \rangle \cdot T(ac) \langle c | x_c | c \rangle$$

$$\beta_{bd} = \frac{e^2}{k} \langle a | x_b | b \rangle \cdot T(bd) \langle d | x_d | d \rangle$$
(3.24)

Thus

$$[H_{ac}] [H_{bd}] = \frac{2}{(\Delta \epsilon)} \frac{\beta_{ac}\beta_{bd}}{R_{ac}^3 R_{bd}^3}$$
(3.25)

and

$$\gamma_{abcd} = (\frac{4\pi^{2}}{h}) | [H_{ab}] [H_{ac}] + [H_{ac}] [H_{bd}] + \dots |^{2}S$$

$$= (\frac{4\pi^{2}}{h}) (\frac{4}{\Delta \epsilon^{2}}) [\frac{\beta_{ab}^{2} \beta_{ac}^{2}}{R_{ab}^{6} R_{ac}^{6}} + \frac{\beta_{ac}^{2} \beta_{bd}^{2}}{R_{ac}^{6} R_{bd}^{6}} + \dots] S$$
(3.26)

With the approximation that $R_{ab}=R_{ac}=\ldots=R$, the four-body energy transfer rate is given by:

$$\gamma_{abcd} = (\frac{4\pi^2}{h}) (\frac{4}{\Delta \varepsilon^2}) \frac{1}{R^{12}} [\beta_{ab}^2 \beta_{ac}^2 + \beta_{ac}^2 \beta_{bd}^2 + \dots] S
= \frac{C_{abcd}}{R^{12}}$$
(3.27)

Since the transfer rate is proportional to R⁻¹² we need only to consider the nearest neighbour interactions. Because the activators are randomly distributed among the lattice points, the nearest neighbour distance is just the lattice distance (in our cases it is the nearest Yttrium -Yttrium distance in the crystals), so we may consider only the interaction within a unit cell. Thus the basic rate equation for the ion a takes the form:

$$\frac{d\rho_{i}^{a}(t)}{dt} = \frac{1}{\tau_{a}} \rho_{i}^{a}(t) - \frac{C_{abcd}}{a^{12}} \rho_{i}^{a}(t) \rho_{i}^{b}(t) \rho_{i}^{c}(t) \rho_{i}^{d}(t) + \dots$$
 (3.28)

where $\rho^{a}_{i}(t)$, $\rho^{b}_{i}(t)$, $\rho^{c}_{i}(t)$ and $\rho^{d}_{i}(t)$ are the possibilities of finding an ion a, b, c and d in the ith unit cell separately. Since the activators (donors and acceptors) are randomly distributed among the lattice points, every lattice point has the same possibility of being occupied by an ion a and the same possibility of being occupied by an ion b and so on. So we have:

$$\rho_{i}^{a}(t) = \frac{N_{a}(t)}{N_{T}}, \rho_{i}^{b}(t) = \frac{N_{b}(t)}{N_{T}}$$

$$\rho_{i}^{c}(t) = \frac{N_{c}(t)}{N_{T}}, \rho_{i}^{d}(t) = \frac{N_{d}(t)}{N_{T}}$$
(3.29)

where and $N_a(t)$, $N_b(t)$, $N_c(t)$, $N_d(t)$ and N_T are the total number of ion a, b, c, d and the total number of the lattice points in the total interactional volume V_T separately. Bring the results of equation (3.29) to equation (3.28) we obtain:

$$\frac{d}{dt}N_a(t) = -\frac{1}{\tau_a}N_a(t) - \frac{N_a(t)N_b(t)N_c(t)N_d(t)}{(N_T)^3} \frac{C_{abcd}}{a^{12}} + \dots (3.30)$$

dividing by the total interaction volume V_{τ} on both sides of equation (3.30) gives the following the rate equation:

$$\frac{dn_{a}(t)}{dt} = -\frac{1}{\tau_{a}}n_{a}(t) - \frac{N_{a}N_{b}N_{c}N_{d}}{N_{T}^{3}} \frac{1}{V_{T}} \frac{C_{abcd}}{a^{12}} + \cdots$$

$$= -\frac{1}{\tau_{a}}n_{a}(t) - n_{a}n_{b}n_{c}n_{d} \frac{V_{T}^{3}}{N_{T}^{3}} \frac{C_{abcd}}{a^{12}} + \cdots$$

$$= -\frac{1}{\tau_{a}}n_{a}(t) - n_{a}n_{b}n_{c}n_{d}W_{abcd} + \cdots$$
(3.31)

where W_{abcd} is the four-body transfer parameter which can be expressed as:

$$W_{abcd} = \left(\frac{V_T}{N_T}\right)^3 \frac{C_{abcd}}{a^{12}}$$

$$= \frac{\gamma_{abcd}(R=a)}{(n_T)^3}$$
(3.32)

where n_T is the total concentration of lattice points (in crystals of Er^{3+} :YAG, Er^{3+} :YAlO₃, Tm^{3+} :YLiF₄ and Tm^{3+} :Y₂BaF₈ they are the concentrations of Yttrium in YAG, YAlO₃, YLiF₄ and Y₂BaF₈ which are given in Table 1.2)

Kushida[23] used the Judd[11]-Offelt[12] theory to calculate the energy transfer rates for the cases of two-body dipole-dipole interaction and three-body dipole-quadrupole interaction. This can be extended to the calculation of four-body energy transfer rates. In our case, the four-body interaction we need to consider are all of the type which involve two donors and two acceptors. The Hamiltonian in (3.12) can then be written as:

$$H' = H'_{aa} + 4H'_{ab} + H'_{bb}$$
 (3.33)

and the second-order contribution to $|\langle i|\tau|f\rangle|^2$ becomes:

$$\begin{split} & \left| \sum_{m \neq i} \langle i | H' | m \rangle m | H' | f \rangle (\epsilon_1 - \epsilon_m)^{-1} \right|^2 \\ &= (8 [H_{aa}] [H_{ab}] + 8 [H_{bb}] [H_{ab}] + 2 [H_{aa}] [H_{bb}] + 16 [H_{ab}]^2)^2 \\ &= 64 [H_{aa}]^2 [H_{ab}]^2 + 64 [H_{bb}]^2 [H_{ab}]^2 + 4 [H_{aa}]^2 [H_{bb}]^2 + 256 [H_{ab}]^4 \\ &+ 192 [H_{aa}] [H_{bb}] [H_{ab}]^2 + 32 [H_{aa}]^2 [H_{ab}] [H_{bb}] + 256 [H_{aa}] [H_{ab}]^3 \\ &+ 32 [H_{bb}]^2 [H_{ab}] [H_{aa}] + 256 [H_{bb}] [H_{ab}]^3 \end{split}$$

In the dipole-dipole case[21]

$$\langle ab|H'_{ab}|a'b'\rangle = (\frac{2}{3})^{1/2} \frac{e^2}{R_{ab}^3} \sum_{m_1=1}^1 \sum_{m_2=1}^1 \langle a|D_{m_1}^{(1)} a' \langle b|D_{m_2}^{(1)}|b'\rangle \quad (3.35)$$

SO

$$[H_{ab}] = (\frac{2}{\Delta \varepsilon})^{1/2} \langle ab | H'_{ab} | a'b' \rangle$$

$$= (\frac{2}{3})^{1/2} \frac{e^2}{R_{ab}^3} (\frac{2}{\Delta \varepsilon})^{1/2} \sum_{m_1 = -1}^{1} \sum_{m_2 = -1}^{1} \langle a | D_{m_1}^{(1)} | a' \langle b | D_{m_2}^{(1)} | b' \rangle$$
(3.36)

Thus

$$[H_{ab}]^{2} = (\frac{2}{3}) \frac{e^{4}}{R_{ab}^{6}} \frac{2}{\Delta \varepsilon}$$

$$\times \sum_{m_{1}=-1}^{1} \sum_{m_{2}=-1}^{1} \langle a | D_{m_{1}}^{(1)} | a \rangle \langle b | D_{m_{2}}^{(1)} | b \rangle$$

$$\times \sum_{m_{1}=-1}^{1} \sum_{m_{2}=-1}^{1} \langle a | D_{m_{3}}^{(1)} | a \rangle \langle b | D_{m_{4}}^{(1)} | b \rangle$$
(3.37)

Neglecting cross terms m₁≠m₃, m₂≠m₄

$$[H_{ab}]^{2} = (\frac{2}{3}) \frac{e^{4}}{R_{ab}^{6}} \frac{2}{\Delta \varepsilon}$$

$$\times \sum_{m_{1}=-1}^{1} \langle a | D_{m_{1}}^{(1)} | a' \rangle^{2} \times \sum_{m_{1}=-1}^{1} \langle b | D_{m_{2}}^{(1)} | b' \rangle^{2}$$
(3.38)

Since[11],[12]:

$$\sum_{m=-1}^{1} \langle a | D_{m}^{(1)} | a^{2} \rangle = \sum_{\lambda=2,4,6} \Omega_{\lambda} \langle J_{a} | U^{(\lambda)} | J_{a}^{2} \rangle^{2} = S_{a}$$

$$\sum_{m=-1}^{1} \langle b | D_{m}^{(1)} | b^{2} \rangle = \sum_{\lambda=2,4,6} \Omega_{\lambda} \langle J_{b} | U^{(\lambda)} | J_{b}^{2} \rangle^{2} = S_{b}$$
(3.39)

thus

$$[H_{ab}]^2 = (\frac{2}{3}) \frac{2}{\Delta \varepsilon} \frac{e^4}{R_{ab}^6} S_a S_b$$
 (3.40)

So

$$[H_{ab}] = (\frac{2}{3})^{1/2} (\frac{2}{\Delta \varepsilon})^{1/2} \frac{e^2}{R_{ab}^3} (S_a S_b)^{1/2}$$
 (3.41)

and

$$[H_{aa}] = (\frac{2}{3})^{1/2} (\frac{2}{\Delta \epsilon})^{1/2} \frac{e^2}{R_{aa}^3} S_a$$

$$[H_{bb}] = (\frac{2}{3})^{1/2} (\frac{2}{\Delta \epsilon})^{1/2} \frac{e^2}{R_{bb}^3} S_b$$
(3.42)

Make the approximation $R_{aa}=R_{bb}=R_{ab}=R$. The average four-body transfer rate is given by:

$$\overline{Y}_{aabb} = \frac{1}{(2J_a+1)^2 (2J_b+1)^2} \left(\frac{4\pi^2}{h}\right) |\langle aabb| \tau | a'a'b'b'\rangle|^2 S$$

$$= \frac{1}{(2J_a+1)^2 (2J_b+1)^2} \left(\frac{4\pi^2}{h}\right) \left(\frac{2}{3}\right)^2 \frac{4}{\Delta \epsilon^2} \frac{e^8}{R^{12}} \qquad (3.43)$$

$$\times (64S_a^3 S_b + 64S_a S_b^3 + 452S_a^2 S_b^2 + 288S_a^{5/2} S_b^{3/2} + 288S_a^{3/2} S_b^{5/2}) S$$

$$= \frac{C_{aabb}}{R^{12}}$$

3.4.2 Energy transfer in a regular distribution of donors and acceptors (Regular model)

We consider a system consisting of two particles, a donor

and an acceptor, in the dipole-dipole approximation, neglecting the exchange term the energy transfer rate is given by [68], [69], [70]:

$$\gamma_{DA} = \frac{C}{R_{DA}^6} = \frac{1}{\tau_D} \left(\frac{R_0}{R_{DA}} \right)^6 \tag{3.44}$$

Where C is the dipole-dipole transfer microparameter, R_{DA} is the distance between the donor and acceptor ions, τ_D is the life time of the donor, and R_0 is the distance at which the transfer rate is equal to the radiative rate. In a system which consists of only one kind of donor and only one kind of acceptor which are distributed among the lattice points of the crystal the basic rate equation for the donors takes the form:

$$\frac{d}{dt}\rho_{i}^{D}(t) = -\rho_{i}^{D}(t)/\tau_{D} - \sum_{j} \gamma_{ij}\rho_{i}^{D}(t) + \dots$$
 (3.45)

where $1/\tau_D$ is the decay rate of the donor, and $\rho_i^D(t)$ is the probability that the ith lattice point is occupied by a donor at time t. In a system which consists of more than one kind of donor or more than one kind of acceptor which are distributed among the doped ions and the doped ions are distributed among the lattice points of the crystal, equation (3.45) becomes:

$$\frac{d\rho_{i}^{D}(t)}{dt} = -\frac{1}{\tau_{D}}\rho_{i}^{D}(t) - \sum_{j=1}^{N_{T}} \gamma_{ij}\rho_{i}^{Ion}\rho_{Ion}^{D}(t)\rho_{j}^{Ion}\rho_{Ion}^{A}(t) + ...$$
 (3.46)

where $\rho_i^D(t) = \rho_i^{Ion} \rho_{Ion}^D(t)$ is the probability that the ith

lattice point is occupied by a donor at time t and $\rho_1^{\Lambda}(t) = \rho_1^{\text{Ton}} \rho_{\text{Ion}}^{\Lambda}(t)$ is the probability that the jth lattice point is occupied by an acceptor at time t separately; ρ_i^{lon} is the probability that the ith lattice point is occupied by an ion and ρ_1^{ton} is the probability that the jth lattice point is occupied by an ion separately; and $\rho_{\text{Ion}}{}^{\text{D}}(t)$ is the probability that the ion which occupies the ith lattice point is occupied by a donor and $\rho_{\text{lon}}^{h}(t)$ is the probability that the ion which occupies the jth lattice point is occupied by an acceptor separately; N_{τ} is the total number of lattice points. To consider the average probability density, we should sum over all the lattice points in the total interaction volume $V_{\mathtt{T}}$ and divide both sides of Equation (3.46) by this volume (for three dimensions) or carry the sum over all the lattice points in the total interaction area S_T and then divide by this area (for two dimensions). Substituting Equation (3.44) into Equation (3.46), we obtain the following expression for the rate equation:

$$\frac{dn_{D}^{(y)}(t)}{dt} = -\frac{1}{\tau_{D}} n_{D}^{(y)}(t) - \frac{1}{L_{T}^{y}} \sum_{i=1}^{N_{T}} \sum_{j=1}^{N_{T}} \frac{C}{R_{ij}^{6}}$$

$$\cdot \rho_{i}^{Ion} \rho_{Ion}^{D}(t) \rho_{i}^{Ion} \rho_{Ion}^{A}(t) + \dots$$
(3.47)

In the above equation we use L_T^y (L_T is the dimension of the interaction volume or area, y=3 or 2) to express V_T or S_T , and

$$n_D^{(y)}(t) = \frac{1}{L_T^y} \sum_{i=1}^{N_T} \rho_i^D(t) = \frac{N_D(t)}{L_T^y}$$
 (3.48)

is the concentration of the donors, where $N_{\scriptscriptstyle D}\left(t\right)$ is the total

number of donors in the region L_T^y . For convenience in the following discussion, we use $n^{(y)}(t)$ to express the y (y=3 or 2) dimensional concentration which has units of L^{-y} , where L is the unit length. From the same considerations we get the rate equation for the acceptors:

$$\frac{dn_A^{(y)}(t)}{dt} = -\frac{1}{\tau_A}n_A^{(y)}(t) - \frac{1}{L_T^y}\sum_{i=1}^{N_T}\sum_{j=1}^{N_T}\frac{C}{R_{ij}^6}\rho_{ion}^{Ion}\rho_{ion}^D(t)\rho_{jon}^{Ion}\rho_{ion}^A(t)^{(3.49)}$$

and for any state M at which the donor or acceptor arrives after the energy transfer process

$$\frac{dn_{M}^{(y)}(t)}{dt} = -\frac{1}{\tau_{M}}n_{M}^{(y)}(t) + \frac{1}{L_{T}^{y}}\sum_{i=1}^{N_{T}}\sum_{j=1}^{N_{T}}\frac{C}{R_{ij}^{6}}\rho_{Ion}^{Ion}\rho_{Ion}^{D}(t)\rho_{j}^{Ion}\rho_{Ion}^{A}(t)^{(3.50)}$$

The general rate equations take the form:

$$\frac{dn_{x}^{(y)}(t)}{dt} = -\frac{1}{\tau_{x}}n_{x}^{(y)}(t) \pm \frac{1}{L_{T}^{y}}\sum_{j=1}^{N_{T}}\sum_{i=1}^{N_{T}}\frac{C}{R_{ij}^{6}}\rho_{Ion}^{Ion}(t)\rho_{j}^{Ion}\rho_{Ion}^{A}(t)^{(3.51)}$$

In the above equation if $n_x^{(y)}(t)$ is the M state ion concentration the sign proceeding the double sum is positive, if $n_x^{(y)}(t)$ is either the donor or the acceptor concentration the sign in front of the double sum is negative.

We now consider a regular distribution of donors and acceptors within a regular distribution of activator ions, such as that which would exist if the activator ions formed a superlattice structure within the crystal. In such a case every configuration of the donors and acceptors would have the same separation between them, and we can choose only one configuration for discussion. For a given configuration only

certain lattice points are occupied by the donors or the acceptors, so in Equation (3.51) we can take $\rho_1^{\text{lon}}\rho_{\text{lon}}^{\text{D}}(t) = \rho_1^{\text{D}}(t) = 1$ for those lattice points which are occupied by a donor and $\rho_1^{\text{lon}}\rho_{\text{lon}}^{\text{D}}(t) = \rho_1^{\text{D}}(t) = 0$ for those lattice points which are not occupied by a donor, and treat $\rho_1^{\text{lon}}\rho_{\text{lon}}^{\text{A}}(t) = \rho_1^{\text{A}}(t)$ in the same way. Equation (3.51) can then be rewritten as:

$$\frac{dn_x^{(y)}(t)}{dt} = -\frac{1}{\tau_x} n_x^{(y)}(t) \pm \frac{1}{L_T^y} \sum_{i=1}^{N_D(t)} \sum_{j=1}^{N_A(t)} \frac{C}{R_{ij}^6} + \dots$$
 (3.52)

where $N_D(t)$, $N_A(t)$ are the total number of donors and acceptors, respectively within the interaction region L_T^{γ} . Note that in Equation (3.52) the double summation refers to the transfer from every donor to every acceptor.

For energy transfer in three dimensions Equation (3.52) takes the form:

$$\frac{dn_{x}^{(3)}(t)}{dt} = -\frac{1}{\tau_{x}} n_{x}^{(3)}(t) \pm \frac{1}{V_{T}} \sum_{i=1}^{N_{D}(t)} \sum_{j=1}^{N_{A}(t)} \frac{C}{R_{ij}^{6}} + \dots
= -\frac{1}{\tau_{x}} n_{x}^{(3)}(t) \pm \frac{1}{V_{T}} N_{D}(T) \sum_{j=1}^{N_{A}(t)} \frac{C}{R_{ij}^{6}} + \dots
= -\frac{1}{\tau_{x}} n_{x}^{(3)}(t) \pm \frac{1}{V_{T}} N_{D}(t) n_{A}(t) \iiint \frac{C}{R^{6}} dV + \dots
= -\frac{1}{\tau_{x}} n_{x}^{(3)}(t) \pm n_{D}(t) n_{A}(t) W^{(3)} + \dots$$
(3.53)

where $W^{(3)}$ is the three dimensional transfer parameter which can be expressed as:

$$W^{(3)} = \iiint \frac{C}{R^6} dV = 4\pi C \int_{d_{nn}}^{d_n} \frac{1}{R^4} dR \approx 4\pi C \int_{d_{nn}}^{\infty} \frac{1}{R^4} dR = \frac{4\pi}{3} \frac{C}{d_{nn}^3}$$
 (3.54)

In the above expression dm is the maximum D-A distance which

is equal to L2, the size of the total interaction volume, and d_{nn} is the average nearest neighbour distance between the donors and acceptors. Since d_m>>d_{nn} we may take d_m from now Within such a regular distribution of donors and on. acceptors the D-A nearest neighbour distance must depend on the donor and acceptor concentrations. We can obtain the this relationship for dependence from the following considerations. If the system consisted only of donors distributed regularly, for a given donor concentration the nearest D-D neighbour distances are all equal. In this case we can treat each donor as a sphere which occupies a volume of $V_{D}(t) = V_{T}/N_{D}(t)$, and the donor-donor nearest neighbour distance is the diameter of this sphere. Similar considerations for a system consisting only of acceptors leads to the acceptoracceptor nearest neighbour distance being given by the diameter of a sphere with volume $V_A(t) = V_T/N_A(t)$. system consisting of both donors and acceptors we can define a sphere which has the average volume of sphere D and sphere **A**:

$$\overline{V}(t) = (V_D(t) V_A(t))^{1/2}
= (\frac{V_T}{N_D(t)} \frac{V_T}{N_A(t)})^{1/2}
= (n_D^{(3)}(t) n_A^{(3)}(t))^{-1/2}$$
(3.55)

and take:

$$\overline{V}(t) = \frac{4\pi}{3} R_{nn}^3 = \frac{\pi}{6} d_{nn}^3$$
 (3.56)

From Equation (3.55) and (3.56) we get:

$$\frac{1}{d_{nn}^{3}} = \frac{\pi}{6} \left(n_D^{(3)}(t) n_A^{(3)}(t) \right)^{1/2}$$
 (3.57)

Equation (3.54) and (3.57) lead to the following expression of the energy transfer parameter:

$$W^{(3)} = \frac{2\pi^2}{9} C(n_D^{(3)}(t) n_A^{(3)}(t))^{1/2}$$
 (3.58)

If, for any reason, the energy transfer is constrained to be planar, with no transfer between planes, Equation (3.52) takes the form:

$$\frac{dn_{x}^{(2)}(t)}{dt} = -\frac{1}{\tau_{x}} n_{x}^{(2)}(t) \pm \frac{1}{S_{T}} \sum_{i=1}^{N_{D}(t)} \sum_{j=1}^{N_{A}(t)} \frac{C}{R_{ij}^{6}} + \cdots$$

$$= -\frac{1}{\tau_{x}} n_{x}^{(2)}(t) \pm \frac{1}{S_{T}} N_{D}(t) \sum_{j=1}^{N_{A}(t)} \frac{C}{R_{ij}^{6}} + \cdots$$

$$= -\frac{1}{\tau_{x}} n_{x}^{(2)}(t) \pm \frac{1}{S_{T}} N_{D}(t) n_{A}^{(2)}(t) \iint \frac{C}{R^{6}} dS + \cdots$$

$$= -\frac{1}{\tau_{x}} n_{x}^{(2)}(t) \pm n_{D}^{(2)}(t) n_{A}^{(2)}(t) W^{(2)} + \cdots$$
(3.59)

where $W^{(2)}$ is the two dimensional transfer parameter which can be written as:

$$W^{(2)} = \iint \frac{C}{R^6} dS = 2\pi C \int_{d_{nn}}^{\infty} \frac{1}{R^5} dR = \frac{\pi}{2} \frac{C}{d_{nn}^4}$$
 (3.60)

As in the three dimensional case d_{nn} is the average nearest neighbour distance between the donor and acceptor which varies with the donor and acceptor concentrations. We can obtain this relationship from the same considerations as for the three dimensional interaction case, but treating circles of area $S_{D,A}=S_T/N_{D,A}(t)$ for donor or acceptor, respectively. Thus

we define a circle with the average area of circle D and circle A

$$\overline{S}(t) = (S_D(t) S_A(t))^{1/2}
= (\frac{S_T}{N_D(t)} \frac{S_T}{N_A(t)})^{1/2}
= (n_D^{(2)}(t) n_A^{(2)}(t))^{-1/2}$$
(3.61)

and take:

$$\overline{S}(t) = \pi R_{nn}^2 = \frac{\pi}{4} d_{nn}^2$$
 (3.62)

From Equation (3.60), (3.61) and (3.62) we obtain the following expression of the two dimensional energy transfer parameter:

$$W^{(2)} = \frac{\pi^3}{32} C n_D^{(2)} (t) n_A^{(2)} (t)$$
 (3.63)

For purposes of comparison it is necessary to transform the two dimensional rate equation (3.59) into a three dimensional form. This can be accomplished by transforming the transfer parameter $W^{(2)}$ as follows:

$$W^{(2)} = \frac{\pi^3}{32} C L^2 n_D^{(3)} (t) n_A^{(3)} (t)$$
 (3.64)

where L is the distance between two adjacent interaction planes, which, for pulsed pump case, is determined by the initial donor concentration from the pump: $(4\pi/3) (L/2)^3 = 1/n^{(3)}_{D(initial)}$. By dividing both sides of Equation (3.59) by L we obtain:

$$\frac{dn_x^{(3)}(t)}{dt} = -\frac{1}{\tau_x} n_x^{(3)}(t) \pm W^{(2)} L n_D^{(3)}(t) n_A^{(3)}(t) + \dots
= -\frac{1}{\tau_x} n_x^{(3)}(t) \pm W^{(3)} n_D^{(3)}(t) n_A^{(3)}(t) + \dots$$
(3.65)

where:

$$W^{(3)} = W^{(2)} L$$

$$= \frac{\pi^3}{32} C L^3 n_D^{(3)} (t) n_A^{(3)} (t)$$

$$= W_{DDAA} n_D^{(3)} (t) n_A^{(3)} (t)$$
(3.66)

Which gives the two dimensional interaction transfer parameters in the three dimensional form. In (3.66)

$$W_{DDAA} = \frac{\pi^3}{32} CL^3 \tag{3.67}$$

is the fourth order transfer parameter.

3.4.3 Four-body model approach to the upconversion dynamics of Er³⁺:YAG and Er³⁺:YAlO₃

Using Equations (3.43) we calculated the four-body transfer rates in the case that all the donor-acceptor distances are treated as the lattice distance (a_y in Tab.1.2). Then we calculated the four-body energy transfer parameters W_{iijj} by (3.32). The values of Ω_{λ} and $\langle J | U^{(\lambda)} | J' \rangle^2$, which were used in the calculation, are from Table 1.5 and 1.6. The value of the overlap integral S was obtained from reference[23] in the case of perfect resonance (S=1/hcv with v=10⁻³ cm⁻¹). The calculated values of W_{iijj} are included in Table 3.13 along with the fitted ones. In this case the calculated values are

Table 3.13 Values of the fourth-order energy transfer parameters obtained in the fittings of the time dependent upconversion emission experimental data of Er³⁺:YAG and Er³⁺:YAlO₃ compared with that calculated from the Judd-Ofelt parameters for the four-body transfer.

	$Er^{3+}:YAG$ $n_Y=1.38\times10^{22} cm^{-3}$, $a_Y=5.17 \ A$		
	Fitted	Calculated	
$C_{1111}(s^{-1}cm^{12})$ $W_{1111}(s^{-1}cm^{9})$	1.35×10 ⁻⁵⁴	4.16×10 ⁻⁸⁷ 4.34×10 ⁻⁶⁶	
$C_{2222} (s^{-1}cm^{12})$ $W_{2222} (s^{-1}cm^{9})$	1.35×10 ⁻⁵⁴	2.00×10 ⁻⁹⁰ 2.09×10 ⁻⁶⁹	
$C_{1122} (s^{-1}cm^{12})$ $W_{1122} (s^{-1}cm^{9})$	5.67×10 ⁻⁵⁴	1.94×10 ⁻⁸⁶ 2.02×10 ⁻⁶⁵	
$C'_{1122} (s^{-1}cm^{12})$ $W'_{1122} (s^{-1}cm^{9})$	2.70×10 ⁻⁵⁶	4.34×10 ⁻⁸⁷ 4.53×10 ⁻⁶⁶	
	$a_{Y}=4.60$	<10 ²² cm ⁻³ ,	
	Fitted	Calculated	
$C_{1111} (s^{-1}Cm^{12})$ $W_{1111} (s^{-1}Cm^{9})$	1.31×10 ⁻⁵⁶	1.28×10 ⁻⁸⁶ 1.89×10 ⁻⁶⁵	
$C_{2222} (s^{-1}cm^{12})$ $W_{2222} (s^{-1}cm^{9})$	1.31×10 ⁻⁵⁶	6.11×10 ⁻⁹⁰ 9.04×10 ⁻⁶⁹	
$C_{1122} (s^{-1}cm^{12})$ $W_{1122} (s^{-1}cm^{9})$	6.55×10 ⁻⁵⁶	6.48×10 ⁻⁸⁶ 1.01×10 ⁻⁶⁴	
C' ₁₁₂₂ (s ⁻¹ cm ¹²) W' ₁₁₂₃ (s ⁻¹ cm ⁹)	8.12×10 ⁻⁵⁵	1.56×10 ⁻⁸⁶ 2.31×10 ⁻⁶⁵	

eight to fifteen orders smaller than the fitted ones.

3.4.4 Regular model approach to the upconversion dynamics of Er³⁺:YAG and Er³⁺:YAlO₃

If the transfer is limited to only two dimensions the energy transfer parameters W_{iijj} in Equation (3.1) are given by Equation (3.67):

$$W_{1111} = \frac{\pi^3}{32} C_{11} L^3$$

$$W_{1122} = \frac{\pi^3}{32} C_{12} L^3$$

$$W'_{1122} = \frac{\pi^3}{32} C'_{12} L^3$$

$$W_{2222} = \frac{\pi^3}{32} C_{22} L^3$$
(3.68)

where C_{ij} is the two-body dipole-dipole microparameters which can be calculated by (1.42) in the case of perfect resonance (S=1/hcv with v=10⁻³ cm⁻¹[23]), L is the distance between two adjacent planes which were obtained by:

$$\frac{4\pi}{3} \left(\frac{L}{2}\right)^3 = \frac{1}{n(1)_{intial}} \tag{3.69}$$

where $n(1)_{initial}=0.04\times4.20\times10^{21}$ cm⁻³ for Er³⁺:YAlO₃ and $n(1)_{initial}=0.043\times1.97\times10^{20}$ cm⁻³ for Er³⁺:YAG. After the above consideration we calculated the energy transfer parameters W_{iijj} which, along with the fitted ones, are listed in Table 3.14. From Table 3.14 we see the calculated transfer parameters are in reasonable agreement with the fitted ones.

Table 3.14 Values of the fourth-order energy transfer parameters obtained from the fittings of the time dependent upconversion emission experimental data of Er³⁺:YAG and Er³⁺:YAlO₃ compared with that calculated from the Judd-Ofelt parameters (for the regular distribution two-body interaction dipole-dipole transfer).

	Er ³⁺ : n(1) _{initial} =8: L ³ =2.56×10 ⁻¹ Fitted	.47×10 ¹⁸ cm ⁻³
$C_{11} (s^{-1}cm^6)$ $W_{1111} (s^{-1}cm^9)$	1.35×10 ⁻⁵⁴	7.87×10 ⁻³⁵ 1.95×10 ⁻⁵³
C_{22} (s ⁻¹ cm ⁶) W_{2222} (s ⁻¹ cm ⁹)	1.35×10 ⁻⁵⁴	3.28×10 ⁻³⁶ 8.12×10 ⁻⁵⁵
C_{12} (s ⁻¹ cm ⁶) W_{1122} (s ⁻¹ cm ⁹)	5.67×10 ⁻⁵⁴	1.81×10 ⁻³⁴ 4.48×10 ⁻⁵³
C' ₁₂ (s ⁻¹ cm ⁶) W' ₁₁₂₂ (s ⁻¹ cm ⁹)	2.70×10 ⁻⁵⁶	7.55×10 ⁻³⁵ 1.87×10 ⁻⁵³
	Er ³⁺ n(1) _{initial} =1 L ³ =1.14×10 ⁻² Fitted	:YAlO ₃ .68×10 ²⁰ cm ⁻³ cm ³ Calculated
C_{11} (s ⁻¹ cm ⁶) W_{1111} (s ⁻¹ cm ⁹)	1.31×10 ⁻⁵⁶	1.32×10 ⁻³⁴ 1.46×10 ⁻⁵⁴
C_{22} (s ⁻¹ cm ⁶) W_{2222} (s ⁻¹ cm ⁹)	1.31×10 ⁻⁵⁶	5.70×10 ⁻³⁶ 6.29×10 ⁻⁵⁶
C_{12} (s ⁻¹ cm ⁶) W_{1122} (s ⁻¹ cm ⁹)	6.55×10 ⁻⁵⁶	3.20×10 ⁻³⁴ 3.53×10 ⁻⁵⁴
C'_{12} (s ⁻¹ cm ⁶) W' ₁₁₂₂ (s ⁻¹ cm ⁹)	.8.12×10 ⁻⁵⁵	1.39×10 ⁻³⁴ 1.53×10 ⁻⁵⁴

The deviations from quadratic concentration dependence noted in reference [58] and [59] for Er³+ concentrations below c.a. 3% and above c.a. 60% (c.f. Figure 5 of Ref.[58]), are also consistent with the model discussed above. To explain this deviation, first we would like to show that if the Er³+ ions are randomly distributed among the lattice points of the crystal and the donors and acceptors are randomly distributed among the Er³+ ions, the transfer term should depend on $n_{\rm D}n_{\rm A}$, or the transfer parameters should be a constant. For the two dimensional interaction case, Equation (3.51) takes the form:

$$\frac{dn_{x}^{(2)}(t)}{dt} = -\frac{1}{\tau_{x}}n_{x}^{(2)}(t) \pm \frac{1}{S_{T}}\sum_{i=1}^{N_{T}}\sum_{j=1}^{N_{T}}\frac{C}{R_{ij}^{6}}\rho_{Er}^{Er}\rho_{Er}^{D}(t)\rho_{j}^{Er}\rho_{Er}^{A}(t)$$
 (3.70)

Since the Er³+ ions are randomly distributed the probability of finding an Er³+ ion at any lattice point is the same as $\rho_i^{Er}=\rho_j^{Er}=N_{TE}/N_T$, where N_{TE} is the total number of Er³+ ions. Since the donors and acceptors are randomly distributed among the Er³+ ions the probability of finding a donor at any Er³+ ion is the same as $\rho_{Er}^{D}(t)=N_D(t)/N_{TE}$ and the probability of finding an

acceptor at any Er³+ ion is also the same as $\rho_{Er}^{\Lambda}(t)=N_{\Lambda}(t)/N_{TE}$, where $N_D(t)$ is the total number of donors and $N_{\Lambda}(t)$ is the total number of acceptors. From the above consideration Equation (3.70) becomes:

$$\frac{dn_{x}^{(2)}(t)}{dt} = -\frac{1}{\tau_{x}}n_{x}^{(2)}(t) \pm \frac{C}{S_{T}} \frac{N_{D}(t)}{N_{T}} \frac{N_{A}(t)}{N_{T}} \sum_{i=1}^{N_{T}} \sum_{j=1}^{N_{T}} \frac{1}{R_{ij}^{6}}$$

$$= -\frac{1}{\tau_{x}}n_{x}^{(2)}(t) \pm n_{D}^{(2)}(t) n_{A}^{(2)}(t) \frac{CS_{T}}{N_{T}^{2}} \sum_{i=1}^{N_{T}} \sum_{j=1}^{N_{T}} \frac{1}{R_{ij}^{6}}$$

$$= -\frac{1}{\tau_{x}}n_{x}^{(2)}(t) \pm n_{D}^{(3)}(t) n_{A}^{(2)}(t) W^{(2)}$$

The transfer parameter of the above equation has the following form:

$$W^{(2)} = \frac{CS_T}{N_T^2} N_T \sum_{j=1}^{N_T} \frac{1}{R_{1j}^6} = \frac{CS_T}{N_T^2} N_T \frac{N_T}{S_T} \iint \frac{1}{R^6} dS$$

$$= :: C \int_{A} \frac{1}{R^5} dR = \pi C \int_{A} \frac{1}{R^5} dR = \frac{\pi}{4} \frac{C}{a^4}$$
(3.72)

where a is the lattice distance. Clearly $W^{(2)}$ does not depend on the activator concentrations.

At low concentrations (<3 %) the distance between donor and acceptor ions is too long so that the inference between the activators is too weak and leads to a semi-random distribution of the donors and acceptors. Since a random distribution of the donors and the acceptors gives a constant transfer parameter (as shown by Equation (3.72)), and an regular distribution of the donors and the acceptors gives a $n_D n_A$ dependence of the transfer parameter (as shown by Equation (3.64). So for a semi-random distribution of the donors and

acceptors the transfer parameter should take the following form:

$$W^{(2)} \propto (n_D^{(3)}(t) n_A^{(3)}(t))^{\gamma_\infty} (n_{TE}^{(3)})^{2\gamma}$$
 (3.73)

where $0<\gamma<1$. If $\gamma=1/2$, the transfer parameter then depends on $(n_pn_a)^{1/2}$ thus depends on the total Er^{3+} concentration linearly.

At high concentrations the reported deviation from quadratic concentration dependence of the transfer parameter , can still be accounted for by the onset of randomization. At total Er3+ concentrations above 50% it is easy to demonstrate that the Er3+ ions can no longer be regularly distributed, which causes the donors and acceptors can not be regularly distributed, thus, according Equation (3.73), leads to a lower power concentration dependence of the transfer parameter. When the total Er3+ concentration exceeds 50% the deformation of the regular distribution increases with total Er3+ the concentration. As the deformation increases the γ (the power of the Er3+ concentration) in Equation (3.73) decreases. This gives a perfect explanation of the experimental curve for c.a. above 60% shown in fig.5 of ref.[58].

The process of energy transfer can destroy the regular distribution. As soon as this balance distribution (we may show that the regular distribution can lead to a minimum repulsive energy between the electron shells of the activators (donor and acceptor ions) in any system, crystal cr liquid) is broken the migration of the excitation takes place to keep the

regular distribution. Since in our case only about 1% of the total Er^{3+} ions are excited by the laser pulse, the excited ions are surrounded by a lot of unexcited ions that can lead to fast migration of the excitation among the Er^{3+} ions.

We have shown that the energy transfer parameter can have functional dependence on the donor and acceptor concentrations when the donors and acceptors are not randomly distributed, but rather are distributed in a arrangement. This is in contrast to the results for a random distribution, which regardless of the spacial arrangement, always requires the interaction of more than two donors and/or acceptors to arrive at such a dependence [53]. The inclusion of these results in a rate equation treatment of the upconversion dynamics of Er3+ in YAlO3 and YAG successfully reproduced the experimental upconversion dynamics over the entire time scale, but only when the energy transfer was restricted to planar (two-dimensional) interactions. While it may be possible to speculate that the energy transfer is indeed constrained to two dimensions because of a combination of polarisation of the pump laser and dipole emission geometric effects (the power radiated by a dipole $\propto \sin^2\theta$ where θ is the angle between the direction of the dipole and the direction of the emission) of the donors, We have not found any supporting evidence for this long-range superlattice structure in these materials. However, This superlattice structure called the was other Suzuki Phase[71],[72] found in some

materials. It will be interesting to see if these materials indeed have a superlattice structure in the range of total doped Er³⁺ concentration between 10% to 50%, and if the results obtained in this work can be successfully applied to energy transfer in materials which are known to have a superlattice structure.

3.4.5 Four-body model approach to the avalanche upconversion dynamics of Tm^{3+} : YLiF₄ and Tm^{3+} : Y₂aF₈.

Using Equations (3.43) and (3.32) we calculated the fourbody energy transfer parameters. The values of Ω_{λ} and $\langle J | U^{(\lambda)} | J' \rangle^2$ used in the calculation were from Table 1.8 and Table 1.9. The value of the overlap integral S was obtained from reference[23] in the case of perfect resonance (S=1/hcV with V=10⁻³ cm⁻¹). The calculated values of W_{iij} are included in Tables 3.15 and 3.16 for $Tm^{3+}:Y_{L}iF_{4}$ and Table 3.17 for $Tm^{3+}:Y_{2}aF_{8}$. From these tables we see that the calculated values are eight to twenty orders smaller than the fitted ones.

Table 3.15 Energy transfer parameters obtained from the Tm^{3+} :YLiF₄ σ polarization fittings compared with those calculated from the Judd-Ofelt parameters (for the four-body transfer). $(n_y=1.39\times10^{22},\ a_y=5.16\ \text{\AA})$

Polarization	(σ)	(σ)	(σ)
λ _{exc} (nm)	627	646	650
Temperature (K)	12	12	300
C ₂₂₂₂ (s ⁻¹ cm ¹²) W ₂₂₂₂ (s ⁻¹ cm ⁹) fitted	5.02×10 ⁻⁸⁷ 9.02×10 ⁻⁵³ 5.26×10 ⁻⁶⁶	5.02×10 ⁻⁸⁷ 9.02×10 ⁻⁵³ 5.26×10 ⁻⁶⁶	5.02×10 ⁻⁸ 2.16×10 ⁻⁵² 5.26×10 ⁻⁶⁶
C ₂₂₃₃ (s ⁻¹ cm ¹²)	1.39×10 ⁻⁸⁶	5.26×10 ⁻⁶⁶ 1.39×10 ⁻⁸⁶	1.39×10 ⁻⁸⁶
W ₂₂₃₃ (S CM) W ₂₂₃₃ (S ⁻¹ CM ⁹) fitted calculated	1.33×10 ⁻⁵¹ 1.46×10 ⁻⁶⁵	1.33×10 ⁻⁵¹ 1.46×10 ⁻⁶⁵	7.94×10 ⁻⁵⁰ 1.46×10 ⁻⁶⁵
C' ₂₂₂₂ (s ⁻¹ cm ¹²) W' ₂₂₂₂ (s ⁻¹ cm ⁹) fitted calculated	2.57×10 ⁻⁸⁶ 8.81×10 ⁻⁵⁴ 2.69×10 ⁻⁶⁵	2.57×10 ⁻⁸⁶ 0 2.69×10 ⁻⁶⁵	2.57×10 ⁻⁸⁶ 9.26×10 ⁻⁵⁴ 2.69×10 ⁻⁶⁵
C ₁₁₄₄ (s ⁻¹ cm ¹²) W ₁₁₄₄ (s ⁻¹ cm ⁹) fitted calculated	1.40×10 ⁻⁸⁷ 0 1.47×10 ⁻⁶⁶	1.40×10 ⁻⁸⁷ 0 1.47×10 ⁻⁶⁶	1.40×10 ⁻⁸⁷ 1.21×10 ⁻⁴⁶ 1.47×10 ⁻⁶⁶

Table 3.16 Energy transfer parameters obtained from the Tm^{3+} :YLiF₄ π polarization fittings compared with those calculated from the Judd-Ofelt parameters (for the four-body transfer). ($n_y=1.39\times10^{22}$, $a_y=5.16$ Å)

Polarization	(π)	(π)	(π)
λ _{exc} (nm)	629	641	654
Temperature (K)	12	12	300
C_{2222} ($s^{-1}cm^{12}$) W_{2222} ($s^{-1}cm^{9}$) fitted calculated	5.02×10 ⁻⁸⁷ 3.89×10 ⁻⁵⁴ 5.26×10 ⁻⁶⁶	5.02×10 ⁻⁸⁷ 3.89×10 ⁻⁵⁴ 5.26×10 ⁻⁶⁶	5.02×10 ⁻⁸⁷ 3.23×10 ⁻⁵² 5.26×10 ⁻⁶⁶
C_{2233} (s ⁻¹ cm ¹²) W_{2233} (s ⁻¹ cm ⁹) fitted calculated	1.39×10 ⁻⁸⁶ 5.46×10 ⁻⁵² 1.46×10 ⁻⁶⁵	1.39×10 ⁻⁸⁶ 7.81×10 ⁻⁵² 1.46×10 ⁻⁶⁵	1.39×10 ⁻⁸⁶ 4.93×10 ⁻⁵⁰ 1.46×10 ⁻⁶⁵
C' ₂₂₂₂ (s ⁻¹ cm ¹²) W' ₂₂₂₂ (s ⁻¹ cm ⁹) fitted calculated	2.57×10 ⁻⁸⁶ 1.11×10 ⁻⁵⁴ 2.69×10 ⁻⁶⁵	2.57×10 ⁻⁸⁶ 2.22×10 ⁻⁵⁴ 2.69×10 ⁻⁶⁵	2.57×10 ⁻⁸⁶ 3.76×10 ⁻⁵³ 2.69×10 ⁻⁶⁵
C ₁₁₄₄ (s ⁻¹ cm ¹²) W ₁₁₄₄ (s ⁻¹ cm ⁹) fitted calculated	1.40×10 ⁻⁸⁷ 1.16×10 ⁻⁴⁹ 1.47×10 ⁻⁶⁶	1.40×10 ⁻⁸⁷ 0 1.47×10 ⁻⁶⁶	1.40×10 ⁻⁸⁷ 7.16×10 ⁻⁴⁸ 1.47×10 ⁻⁶⁶

Table 3.17 Energy transfer parameters obtained from the $Tm^{3+}:Y_2BaF_8$ fittings compared with those calculated from the Judd-Ofelt parameters (for the four-body transfer). $(n_y=1.30\times 10^{22},\ a_y=5.28\ \text{\AA})$

Temperature	12 k	300 k
λ _{exc} (nm)	628.5	628.5
C ₂₂₂₂ (s ⁻¹ cm ¹²)	8.53×10 ⁻⁸⁷	8.53×10 ⁻⁸⁷
W ₂₂₂₂ (S ⁻¹ Cm ⁹)		
Calculated	8.28×10 ⁻⁶⁶	8.28×10 ⁻⁶⁶
Fitted	(4.00±0.22)×10 ⁻⁵⁵	(2.84±0.14)×10 ⁻⁵⁵
C ₂₂₃₃ (s ⁻¹ cm ¹²)	4.20×10 ⁻⁸⁷	4.20×10 ⁻⁸⁷
W ₂₂₃₃ (S ⁻¹ Cm ⁹)		
Calculated	4.07×10 ⁻⁶⁶	4.07×10 ⁻⁶⁶
Fitted	(1.56±1.40)×10 ⁻⁵²	(1.42±0.14)×10 ⁻⁵²
C' ₂₂₂₂ (s ⁻¹ cm ¹²)	1.63×10 ⁻⁸⁶	1.63×10 ⁻⁸⁶
W' 2222 (S ⁻¹ Cm ⁹)		
Calculated	1.58×10 ⁻⁶⁶	1.58×10 ⁻⁶⁶
Fitted	(2.00±0.22)×10 ⁻⁵⁵	(1.31±0.06)×10 ⁻⁵⁵
C ₁₁₄₄ (s ⁻¹ cm ¹²)	8.94×10 ⁻⁸⁸	8.94×10 ⁻⁸⁸
W ₁₁₄₄ (s ⁻¹ cm ⁹)		
Calculated	8.65×10 ⁻⁶⁷	8.65×10 ⁻⁶⁷
Fitted	(2.91±0.76)×10 ⁻⁵²	(2.11±0.59)×10 ⁻⁵²

3.4.6 Regular model approach to the avalanche upconversion dynamics of Tm³⁺:YLiF₄ and Tm³⁺:Y₂Ba₈

We also calculated the energy transfer parameter with the regular model by Equation (3.67) where the transfer microparameter C can be calculated by (1.42) in the case of perfect resonance, and L_{ij} , in the continuous pump case, can be obtained by:

$$\frac{4\pi}{3} \left(\frac{L_{ij}}{2}\right)^{3} = \frac{1}{\sqrt{n(i)n(j)}}$$
 (3.74)

where n(i) and n(j) are obtained by the steady state solutions of Equation (3.5). The calculated the energy transfer parameters W_{iijj} for Tm^{2*} :YLiF₄, along with the fitted ones for both the σ and π polarizations, are listed in Table 3.18 and 3.19, and for Tm^{3*} :Y₂Ba₈ are listed in Table 3.20. From these tables we can see that most of the calculated values are bigger than the fitted values within three orders. The calculated values are expected to be greater than the fitted values because they were calculated under the assumption of perfect resonance, which is certainly not the case -particularly at low temperature. There are several transfer parameters with calculated values smaller than the fitted values. This may be caused by the treatment of the distance between two adjacent interaction planes L_{ij} by (3.74).

Table 3.18 Energy transfer parameters obtained from the σ polarization fitting compared with those calculated from the Judd-Ofeld parameters (for the regular distribution two-body interaction dipole-dipole energy transfer).

 $n_{\rm Tm} = 1.98 \times 10^{20} \ {\rm cm}^{-3}$

Polarization	(σ)	(o)	(σ)
λ _{exc} (nm)	627	646	650
Temperature(K)	12	12	300
n(0)/n _{Tm}	0.99	0.96	0.99
n(1)/n _{Tm}	3.99×10 ⁻³	2.71×10 ⁻²	3.23×10 ⁻³
n(2)/n _{Tm}	3.76×10 ⁻³	5.21×10 ⁻³	2.37×10 ⁻³
n(3)/n _{rm}	4.62×10 ⁻⁴	3.03×10 ⁻³	1.88×10 ⁻⁴
n(4)/n _{Tm}	3.85×10 ⁻⁶	1.45×10 ⁻⁴	3.04×10 ⁻⁶
C_{22} (s ⁻¹ cm ⁶) W_{2222} (s ⁻¹ cm ⁹)	9.38×10 ⁻³⁵	9.38×10 ⁻³⁵	9.38×10 ⁻³⁵
calculated fitted	2.33×10 ⁻⁵² 9.02×10 ⁻⁵³	1.68×10 ⁻⁵² 9.02×10 ⁻⁵³	3.70×10 ⁻⁵² 2.16×10 ⁻⁵²
C_{23} (s ⁻¹ cm ⁶) W_{2233} (s ⁻¹ cm ⁹)	1.60×10 ⁻³⁴	1.60×10 ⁻³⁴	1.60×10 ⁻³⁴
calculated fitted	1.13×10 ⁻⁵¹ 1.33×10 ⁻⁵¹	3.76×10 ⁻⁵² 1.33×10 ⁻⁵¹	2.24×10 ⁻⁵¹ 7.94×10 ⁻⁵⁰
C' ₂₂ (S ⁻¹ Cm ⁶) W' ₂₂₂₂ (S ⁻¹ Cm ⁹)	3.76×10 ⁻³⁴	3.76×10 ⁻³⁴	3.76×10 ⁻³⁴
calculated fitted	9.34×10 ⁻⁵² 8.81×10 ⁻⁵⁴	6.74×10 ⁻⁵²	1.48×10 ⁻⁵¹ 9.26×10 ⁻⁵⁴
C ₁₄ (s ⁻¹ cm ⁶) W ₁₁₄₄ (s ⁻¹ cm ⁹)	3.91×10 ⁻³⁵	3.91×10 ⁻³⁵	3.91×10 ⁻³⁵
calculated fitted	2.95×10 ⁻⁵¹	1.84×10 ⁻⁵²	3.68×10 ⁻⁵¹ 1.21×10 ⁻⁴⁶

Table 3.19 Energy transfer parameters obtained from the π polarization fitting comparing with those calculated from the Judd-Ofeld parameters (for the regular distribution two-body interaction dipole-dipole transfer).

 $n_{\rm Tm} = 1.98 \times 10^{20} \, {\rm cm}^{-3}$

 $V_{i,j}$

II _{Im} -1.96XIO CIII	<u>. </u>		
Polarization	(π)	(π)	(π)
λ _{exc} (nm)	629	641	654
Temperature (K)	12	12	300
n(0)/n _{Tm}	0.98	0.98	0.99
n(1)/n _{Im}	1.51×10 ⁻²	8.03×10 ⁻³	4.79×10 ⁻³
n(2)/n _{Tm}	6.61×10 ⁻³	5.51×10 ⁻³	2.49×10 ⁻³
n(3)/n _{Tm}	2.14×10 ⁻³	1.51×10 ⁻³	2.12×10 ⁻⁴
$n(4)/n_{Tm}$	4.70×10 ⁻⁵	5.14×10 ⁻⁵	6.25×10 ⁻⁶
C ₂₂ (s ⁻¹ cm ⁶)	9.38×10 ⁻³⁵	9.38×10 ⁻³⁵	9.38×10 ⁻³⁵
W ₂₂₂₂ (s ⁻¹ cm ⁹) calculated	1.32×10 ⁻⁵²	1.59×10 ⁻⁵²	3.52×10 ⁻⁵²
fitted	3.89×10 ⁻⁵⁴	3.89×10 ⁻⁵⁴	3.23×10 ⁻⁵²
C ₂₃ (s ⁻¹ cm ⁶)	1.60×10 ⁻³⁴	1.60×10 ⁻³⁴	1.60×10 ⁻³⁴
W ₂₂₃₃ (s ⁻¹ cm ⁹) calculated	3.97×10 ⁵²	5.18×10 ⁻⁵²	2.06×10 ⁻⁵¹
fitted .	5.46×10 ⁻⁵²	7.81×10 ⁻⁵²	4.39×10 ⁻⁵⁰
C' ₂₂ (s ⁻¹ cm ⁶)	3.76×10 ⁻³⁴	3.76×10 ⁻³⁴	3.76×10 ⁻³⁴
W' ₂₂₂₂ (s ⁻¹ cm ⁹) calculated	5.31×10 ⁻⁵²	6.37×10 ⁻⁵²	1.41×10 ⁻⁵¹
fitted	1.11×10 ⁻⁵⁴	2.22×10 ⁻⁵⁴	3.76×10 ⁻⁵³
C ₁₄ (s ⁻¹ cm ⁶)	3.91×10 ⁻³⁵	3.91×10 ⁻³⁵	3.91×10 ⁻³⁵
W ₁₁₄₄ (s ⁻¹ cm ⁹) calculated	4.33×10 ⁻⁵²	5.68×10 ⁻⁵²	2.11×10 ⁻⁵¹
fitted	1.16×10 ⁻⁴⁹	0	7.16×10 ⁻⁴⁸

Table 3.20

Energy transfer parameters obtained from the $Tm^{3+}:Y_2BaF_8$ fittings compared with those calculated from the Judd-Ofelt parameters (for the regular distribution two-body interaction dipole-dipole energy transfer). ($n_{Tm}=6.50\times10^{20}$)

Temperature	12 k	300 k
λ _{exc} (nm)	628.5	628.5
C ₂₂ (s ⁻¹ cm ⁶) W ₂₂₂₂ (s ⁻¹ cm ⁹) Calculated Fitted	8.38×10 ⁻⁵³ (4.00±0.22)×10 ⁻⁵⁵	1.25×10 ⁻³⁴ 7.40×10 ⁻⁵³ (2.84±0.14)×10 ⁻⁵⁵
C ₂₃ (s ⁻¹ cm ⁶) W ₂₂₃₃ (s ⁻¹ cm ⁹) Calculated Fitted	8.82×10 ⁻³⁵ 1.57×10 ⁻⁵² (1.56±1.40)×10 ⁻⁵²	8.82×10 ⁻³⁵ 1.89×10 ⁻⁵² (1.42±0.14)×10 ⁻⁵²
C' ₂₂ (s ⁻¹ cm ⁶) W' ₂₂₂₂ (s ⁻¹ cm ⁹) Calculated Fitted	2.89×10 ⁻³⁴ 1.94×10 ⁻⁵² (2.00±0.22)×10 ⁻⁵⁵	2.89×10 ⁻³⁴ 2.00×10 ⁻⁵² (1.31±0.06)×10 ⁻⁵⁵
C ₁₄ (s ⁻¹ cm ⁶) W ₁₁₄₄ (s ⁻¹ cm ⁹) Calculated Fitted	2.29×10 ⁻³⁵ 1.22×10 ⁻⁵² (2.91±0.76)×10 ⁻⁵²	2.29×10 ⁻³⁵ 2.14×10 ⁻⁵² (2.11±0.59)×10 ⁻⁵²

3.5 Discussions

3.5.1. About the many-body interaction

From Table 3.13, 3.15, 3.16, 3.17 we see that in all cases the calculated values of the fourth order energy transfer parameters W_{iij1} obtained from the four-body interaction transfer model are 10^8 to 10^{20} smaller than the fitted values. Also, the Judd-Ofelt parameter calculations for the three-body interaction yield energy transfer rates about 108 times smaller than the two-body transfer rate[23]. It is clear that the high order concentration dependence energy transfer kinetics cannot be accounted for by the many-body interaction transfer. In fact, the many-body interaction energy transfer requires a many-body electric interaction force which does not exist. As we can see, the two-body transfer rate given by Eq. (1.37) comes from the two-body interaction Hamiltonian $H_{AB} = \Sigma e^2/r_{st}$ given by Eq.(1.15). The repulsive energy between two electrons e2/r in this two-body interaction Hamiltonian arrives from the two-body electric interaction force $f=e^2/r_{st}^2$. The many-body transfer rate comes from the Hamiltonian given by the form HABHAC, for instance the three-body transfer rate given by Eq.(1.87) comes from the Hamiltonian that takes the form:

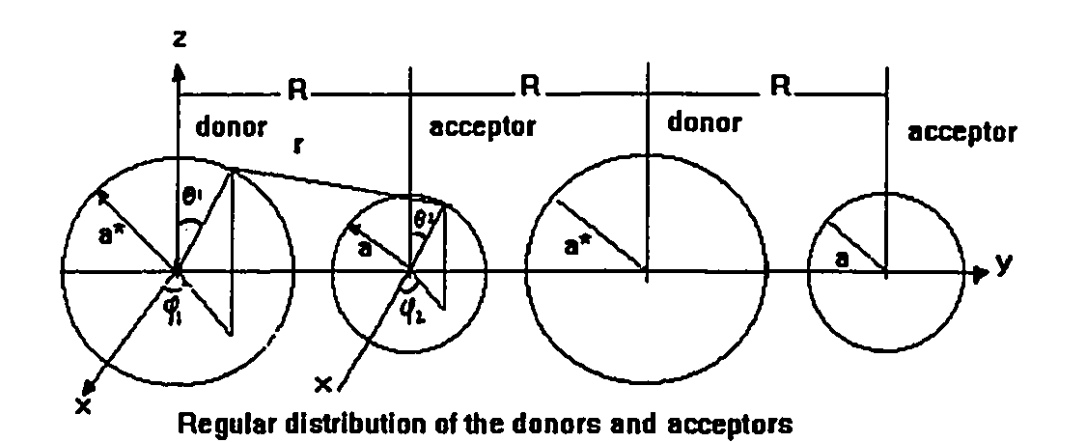
 $H'_{DA1}H'_{DA2} = (e^4/k^2R_{DA1}^3R_{DA2}^3) \, \mathbf{r}_D \cdot \mathbf{T} \, (DA_1) \cdot \mathbf{r}_{A1} \, \mathbf{r}_D \cdot \mathbf{T} \, (DA_2) \cdot \mathbf{r}_{A2}$ The physical meaning of this Hamiltonian is that there must exist a three-body electric interaction force that takes the form: $f_{DA1A2} = (e_D^2 e_{A1} e_{A2}) / (k^2 R_{DA1}^2 e_{DA1}^2)$, otherwise this process cannot

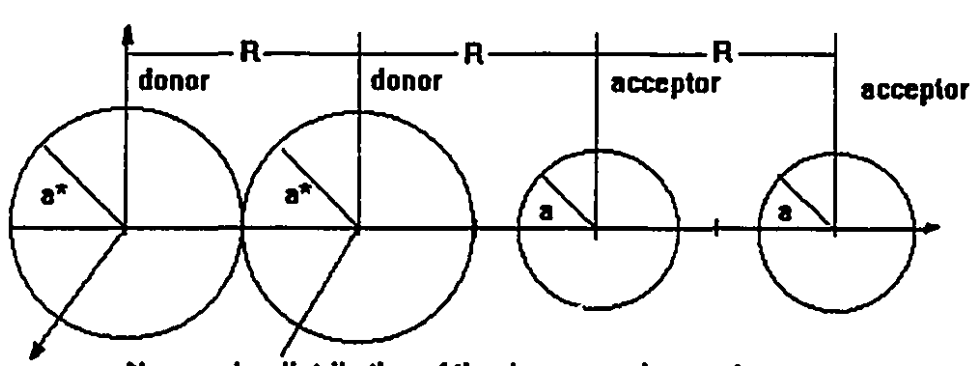
happen because the possibility that two events (the donor D transfers energy to the acceptors A_1 and A_2) happen exactly at the same time is zero. Since among the four basic interaction forces (the gravity interaction force, the electromagnetic interaction force, the strong interaction force, and the weak interaction force) up to date there is no report for the discovery of a many-body interaction force. This is the reason why the many-body interaction energy transfer model can not fit the experimental data.

3.5.2. About the regular distribution of the donors and acceptors

From Tables 3.14, 3.18, 3.19 and 3.20 we see that in all the cases of our research the calculated values of the fourth order energy transfer parameters obtained from the regular and two dimension transfer model are in reasonable agreement with the fitted values. What causes the donors and acceptors to be distributed regularly? The following gives a possible reason.

The regular distribution of the donors and acceptors (the same ions in different states) may be caused by the different magnitude of the repulsive force between different activator's electron shells. If we treat the electrons of an ion as a shell and suppose that the diameter of the donor's electron shell is bigger than that of the acceptor's electron shell as shown by Figure 3.24, and if the donor and acceptor are separated by a distance R, then the repulsive energy between





Nonregular distribution of the donors and acceptors

Figure 3.24

the donor's shell and the acceptor's shell is the following:

$$U_{D,A} = \sigma_D \sigma_A \iiint \frac{ds_D ds_A}{r}$$
 (3.75)

where σ_D and σ_A are the charge densities of the electron shells of the donor ion and the acceptor ion, r is the distance between any two points on the two electron shells. In Equation (3.75) we have:

$$\sigma_{D} = \frac{Ne}{4\pi a^{*2}}$$

$$\sigma_{A} = \frac{Ne}{4\pi a^{2}}$$

$$r = [(a\sin\theta_{2}\cos\phi_{2} - a^{*}\sin\theta_{1}\cos\phi_{1})^{2} + (R^{*}a\sin\theta_{2}\sin\phi_{2} - a^{*}\sin\theta_{1}\cos\phi_{1})^{2} + (a\cos\theta_{2} - a^{*}\cos\theta_{1})^{2}]^{1/2}$$

$$ds_{D} = a^{*2}\sin\theta_{1}d\theta_{1}d\phi_{1}$$

$$ds_{A} = a^{2}\sin\theta_{2}d\theta_{2}d\phi_{2}$$
(3.76)

where N is the number of electrons of the donor or acceptor. If we put Eq. (3.76) into (3.75), we obtain:

$$U_{D,A} = \frac{(Ne)^2}{16\pi^2} \iiint \frac{\sin\theta_1 d\theta_1 d\phi_1 \sin\theta_2 d\theta_2 d\phi_2}{r}$$
(3.77)

Since under normal donor and acceptor concentrations a* and a << R, therefor in Eq. (3.77) we can make the following approximation:

$$\frac{1}{r} \frac{1}{R[1 + \frac{2}{R}(a \cdot \sin\theta_1 \sin\phi_1 - a\sin\theta_2 \sin\phi_2)]^{1/2}}$$

$$\approx \frac{1}{R} \left[1 - \frac{1}{R}(a \cdot \sin\theta_1 \sin\phi_1 - a\sin\theta_2 \sin\phi_2) + \frac{3}{R}(a \cdot \sin\theta_1 \sin\phi_1 - a\sin\theta_2 \sin\phi_2)^2\right]$$
(3.78)

Put Eq. (3.78) into Eq. (3.77) we obtain:

$$U_{D,A} = \frac{N^2 e^2}{4\pi \epsilon_o R} \left[1 + \frac{3}{8} \frac{(a^{*2} + a^2)}{R^2} \right]$$
 (3.79)

For the same consideration we obtain the repulsive energy between two donors which are separated by the same distance R:

$$U_{D,D} = \frac{N^2 e^2}{4\pi \epsilon_{\sigma} R} \left[1 + \frac{3}{8} \frac{(a^{*2} + a^{*2})}{R^2} \right]$$
 (3.80)

The difference of the repulsive energy between two donors and the repulsive energy between a donor and an acceptor is:

$$\Delta U = U_{D,D} - U_{D,A}$$

$$= \frac{3}{32} \frac{N^2 e^2}{\pi \epsilon_o} \frac{(a^{*2} - a^2)}{R^3}$$

$$= \frac{3}{32} \frac{N^2 e^2}{\pi \epsilon_o} \frac{(a^{*+} + a)(a^{*-} - a)}{R^3}$$
(3.81)

If we take a'+a=4Å, a'-a=0.1Å, N=65 and R=20Å (the nearest neighbour distance between the excited Er³+ ions in the Er³+:YAlO₃ when 1% of the doped Er³+ ions are excited) we get $\Delta U\approx 10^{-19} J$. Compared with the thermal energy which at room temperature is about $10^{-21} J$, this difference of the repulsive energy can not be neglected. It is this difference that makes the donors distribute regularly rather than randomly. This can also be explained as the follows: The total repulsive energy between the electron shells of a donor acceptor system take the form:

$$U_{T} = \frac{1}{2} \sum_{i=1}^{N_{T}} \sum_{j=1}^{N_{T}} \frac{N^{2}e^{2}}{4\pi\epsilon_{0}} \frac{1}{R_{ij}} + \frac{1}{2} \sum_{i=1}^{N_{T}} \sum_{j=1}^{N_{T}} \frac{3}{32} \frac{N^{2}e^{2}}{\pi\epsilon_{0}} \frac{(a_{i}^{2} + a_{j}^{2})}{R_{ij}^{3}}$$

$$= U_{m} + U_{m}$$
(3.82)

where $N_T=N_D+N_A$, and N_D is the number of donors and N_A is the number of acceptors. In the above equation $a_{i,j}$ equals a^* if the i^{th} or j^{th} ion is a donor ion, and $a_{i,j}$ equals a if the i^{th} or j^{th} ion is an acceptor ion. Clearly, the U_{T1} dose not depend on the distribution of the donors and acceptors but the U_{T2} dose. It is not difficult to understand from Equation (3.82) that when the donors and acceptors are regularly distributed, U_{T2} reaches a minimum. Because a balance distribution requires the lowest interaction energy, this leads to the regular distribution of the donors and acceptors.

3.5.3. About the two-dimension transfer

How are the energy transfer processes limited to a plane? The following gives one explanation. In our research, the pumping laser beam is polarized. As shown in Figure 3.25, the

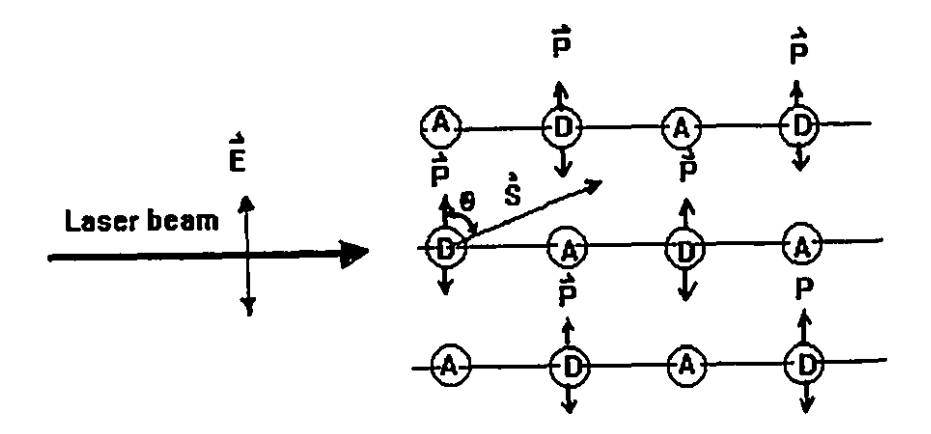


Figure 3.25

electric field of the laser beam induces all the ion's dipoles vibrate in the same direction as that of the electric field of the laser beam. From the general theory of electron dynamics the dipole energy emission obeys the following equation

$$S(\theta) = \frac{\omega^4 P_0^2}{4\pi c^3 r_0^2} \sin^2 \theta$$
 (3.83)

where $S(\theta)$ is the density of the emission energy flux and θ is the angle between the direction of emission and the direction of the dipole. Since at $\theta=0^\circ$ there is no emission and at $\theta=90^\circ$ the emission is maximum, and since the energy of a donor is transferred mainly to the nearest neighbour acceptors (because the transfer rate is proportional to $1/R_{DA}^{-6}$), therefor, the energy is transferred mainly between the nearest ions on the same interaction plane.

3.5.4 The influence of the energy transfer parameters by structure of the compounds.

From Eq.(1.37) and (1.38) we can see that the energy transfer rate γ_{AB} is determined by the D-A distance R and the microtransfer parameter $C^{(6)}$. The microtransfer parameter $C^{(6)}$ is determined by the dipole element $[\Sigma|\langle a'|D^1_m|a\rangle|^2] \cdot [\Sigma|\langle b'|D^1_m|b\rangle|^2]$ and the overlap integral S. From Eq.(1.42) we see that the dipole element is determined by the intensity parameters Ω_{λ} and the matrix elements $U^{(\lambda)}$. From Eq.(1.33) we see that the overlap integral S is determined by the resonance of the energy transfer $(\nu_{\lambda}-\nu_{B})$. In the following we will show

10

that the structure of the compounds has an influence on the matrix elements $U^{(\lambda)}$ and the resonance ν_A - ν_B thus the transfer rate.

- a). Different compounds or different crystal structure have different crystal fields. Since the matrix elements $U^{(\lambda)}$ and the energy level splitting of the doped ion are affected by the symmetry and magnitude of the crystal field, any change in the structure will 1) changes the matrix elements $U^{(\lambda)}$ and thus the transfer rate γ_{AB} and 2) changes the energy level structure of the doped ion and thus changes the resonance mismatch $(V_A V_B)$ and thus the transfer rate γ_{AB} .
- b). Different compounds or different crystal structure have different phonon energy. This phonon energy compensates for the resonance mismatch $(\mathbf{V}_A \mathbf{V}_B)$ of the transfer process. At low temperature this phonon assistance is not important but at room temperature it gains importance.

3.5.5 Analysis of the parameters

a). Tm3+:YLiF4

The resonance mismatch for the energy transfer processes are listed in Table 3.21.

Table 3.21

	W ₂₂₂₂	W ₂₂₃₃	W′ 2222	W ₁₁₄₄
$(V_A - V_B)$ (cm ⁻¹)	1	12	218	291

From Table 3.8 we can see that at 12 K the fitted values of $W_{1:44}$ are zero, consistent with the lack of resonance ($v_A - v_B = 291 \text{ cm}^{-1}$) and the values of $W'_{2:2:2}$ are small or zero also because of large mismatch ($v_A - v_B = 218 \text{ cm}^{-1}$). From Table 3.8 and 3.9 we see that all the fitted room temperature (300 k) parameters $W_{1:1:1}$ are bigger than the corresponding low temperature (12 K) values, which is because the resonance mismatch can be compensated by phonons at room temperature.

b. Er3+: YAG and Er3+: YAlO3

The resonance mismatch of the transfer processes are given in Table 3.22.

Table 3.22

	W ₁₁₁₁	W ₁₁₂₂	W' 1122	W ₂₂₂₂
(V _A - V _B) (cm ⁻¹) Er ³⁺ :YALO ₃	5	887	8	1561
(V _A - V _B) (cm ⁻¹) Er ³⁺ :YAG	213	924	30	1470

From Table 3.2 we see that the parameters W_{2222} for both Er^{3+} :YALO₃ and Er^{3+} :YAG are the same as W_{1111} even though the resonance for W_{2222} is much worse. This may be due to the phonon assistance of the W_{2222} processes (for Er^{3+} :YALO₃ the phonon energy is 600 cm⁻¹ and the energy of three phonons is close to the energy mismatch, while for Er^{3+} :YAG the phonon energy is 700 cm⁻¹ and the energy of two phonos is close to the energy mismatch).

CHAPTER 4

CONCLUSIONS AND SUMMARY OF THE

CONTRIBUTIONS TO THE KNOWLEDGE

4.1 Conclusions

In this work we have examined existing data for the upconversion dynamics of Er^{3+} in two different oxide hosts, YAG and YAlO₃, and new data for Tm^{3+} in two different fluoride hosts, YLiF₄ and Y₂BaF₈. From this work we may conclude that:

- 1. At low donor-acceptor concentrations (low excitation intensity), the energy transfer kinetics is second order, and at high donor-acceptor concentrations (high excitation intensity), the energy transfer kinetics is fourth order.
- 2. The general form of the energy transfer term in the rate equations should take the form:

$$W_f(n_D(t) n_A(t))^{f(nD(t),nA(t))}$$

where $f(n_D(t), n_A(t))$ is a continuous function of $n_D(t)$ and $n_A(t)$, and $1 < f(n_D(t), n_A(t)) \le 2$. At low donor and acceptor concentrations $f(n_D(t), n_A(t)) \to 1$ and W_f is given by Eq.(1.51). At high donor and acceptor concentrations $f(n_D(t), n_A(t)) = 2$ and W_f is given by Eq.(3.67).

- 3. The high order (higher than two) concentration dependence of the energy transfer term can only come from the two-body interaction transfer, not from the many-body interaction transfer.
- 4. The fourth order energy transfer kinetics may come from a regular distribution of the donors and acceptors and two-dimensional transfer.
- 5. At low pump power there is a photon avalanche which is caused by the cross relaxation process W_{30} . At high pump power

the avalanche process stops, and the delay of the rise time as shown by Figure 3.12 is caused by the fourth order kinetics of the other energy transfer processes shown in Figure 3.7.

4.2 Summary of the contributions to the knowledge

- 1. Experimental evidence is presented for the first time indicating that under conditions of low donor and acceptor concentrations energy upconversion occurs via second order energy transfer kinetics and under conditions of high activator concentrations energy upconversion occurs via fourth order energy transfer kinetics.
- 2. A new energy transfer model based on regular distribution of donors and acceptors for two-dimension transfer is developed in this work which can lead to fourth order energy transfer terms.
- 3. Kinetic models are given which adequately describe the upconversion dynamics for Er^{3+} :YAlO₃, Er^{3+} :YAG, and for the avalanche upconversion dynamics for Tm^{3+} :YLiF₄ and Tm^{3+} :Y₂BaF₈.
- 4. The existing three-body interaction energy transfer model obtained from the second order perturbation is extended to the case of four-body interaction.
- 5. Existing methods utilizing Judd-Ofelt parameters to estimate the energy transfer rates for two body dipole-dipole interactions are extended to the case of the four body dd-dd interactions invoked in this work.
 - 6. Pump-probe gain measurements are reported for the

first time for $Tm^{3+}: Y_2BaF_8$, and an unusual temperature dependence for one of the lines is discussed.

4.3 Suggestions for future work

- 1. Detailed investigation of the concentration dependence of the energy transfer parameters, over a wide range of concentrations and pump power to determine the range of activator concentrations for which fourth order kinetics are valid.
- 2. Study of energy transfer in the liquid state, if possible, would be very helpful in verifying some of the ideas put forward in this work.
- 3. Theoretical investigations of other possible models which can obtain fourth order energy transfer term from two-body interaction.
- 4. Detailed theoretical justification for the regular distribution of the donors and acceptors and two-dimension transfer.

APPENDIX

1. Error analysis

The errors of a fitted parameter Δa_i in all the models are calculated by the following equation:

$$\Delta a_i = \pm \sqrt{\Delta \chi_v^2} \sqrt{C_{ii}}$$

where $\Delta \chi_{\nu} = \chi_{\nu}^2 - \chi_{\min}^2$ and:

$$\frac{1}{C_{kl}} = \alpha_{kl} = \frac{\partial^2 \chi^2}{\partial a_k \partial a_l}$$

and:

$$\chi^{2}(a_{1}, a_{2}, ...) = \sum_{i=1}^{N} \left[\frac{y_{i} - y(x_{i}, a_{1}, a_{2}, ...)}{\sigma_{i}} \right]^{2}$$

In all the error estimatings, we take the measurement errors σ_i =1, and $\Delta\chi_v$ (v=1)=4 (95.4% confidence level). The sensitivity of the parameters are determined by the magnitude of the errors.

2. Assumptions in the energy transfer models

All the current energy transfer models are based on the assumption that the donors and acceptors are randomly distributed among the lattice points of the crystal. According to this assumption the nearest neighbour distance is not dependent on the donor and acceptor concentrations and is always the lattice distance.

The regular model presented in this thesis is based on the assumption that the donors and acceptors are regularly distributed in the system (crystal, or liquid) at high donor and acceptor concentrations and the distribution changes from regular towards random as the donor and acceptor concentrations decrease. According to this assumption, when the donors and acceptors are regularly distributed the nearest neighbour distance between the donors and acceptors is dependent on the concentrations of the donor and acceptor $d_{nn} \approx 1/\left(n_{p}n_{A}\right)^{1/6}$.

REFERENCES

- [1] S. Hüfner, "Optical Spectra of Transparent Rare Earth Compounds". ACADEMIC PRESS New York, San Francisco, London, 1978.
- [2] G. H. Dieke, "Spectra and Energy Levels pf Rare Earth Ions in Crystals", edited by H. M. Crosswhite and Hannah Crosswhite, Interscience Publishers, (1968).
- [3] Alexander A. Kaminskii (ed.), "Laser Crystals", Springer Series in Optical Science, Vol.14, P.12-15.
- [4] Chim. Miner., 21, 771, (1984).
- [5] Sov. Pnys. Crystallogr., 15, 496, (1970).
- [6] J. A. Koningstein and J. E. Geusic, Phys. Rev., Vol. 136, No. 3A, A726-728.
- [7] Vincent L. Donlan and Abraham A. Santiago, J. Chem. Phys. 57, 4717, (1972).
- [8] M. Dulick, G. E. Faulkner, N. J. Cockroft and D. C. Nguyen, J. Lumin. 48 & 49, 517-521, (1991).
- [9] E. U. Condon, G. H. Shortley: The Theory of Atomic Spectra (Cambridge University Press, Cambridge 1957).
- [10] J. H. van Vleck, J. Phys. Chem. 41, 67 (1937).
- [11] B. R. Judd, Phys. Rev. 127, 750 (1962).
- [12] G. S. Ofelt, J. Chem. Phys., 37, 511 (1962).
- [13] Q. Y. Wang, S. Y. Chang, S. X. Wu, Y. Ren and X. M. Dong, ACTA OPTICAL SINICA, P.R. CHINA, 6, 307 (1986).
- [14] M. J. Weber, Phys. Rev. 157, 262, (1967).
- [15] W. T. Carnall, P. R. Fields, and K. Rajnak, J. Chem. Phys. 49, 4424, (1968).
- [16] B. M. Antipenko, Opt. Spectrosc. (USSR), 56, 44-48 (1984).

- [17] Nissan CPECTOR and, R. Reisfeld and L. Boehm, Chem. Phys. Lett. 49, 49, (1977).
- [18] Föster, T.: Ann. Phys. 2, 55 (1948).
- [19] Föster, T.: Z. Naturforsch. A4, 321 (1949).
- [20] Dexter, D. L.: J. Chem. Phys. 21, 836 (1953).
- [21] Baldesare Di Bartolo (ed.), "Energy Transfer Processes in Condensed Matter"'NATO ASI Seiries B: Physics, Vol. 114, 1984' Plenum Press, New York.
- [22] B. C. Carlson and G. S. Rushbrooke, Proc. Camb. Phil. Sco. **46**, 626 (1950).
- [23] Kushida, T, J. Phys. Sco. Japan 34, 1318, 1327 and 1334 (1973).
- [24] L. F. Johnson and H. J. Guggenhein, Appl. Phys. Lett. 19, 44 (1971).
- [25] M. E. Koch, A. W. Kueny, and W. E. Case, Appl. Phys. Lett. 56, 1083 (1990).
- [26] R. G. Smart, D. C. Hanna, A. C. Tropper, S. T. Davey, S. F. Carter, and D. Szebesta, Conference on Lasers and Electro-Optics (CLEO-91) Technical Digest, American Optics Society, 1991, Post-deadline Paper CODP13-2.
- [27] R. M. Macfarlane, F. Tong, A. J. Silversmith, and W. Lenth, Appl. Phys. Lett. 52, 1300 (1988).
- [28] R. M. Macfarlane, A. J. Silversmith, F. Tong, and W. Lenth, Proceedings of the International Conference on laser Science and Laser Materials, Shanghai, July 25-27, 1988, edited by Z. J. Wang and Z. M. Zhang (World Scientific, Singapore, 1989). p.24.
- [29] J. Y. Allain, M. Monerie, and H. Poignant, Electron Lett. 26, 261 (1990).
- [30] A. J. Silversmith, W. Lenth, and R. M. Macfarlane, J. Opt. Soc. Am. A3, P128 (1986); A. J. Silversmith, W. Lenth, and R. M. Macfarlane, Appl. Phys. Lett. 51, 1977 (1987).
- [31] B. M. Antipenko, S. P. Voronin, and T. A. Privalova, Sov. Phys. Tech. Phys. 32, 208 (1978).

- [32] W. Lenth, A. J. Silversmith, and R. M. Macfarlane, Advances in Laser Science III, edited by A. C. Tam, J. L. Gole, and W. C. Stwalley [AIP Conf. Proc. 172, 8 (1987)].
- [33] R. A. McFarlane, Appl. Phys. Lett. 54, 2301 (1989).
- [34] R. A. McFarlane, M. Robinson, and S. A. Pollack, Proc. SPIE 1223, 294 (1990).
- [35] T. Hebert, R. Wannemacher, W. Lenth, and R. M. Macfarlane, Appl. Phys. Lett. 57, 1727 (1990).
- [36] T. Hebert, W. P. Risk, R. M. Macfarlane, and W. Lenth, Advanced Solid State Lasers, edited by H. P. Jenssen and G. Dube, Opt. Soc. Am., Washington DC, 1990, P.379.
- [37] D. C. Nguyen, G. E. Faulkner, and M. Dulick, Appl. Opt. 28, 3553 (1989).
- [38] D. C. Nguyen, G. E. Faulkner, M. E. Weber, and M. Dulick, Proc. SPIE 1223, 54 (1990).
- [39] R. M. Macfarlane, R. Wannemacher, T. Hebert, and W. Lenth, Conference on Lasers and Electro-optics (CLEO-90) Technical Digest, American Optics Society, F.250.
- [40] F. E. Auzel, Compt. Rend. 262, 1016 (1966).
- [41] V. V. Ovsyankin and P. P. Feofilov, Sov. Phys. JETP Lett. 3, 317 (1966).
- [42] Mario Yokota and Osamu Tanimoto, J. Phys. Soc. Japan, 22, 3 (1967)
- [43] A. l. Burshtein, Sov. phys. Usp. 27 (8), (1984).
- [44] Gochanour, Andersen, and Fayer: J. Chem. Phys. 70, 9 (1979).
- [45] Steven W. Haan and Robert Zwanzig, J. Chem. Phys. 68, 4 (1978).
- [46] D. L. Huber: Phys. Rev. **B20**, 12 (1979).
- [47] Jay S. Chivian, W. E. Case, and D. D. Eden, Appl. Phys. Lett. 35, 124 (1979).
- [48] N. J. Krasutsky, J. Appl. Phys. 54, 1261 (1983).

- [49] W. Lenth and R. M. Macfarlane, J. Lumin. 45, 346 (1990).
- [50] T. Hebert, R. Wannemacher, R. M. Macfarlance, and W. Lenth, Appl. Phys. Lett. 60, 2592 (1992).
- [51] H. Ni and S. C. Rand, Opt. Lett. 16, 1424 (1991).
- [52] M. F. Joubert, S. Guy, and B. Jacquier, Phys. Rev. B 48, 10031-10037, (1993).
- [53] Walter J. C. Grant, Phys. Rev. B4, 648 (1971).
- [54] L. G. Van Uitert, J. Chem. Phys. 44, 3514 (1966).
- [55] L. G. Van Uitert, Luminescence in Inorganic Solid, edited by P. Goldberg (Academic, New York, 1966), P.465.
- [56] V. I. Zhekov, T. M. Murina, A. M. Prokhorov, M. I. Studenikin, S. Geogescu, V. Lupei, and I. Ursu, Sov. J. Quantum Electron. 16, 274 (1986).
- [57] A. Lupei, V. Lupei, S. Georgescu, I. Ursu, V. I. Zhekov, T. M. Murina and A. M. Prokhorov, Phys. Rev. B41, 10923 (1990).
- [58] S. Georgescu, V. Lupei, A. Lupei, V. I. Zhekov, T. M. Murina and M. I. Studenikin, Opt. Commun. 81, 186 (1991).
- [59] Kh. S. Bagdasarov, V. P. Danilov, V. I. Zhekov, T. M. Murina, N. N. Platnov, and A. M. Prokhcrov, Sov. J. Quantum Electron. 22, 341 (1992).
- [60] Francis K. Fong and Dennis J. Diestler, J. Chem. Phys. 56, 6 (1972).
- [61] John D. Dow, Phys. Rev. 174, 962, (1968).
- [62] D. J. Simkin, J. A. Konigstein, P. Myslinski, S. A. Boothroyd, and J. Chrostowski, J. Appl. Phys. 73, 8046 (1993).
- [63] R. J. Thrash and L. F. Johnson, J. Opt. Soc. Am. B11, 881-885, (1994).
- [64] V. François, F. Pelle, P. Goldner, D. Simkin, J. Lumin. 65, 57 (1995).
- [65] W. C. Shi, M. Bass and M. Birnbaum, J. Opt. Soc Am. E7, 1456 (1990).

- [66] Stephen A. Payne, L. L. Chase, Larry K. Smith, Wayne L. Kway, and William F. Krupke, IEEE J. Quantum Electron. 28, 2619 (1992).
- [67] J. A. Wang and D. J. Simkin, Phys. Rev. **B52**, 3309 (1995).
- [68] Th. Förster: Naturwissenschaften 33, 166 (1946)
- [69] Th. Förster: Disc. Faraday Sco. 27, 7 (1959).
- [70] D. L. Dexter, Th. Förster, R. S. Knox: Phys. Status Solidi 34, K 159 (1969).
- [71] K. Suzuki, J. Phys. Sco. Jpn. 16, 67 (1961).
- [72] J. Rubio o, and H. Murrieta S, R. C. Powell and W. A. Sibley, Phys. Rev. **B31**, 59 (1985).